Universiteit Gent
Faculteit Ingenieurswetenschappen
Vakgroep Electronica en Informatiesystemen

Computersimulaties in de preventie van beroertes:
ontwerpmethodes en strategieën voor virtuele procedurele planning

Computer simulations in stroke prevention:
design tools and strategies towards virtual procedure planning

---

Francesco Iannaccone

Proefschrift tot het bekomen van de graad van
Doctor in de Ingenieurswetenschappen:
Biomedische Ingenieurstechnieken
Academiejaar 2013-2014

Universiteit Gent
Faculteit Ingenieurswetenschappen
Vakgroep Electronica en Informatiesystemen

Promotoren: Prof. Dr. Ir. Patrick Segers
Prof. Dr. Ir. Benedict Verhegghe

Universiteit Gent
Faculteit Ingenieurswetenschappen

Vakgroep Electronica en Informatiesystemen
De Pintelaan 185 Blok B-5, B-9000 Gent, België

Phone: + 32 (0)9 332 46 21

Proefschrift tot het bekomen van de graad van
Doctor in de Ingenieurswetenschappen:
Biomedische Ingenieurstechnieken
Academiejaar 2013-2014

Contents

List of Figures

List of Tables

Abbreviations and Symbols

Abbreviations

μCT	Micro Computed Tomography
2D	Two dimensional
3D	Three dimensional
3T-MRA	3 Tesla Magnetic Resonance Angiography
CAS	Carotid Artery Stenting
CCA	Common carotid artery
CE	Contrast-enhanced
CEA	Carotid Endarterectomy
CFD	Computational Fluid Dynamics
CPU	Central Processing Unit
CT	Computed Tomography
CTA	Computed Tomography Angiography
DICOM	Digital Imaging and Communications in Medicine
DISP	User displacement subroutine, Abaqus
DSA	Digital Subtraction Angiography
DW	Diffusion Weighted
ECA	External carotid artery
FCA	Free cell area
FE	Finite element
FEA	Finite element analysis
FEM	Finite element modeling
FPCT	flat-panel angio-Computed Tomography
FSI	Fluid structure interaction
ICA	Internal carotid artery
IFU	Instructions For Use
ISA	Incomplete stent apposition
LFS	Largest fitting sphere
MRA	Magnetic Resonance Angiography
MRI	Magnetic Resonance Imaging

nitinol	NIckel TItanium Naval Ordonance Laboratory
NURBS	Non-uniform rational B-spline
OSI	Oscillatory shear index
SC	Strut coverage
SFE	Structural Finite Element
SP	Systolic pressure
STL	Triangulated surface (SurfaceTessellationLanguage)
TAWSS	Time averaged wall shear stress
US	Ultrasound
VDISP	User displacement subroutine, Abaqus
vmtk	Vascular Modeling ToolKit
WSS	Wall shear stress
wt%	weight percentage

Symbols

α	Angle
ϵ	Strain
γ,τ,Ψ^{ini}	Material parameters, damage model
λ	Stretch ratio
μ, α	Material parameters, Ogden model
ν	Poission's ratio
$\overline{\lambda}$	Deviatoric principal stretches, Ogden model
Ψ	Strain energy function
Ψ_{dil}	Dilatational component of the strain energy function
Ψ_{fib}	Strain energy function of the collagen fibers, Holzapfel model
Ψ_{mat}	Strain energy function of the cellular matrix, Holzapfel model
ρ	Fiber dispersion parameter, Holzapfel model
σ	Stress
τ	Tortuosity
ε	Relative error
C_{10}, k_1, k_2	Material parameters, Holzapfel model
D	Bulk modulus dependent parameter
d	Damage scale function
I	Invariant
J	Elastic volume ratio

99PCS	99 percentile of the maximum principal Cauchy stresses
%	Percentage
A	Area
D	Diameter
D	Distance of the boundary points of a centerline, tortuosity
E	Young's Modulus, Elastic modulus
F	Force
Fr	French (catheter size)
L	Length of a centerline, tortuosity
P	Pressure
R	Radius
VD50%	Volume of damaged material beyond 50%

Operators

$\sum$	Sum

Units

μm	micrometers
$^\circ$	Degrees (angle)
$^\circ$C	Temperature (Celsius)
GHz	Gigahertz (frequency)
Gpa	Giga Pascal (1e^9 Pa, E-modulus)
kPa	kilo Pascal (1e^3 Pa, pressure)
mm	millimeters
mmHg	milimeters of mercury (pressure)
MPa	Mega Pascal (1e^6 Pa, stress, E-modulus)
N	Newton (force)
Pa	Pascal (force per area)

Samenvatting
Summary

Samenvatting

Dit doctoraatsonderzoek onderzoekt de mechanische aspecten van de endovasculaire behandeling van halsslagadervernauwingen en cerebrale aneurysma's. De onderzoeken die hiervoor werden uitgevoerd worden als volgt samengevat:

- Ontwikkelingen in eindige-elementenmodelleertechnieken worden besproken: de totstandbrenging van zowel stent- als slagadermodellen en strategieën voor het virtueel plaatsen van de stents.
- Stentplaatsing in de halsslagader.
  - Er wordt een parametrische studie uitgevoerd op anatomisch realistische halsslagadermodellen. Het effect van zowel de anatomie van de patologische vaatwand als van de plaque morfologie op de stent plaatsing wordt onderzocht.
  - In vivo pre- en peri-operatieve data van twee patiënten waarvan de carotide werd gestent werd gebruikt voor het opbouwen van een virtuele stenting procedure. Het resultaat van de numerieke analyse werd gevalideerd. Klinisch relevante geometrische parameters werden geanalyseerd om de uitkomst van de procedure te evalueren.
- Stentplaatsing in cerebrale aneurysma's.
  - Drie patiënt specifieke aneurysmatische cerebrale slagaders werden virtueel behandeld met drie verschillende stents. De ontplooide stent configuraties werden vergeleken, waarbij gefocussed werd op de verschillende werking van implantaten met gesloten of open stentcellen.
  - Tot slot wordt de stenting methodologie aangepast voor het virtueel behandelen van patiënt specifieke aneurysma's. Postoperatieve CT scans worden gebruikt om de eindige-elementenresultaten te valideren.

- De voornaamste resultaten van dit onderzoek worden samengevat. Er worden enkele conclusies getrokken, waaruit richtlijnen en aanbevelingen rond verder onderzoek naar dit onderwerp worden gegeven.

Hoofdstuk 1: Anatomische en klinische achtergrond

Dit hoofdstuk bevat een korte beschrijving van de cerebrovasculaire anatomie en histologische en biomechanische infomatie over de slagaderwand. Vervolgens worden de belangrijkste beroerte-gerelateerde pathologieën geïdentificeerd op vlak van carotide atherosclerosis. De mogelijke behandelingen voor intercraniale aneurysma's worden eveneens kort beschreven. De bestaande chirurgische en endovasculaire behandelingsmogelijkheden worden uiteengezet, in het kader van onderzoek naar de huidige richtlijnen voor selectie van een behandeling.

Hoofdstuk 2: Computer simulaties in de preventie van beroertes: state of the art

Een cerebrovasculair accident (CVA) of beroerte is een heterogene medische aandoening, veroorzaakt door een langdurige onderbreking van de bloedtoevoer naar een deel van de hersenen. Preventie en behandeling van deze ziekte is van primair belang, aangezien geschat wordt dat het wereldwijd de tweede meest voorkomende oorzaak van sterfte is. Vanwege het groot aantal mogelijke oorzaken is er geen algemene strategie voor het preventief behandelen en evidence-based aanbevelingen worden gemaakt. De locatie van de hoofdoorzaken van beroertes kunnen beperkt worden tot enkele vasculaire regio's.

Steeds meer bewijs ondersteunt de hypothese dat deze katastrofische cerebrovasculaire aandoeningen kunnen gerelateerd worden met biomechanische en hemodynamische parameters. Computer simulaties van de structuur- en vloeistofmechanica lijken een optimaal instrument voor het quantificeren van deze voorspellende parameters. Verder laat de recente vooruitgang in medische beeldvorming het toe realistische *in vivo* condities (zoals accurate anatomische geometrieën en de initiële mechanische toestand) te bekomen voor patiënt specifieke analyses.

In dit hoofdstuk wordt de vooruitgang en de *state of the art* van numerieke simulaties bekeken voor 1) het analyseren van de eerste fases en de progressie van de ziekte, 2) het analyseren van het resultaat van de

behandeling, 3) het potentieel van simulaties als instrument voor risico-evaluatie en 4) het gebruik bij de planning van de procedure. Bijzondere aandacht wordt gegeven aan de intra- en extra-craniale vasculaire ziektes in de vasculaire regio's die van belang zijn bij het onderzoek naar CVA.

Bij de behandeling van een vernauwing van de halsslagader (carotide) en cerebrale aneurysma's wordt soms gekozen voor een endovasculaire behandeling door implantatie van een stent. Dit gebeurt voor patiënten met een hoog risico voor chirurgie, vanwege het lagere trauma bij deze minimaal invasieve techniek. Ook in gevallen waar de conventionele operatie niet mogelijk is door de locatie van de pathologische anatomie (bijvoorbeeld als het aneurysma niet bereikbaar is via een craniotomie, of in het geval van een aneurysma met brede hals) wordt de endovasculaire techniek gebruikt. Deze procedures hebben een hoge kans op slagen, maar bij het mislukken van de operatie is de oorzaak nog vaak onduidelijk.

Virtuele stenting procedures in patiënt specifieke of anatomisch realistische vasculaire structuren worden gebruikt om meer informatie te verschaffen over het mechanisch gedrag van deze medische implantaten en hun interactie met de vaatwand. Numerieke simulatieresultaten kunnen ook een inzicht geven tot de oorzaken van belangrijke bijwerkingen en de invloed van relevante geometrische parameters.

Hoofdstuk 3: Vooruitgang in de eindige-elementenmodellering van stenting procedures

De complexiteit van een endovasculaire stenting procedure kan nauwelijks worden gerepliceerd in een computationele setting. Veel aspecten moeten worden overwogen en vereenvoudigingen moeten verstandig gekozen worden om een evenwicht te vinden tussen de efficiëntie van de simulaties en betrouwbaarheid van de resultaten. In dit hoofdstuk worden de ontwikkelde modelleer strategieën gepresenteerd en wordt een beschrijving gegeven van de vooruitgang van de numerieke technieken voor virtuele endovasculaire behandeling.

Stents worden gewoonlijk gemaakt door het lasersnijden van een buisvormige metalen cilinder. Het ontwerp is gebaseerd op nauwkeurig beschreven geometrische patronen, waarbij extra mechanische processen specifieke kenmerken (zoals het radiaal uitzetten van de uiteinden) van het oorspronkelijke ontwerp wijzigen.

Het is in dit geval moeilijk om een exacte geometrische beschrijving van het oorspronkelijke ontwerp te vinden. Een bibliotheek van vooraf

gedefinieerde vormen op basis van Bezier splines, verder gediscretiseerd met polylijnen, werd gemaakt in pyFormex. Het opmaken van eindige-elementenmodellen van de stents met niet-repetitieve patronen wordt zo vereenvoudigd. Het voordeel van deze benadering wordt aangetoond met geometrieën geëxtraheerd uit μCT-scans, analytische of visuele bronnen. Dit zowel voor geparametriseerde als exacte replica's van de werkelijke stents.

Vasculaire modellering vereist ook bijzondere aandacht bij het benaderen van complexe vasculaire structuren. Het lumen en de externe vaatwand kunnen ook, als gevolg van de slagadervernauwing, zeer verschillende vormen vertonen. Er worden methoden gepresenteerd om patiëntspecifieke en anatomisch realistische modellen te bouwen. Deze tonen de strategieën die gebruikt werden om de verschillende weefsels in te bouwen en de methode om controle uit te oefenen op de dichtheid van het computationeel raster, om zo de efficiëntie van de simulatie te verbeteren.

Het modelleren van een realistische stentontplooiing is ook uitdagend bij het simuleren van driedimensionale, kronkelige, vasculaire geometrieën omdat de gebruikte procedurele technieken de stenting uitkomst kunnen beïnvloeden. Verschillende aanpakken om deze ontplooiing te imiteren worden gebruikt, waarbij de vereenvoudigingen en limitaties beschreven worden.

Hoofdstuk 4: De invloed van de vasculaire anatomie op het stenten van de carotide slagader: een parametrische studie voor de evaluatie van schade in het weefsel

De in het vorige hoofdstuk ontwikkelde technieken worden in dit hoofdstuk toegepast om het stent gedrag te bestuderen in verschillende pathologische aandoeningen van de halsslagader. Klinisch en experimenteel bewijs toont aan dat zowel plaque morfologie en biomechanische veranderingen als gevolg van de implantatie de oorzaken kunnen zijn van een mislukte behandeling. Om verder inzicht te krijgen in de endovasculaire ingreep, werd de virtuele omgeving gebruikt om de stenting procedure na te bootsen op atherosclerotische carotide geometrieën, waarbij een schademodel de schade van de vaatwand kwantificeert.

Vijf mogelijke vaatvernauwingen werden gesimuleerd door het veranderen van zowel de materiaaleigenschappen van het weefsel en van de vasculaire geometrische kenmerken. Hierdoor werden zowel kwetsbare en stabiele plaques onderzocht. De spanningen in de vaatwand en de

toename van het lumen van de slagader na stenting werden onderzocht, aangezien deze volgens eerdere studies mogelijks gerelateerd zijn met het falen van de endovasculaire procedure.

Onze bevindingen tonen aan dat de vorm van het lumen, de dikte van de fibrotische laag van de atherosclerotische plaque en de aanwezigheid van een onderliggende lipidekern een impact hebben op de uitkomst van de procedure. De stress analyse op de vernauwde plaats toont aan dat de plaque samenstelling de spanningsverdeling in de plaque verandert en zo ook een potientiële invloed heeft op het ontwikkelen van trombotische complicaties. Uit de kwantificering van het beschadigde volume blijkt dat de plaque samenstelling ook een impact heeft op de schade van de vasculaire gezonde regio's. Tenslotte wordt de betrouwbaarheid van de verkregen resultaten in een klinisch perspectief geplaatst.

Hoofdstuk 5: Ondersteuning van plaques na stenting van de carotiden in de klinische praktijk: een in vivo validatie

In hoofdstuk 4 werd de eindige-elementenmethode toegepast in puur virtuele parametrische modellen. In dit hoofdstuk gaan we een stap verder om te komen tot een validatie van *in vivo* patient-specifieke data.

Selectie van de gepaste patienten en een correct design van de stent zijn levensbelangrijke voorwaarden om een lage incidentie van beroertes - en daaraan gekoppeld overlijden - te bekomen bij deze complexe en riskante procedures. In de studie beschreven in hoofdstuk 4 wordt een patient-specifieke, pre-operatieve virtuele omgeving geintroduceerd en geevalueerd, die toelaat parameters te kwantificeren die de ondersteunende functie van de stent kunnen beschrijven. Dit alles is puur gebaseerd op beschikbare beeldvormingstechnieken die rechtstreeks uit de klinische routine afkomstig zijn.

Twee patienten die elk een CAS ondergingen werden virtueel gesimuleerd met twee verschillende groottes van dezelfde stent. Pre-operatieve data werden gebruikt om de numerieke modellen voor de virtuele procedure op punt te zetten. Vervolgens werden de numerieke resultaten gevalideerd met post-operatieve angiografie. Onvolledige stent appositie, vrije cel-oppervlakte en de grootste ingeschreven bol binnen de stent cel (in situ) werden geevalueerd als potentiele risicofactoren voor CAS complicaties. Deze parameters worden normaliter gebruikt om verschillende stents te vergelijken in hun vrije configuratie, maar het is duidelijk dat de in situ vervorming van de stent deze parameters sterk kan beïnvloeden.

Een kwantitatieve validatie van de numerieke resultaten met post-operatieve beelden, die werden bekomen door opmeten van de lumen diameter, toonden de betrouwbaarheid van de vooropgestelde methodologie aan. De kwantificatie van de ondersteundende functie van de virtueel ontplooide stentgeometrie benadrukte de variabiliteit van het gedrag van de stents en hun afhankelijkheid van de te behandelen laesie.

De voorgestelde methode kan derhalve gebruikt worden in de klinische praktijk als een bijkomend middel voor endovasculaire specialisten, vooral in complexe anatomische gevallen waar stent design en positionering een grote impact hebben op de uitkomst en het succes van de klinische procedure.

Hoofdstuk 6: De invloed van stent design en bloedvatgeometrie op het mechanisch gedrag van stentontplooiing in intra-craniale aneurysmas

In de voorgaande hoofdstukken werden stenotische carotiden bestudeerd. In dit hoofdstuk verschuift het vasculaire interessegebied naar aneurysmavorming in de cerebrale arteriën. Een eindige-elementenanalyse werd uitgevoerd om de invloed van stent design en bloedvatgeometrie te onderzoeken in de klinische procedure waarbij intra-craniale aneurysmas opgevuld worden met behandeld van stents.

Drie nitinol stents werden ontworpen: (i) een open cel stent die sterke gelijkenissen vertoont met de Neuroform stent, (ii) een gesloten cel stent met generieke stijve cellen en (iii) een gesloten cel stent met meer flexibile cellen. De stents werden ontplooid in drie patient-specifieke cerebrale aneurysmatische bloedvaten. De ontplooide configuratie werd opgemeten aan de hand van drie klinisch relevante parameters: het percentage van de strut oppervlakte dat de nek van het aneurysma bedekt werd opgemeten, het rechttrekken van de hersenvasculatuur door de plaatsing van de stent werd gekwantificeerd aan de hand van de reductie in tortuositeit, en de stent appositie ten opzichte van de bloedvatwand werd bepaald als het percentage van struts binnen een bepaalde afstand tot het bloedvat.

De voor- en nadelen van open en gesloten cel stents worden vervolgens bediscussieerd aan de hand van de bekomen resultaten.

Hoofdstuk 7: *In vivo* voorbeeldstudie van virtuele ontplooiing bij het opvullen van aneurysma's met behulp van stents

In hoofdstuk 6 werd het potentieel van eindige-elementenanalyses aangetoond om het behandelen van intra-craniale aneurysma's met behulp van stents virtueel te voorspellen. Deze procedure werd echter niet gevalideerd, een lacune waaraan in dit hoofdstuk tegemoet gekomen wordt.

In deze studie werd een patient bestudeerd die behandeld werd met een Enterprise stent. μCT scans van de stent, optische microscopie metingen en mechanische testen leverden een accuraat model op van de stent. De materiaaleigenschappen van het bloedvat werden gefit aan literatuurwaarden voor cerebrale bloedvaten. De eindige-elementenmodellen van bloedvat en stent modellen werden vereenvoudigd door shell en beam elementen te gebruiken, wat toeliet de numerieke prestaties merkelijk te verbeteren. De plaatsing van de stent werd accuraat nagebootst, inclusief het voorttrekken door de catheter, en kwalitatief gevalideerd aan de hand van literatuurwaarden. Dit laatste is belangrijk gezien het geweten is dat de plaatsingsprocedure een grote impact heeft op de stent appositie. Vervolgens werd de numerieke procedure toegepast op de patientspecifieke bloedvatgeometrie en werden de resultaten vergeleken met de post-operatieve CT scans.

De gebruike virtuele methodologie toonde aan dat het mogelijk is om de configuratie van het gestente bloedvat zowel kwalitatief als kwantitatief te voorspellen aan de hand van de tortuositeit van het bloedvat.

Hoofdstuk 8: Conclusies en toekomstperspectieven

Dit finale hoofdstuk geeft een overzicht van het uitgevoerde onderzoek en de behaalde onderzoeksdoelen binnen dit doctoraat door de belangrijkste resultaten en conclusies samen te vatten. Suggesties worden aangehaald om de technische hulpmiddelen die binnen dit project ontwikkeld werden verder te verfijnen naar de toekomst toe. Verder worden ook richtlijnen meegegeven voor verder onderzoek naar intra- en extra-craniale stenting.

Summary

This doctoral research had as its goal to study the bio-mechanical aspects in the minimally invasive (stent-based) treatment of carotid stenosis and cerebral aneurysms. The investigations performed to achieve this goal are:

- Advances in finite element modeling in the domain of this thesis are described, including the creation of both high quality and advanced stent and vessel models and virtual stent placement strategies.
- Carotid artery stenting
  - A parametric study on anatomically realistic carotid models is performed to analyze the effect of plaque morphology and pathological vessel anatomy on the stenting procedure.
  - In vivo pre- and peri-operative data of two patients undergoing carotid artery stenting were used to emulate the actual procedure. After validation of the numerical results, clinically relevant geometrical parameters are analyzed to evaluate the procedural outcome.
- Cerebral aneurysm stenting
  - Three patient specific aneurysmatic cerebral vessels were virtually treated with three stent designs. The deployed configurations were compared highlighting different effects of closed and open cell devices.
  - Finally, the stenting methodology is adapted for virtual patient specific aneurysm treatment. Post operative CT scans are used to validate the finite element results.
- The main results of this research are summarized, conclusions are drawn and guidelines and advice on future research on the topic are provided.

Chapter 1: Anatomical and clinical background

In this chapter a short description of the cerebrovascular anatomy is provided together with some histological and biomechanical information of the arterial wall. Main stroke-related pathologies are then identified in carotid atherosclerosis and intra-cranial aneurysms whose pathogenesis is shortly described. The current surgical and endovascular treatment options are outlined, investigating current guidelines for treatment selection.

Chapter 2: Computer simulations in stroke prevention: state of the art

Stroke is a so-called cerebrovascular disease of a heterogeneous origin caused by a sustained interruption of the blood supply to part of the brain. Prevention and treatment of this disease is of primary importance as it has been estimated to be the second leading cause of death worldwide and a huge source of morbidity. Due to the large number of possible causes there is no general strategy for preventive treatment and evidence based recommendations are given. However, major causes of stroke can be confined to few vascular districts.

More and more evidence is supporting the hypothesis that biomechanical and hemodynamic parameters play a role in these catastrophic cerebrovascular events. In this context, structural and fluidodynamic computer simulations offer an ideal tool to quantify these parameters and potential predictors. At the same time, the advances in medical imaging allow to provide realistic *in vivo* information for patient specific computational analysis.

This chapter reviews the progress and the state of the art of numerical simulations in the domain of cerebrovascular biomechanics and how these are used to analyze the early stages and the progression of the disease. In addition, the potential of these computer models as a tool for risk assessment for treatment outcome and procedure planning is reviewed. A particular focus is given to intra- and extra-cranial (carotid arteries) vascular diseases which are the districts of interest of this investigation. Endovascular treatment of carotid artery stenosis and cerebral aneurysm by stent implantation is the preferred option of treatment for patients at high risk for surgery due to its minimal invasiveness or in cases where surgery cannot be performed due to the diseased location or the pathological anatomy (e.g. when the aneurysm cannot be reached

by craniotomy or in the case of wide-necked aneurysms). Though the procedure has shown a high rate of success, causes of failure are still unclear.

Virtual stenting procedures in patient specific or anatomically realistic vessel models can provide more information on the mechanical behavior of the devices and their interaction with the vascular wall. Numerical simulations can also give insights into the causes leading to major adverse events and how these events relate with clinically relevant geometrical parameters of the deployed device and its interaction with the arterial wall.

Chapter 3: Advances in modeling strategies

The complexity of the endovascular stenting procedure can be hardly entirely replicated in a computational setting. Many aspects need to be considered and simplifications need to be wisely chosen in order to balance computationally efficient simulations and reliability of the results. In this chapter the developed modeling strategies are presented and a description of the advances of the numerical toolkit for virtual endovascular treatment is provided.

Stents are normally created by laser cutting a tubular metallic cylinder. Even though the design is based on precisely described geometrical patterns, often additional mechanical processes meant to improve specific features of the device (such as tapering or flaring of the ends) modify the original mesh. It is then difficult to retrieve an exact geometrical description of the original design. A library of predefined shapes based on bezier splines and further discretized with polylines has been created in pyFormex to simplify the creation of the finite element stent models when dealing with these non-repetitive patterns. The advantage of this approach is shown with geometries retrieved from μCT scanning, analytical or image based sources both for parametrized and complete replicas of actual device samples.

Vascular modeling also requires particular attention for a good approximation of complex vascular structures. Moreover, due to the stenotic condition, the lumen and external vessel wall exhibit very different shapes making the task harder. The methodologies to build patient specific and anatomically realistic fully hexahedral vessel meshes are presented, showing the strategies adopted to include different tissues and control mesh densities to improve simulation efficiency.

Furthermore, modeling realistic stent delivery is also challenging when dealing with tridimensional tortuous vascular geometries because the procedural techniques can influence the stenting outcome. Different approaches used to mimic the deployment procedure are here described pointing out simplifications and limitations.

Chapter 4: The influence of vascular anatomy on carotid artery stenting: a parametric study for damage assessment

The tools described in the previous chapter, are applied in this chapter to study stent behavior in parametric models replicating different pathological conditions of the carotid artery. Clinical and experimental evidence demonstrates that both plaque morphology and biomechanical changes due to the device implantation can be possible causes of an unsuccessful treatment.

In order to gain further insights into the endovascular intervention, the virtual simulation environment was used to emulate the stenting procedure on generalized atherosclerotic carotid geometries which also included a damage model to quantify and mimic the injury of the vessel. Five possible lesion scenarios were simulated by changing both material properties and vascular geometrical features to cover both presumed vulnerable and stable plaques. The results were analyzed with respect to lumen gain and wall stresses which are potentially related to the failure of the procedure according to previous studies.

Our findings show that lumen shape, fibrous cap thickness and the presence of an underlying lipid pool have an impact on the success of the procedural outcome. The stress analysis at the stenotic location shows that plaque composition changes stress distribution in the plaque, potentially influencing plaque rupture and thus leakage of plaque debris into the circulation. The quantification of the damaged volumes shows that plaque composition also has an impact on the injury of the healthy vascular tissue. Finally the reliability of the achieved results was put into clinical perspective.

Chapter 5: Plaque scaffolding after carotid artery stenting in clinical routine: an in vivo validation

In chapter 4, the finite element deployment procedure was applied in virtual parametric models. In this chapter, the study advances for validation of *in vivo* patient specific data.

Appropriate patient selection and stent design are paramount to achieve a low stroke and death rate in these complex high-risk procedures. This study introduces and evaluates a novel virtual patient-specific pre-operative environment to emulate the endovascular procedure and to quantify scaffolding parameters based on routinely performed imaging techniques.

Two patients who underwent CAS with two different sizes of the same stent device were studied. Pre-operative data were used to build the numerical models for the virtual procedure. Then numerical results were validated with post-operative angiography. Incomplete stent apposition, free cell area and largest fitting sphere in the stent cell were evaluated in situ as potential risk factors for CAS complications. These parameters are normally used for comparison of different devices in the free expanded configuration, but clearly the deformed stent shape influences these measurements.

A quantitative validation of the numerical outcome with post-operative images performed by measuring the lumen diameter demonstrated the reliability of the proposed methodology. The quantitative measurements of the scaffolding parameters on the virtually deployed stent geometry highlights the variability of device behavior in relation with the target lesion.

The proposed method may be an additional tool for endovascular specialists especially in complex anatomical cases where stent design and positioning may have a higher impact on procedural success and outcomes.

Chapter 6: The influence of stent design and vessel geometry on the mechanics of intra-cranial aneurysm stent deployment

In the previous chapters stenotic carotids were studied. In this chapter the vascular district of interest is moved to the aneurysmatic cerebral arteries. The finite element analysis is here used to investigate the influence of stent design and vessel geometry for stent assisted coiling of intra-cranial aneurysms.

Three nitinol stent design models were created: (i) an open cell stent resembling the Neuroform, (ii) a generic stiff and (iii) a generic more flexible closed cell design. The stents were deployed in three different patient-specific cerebral aneurysmatic vessels. Assessment of the deployed configuration was performed by calculating 3 clinically relevant

parameters: the percentage of strut area covering the aneurysm neck, the straightening induced on the cerebrovasculature by the stent placement (quantified by the reduction in tortuosity), and stent apposition to the wall (quantified as the percentage of struts within a threshold distance to the vessel) were investigated.

Advantages and drawbacks of closed and open cell stent devices are discussed according to achieved results.

Chapter 7: In vivo case study of stent supported coiling

In chapter 6 the potential of finite element analysis as a predictive tool to assess stent supported coiling was shown. However, the simulation procedure was lacking a validation which will be provided in this chapter by a case study.

One patient treated with an Enterprise stent is used in this study. μCT scanning of the device, optical microscopy measurements and mechanical testing provided an accurate model of the stent, while the vessel material properties were averaged based on literature values for the cerebral arteries. The finite element vessel and stent models were simplified by using shell and beam elements to improve numerical performance. Stent placement was accurately mimicked by emulating the pulling of the catheter and qualitatively validated using literature references. It is known, in fact, that the delivery procedure has a high impact on the stent apposition.

In addition, the numerical procedure was applied to the patient specific vessel geometry and results were compared to the post-operative CT scans.

The numerical methodology showed its capability of predicting the stented vessel configuration both qualitatively and quantitatively by comparing vessel tortuosity.

Chapter 8: Final remarks

This final chapter gives an overview of the research performed and the goals achieved in this doctoral thesis, summarizing results and conclusions. Suggestions and perspectives to improve the tools developed in this project and guidelines for further research on intra and extra-cranial stenting are presented.

One

Introduction to the numerical analysis in stroke prevention

CHAPTER 1

Anatomical and clinical background

To explain stroke disease and its management, an overview of the vascular district of interest and the available clinical strategies are fundamental. This chapter summarizes the necessary anatomical, histological and clinical concepts to understand procedures to treat cerebral and carotid arteries stroke-related diseases.

1.1 Overview of the main human vasculature related to stroke

The two common carotids (CCAs) are the principal arteries supplying blood to the head and neck (Figure 1.1). The right CCA originates at the bifurcation of the innominate artery while the left CCA raises from the aortic arch. The cervical portions of the CCAs are similar. They both ascend in the neck where they divide into two branches: the external carotid artery (ECA), supplying the exterior of the head, the face, and the neck and the internal carotid artery (ICA), supplying the anterior part of the brain and the orbital cavities. The cerebral portion of the ICA leaves the following branches: the anterior and the middle cerebral artery which forms the anterior cerebral circulation and the posterior communicating artery which connects the anterior and the posterior cerebral circulation. The posterior cerebral circulation consists of

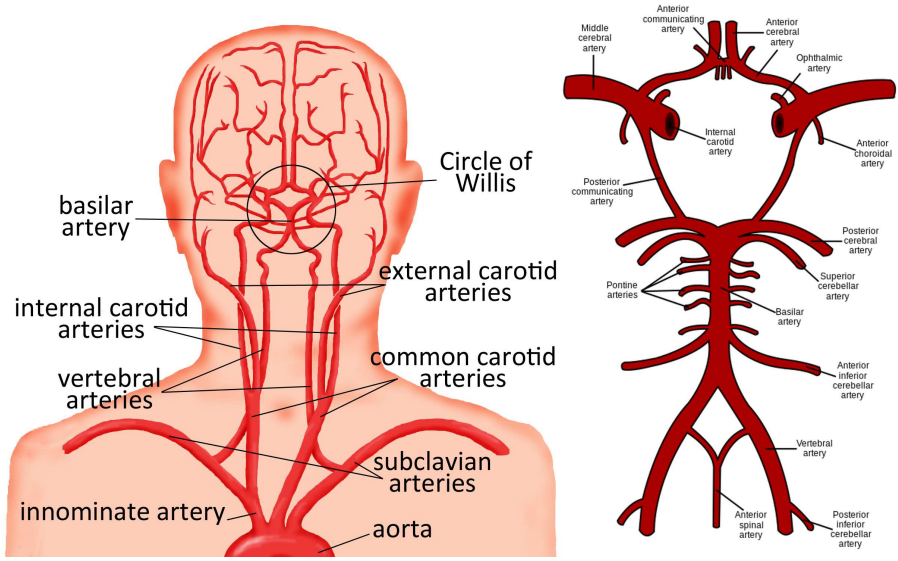

Figure 1.1: Overview of the arterial circulation of the brain (including carotid arteries) (left) and the circle of Willis (right).

the branches generated from the vertebral arteries (originated from the subclavian arteries) which merge in the skull into the basilar artery. The latter branches into posterior cerebral artery, anterior inferior cerebellar artery, pontine branches and superior cerebellar artery. Both cerebral circulations form the Circle of Willis (Figure 1.1), which provides backup circulation to the brain due to the interconnection among them [1].

1.2 Histology and typical mechanical behavior of arterial walls

Adequate constitutive descriptions of arterial walls require knowledge of the arterial histology to understand the mechanical characteristics and the components providing the main contributions to the deformation process. In this section this relationship is explained. The reader is invited to refer to the work of Holzapfel et al. [2] here resumed. Arterial types are roughly distinguished between elastic (central arteries such as aorta or carotid arteries) and muscular (peripheral arteries such as the cerebral arteries). They are composed of three distinct layers:

i the intima: the inner layer composed of one layer of endothelial cells resting on a thin basal membrane. Healthy intima is very thin and

does not have a real influence on the mechanical behavior of the vessel. Though pathological changes (such as in atherosclerotic arteries) can lead to thickening and stiffening of the intima and can give significant contribution to the arterial behavior.

ii the media: is the middle layer consisting of smooth muscle cells, elastin and collagen fibrils. They are composed of concentrically fiber-reinforced medial layers separated by an elastic laminae, whose thickness decreases at the periphery. These interconnected structures are oriented in a continuous fibrous helix almost in the circumferential direction. This architecture provides strength, resilience and resistance in both the longitudinal and circumferential directions making the media the most relevant layer from the mechanical perspective.

iii the adventitia: is the external layer constituted by fibroblasts and fibrocytes (cells synthesizing collagen and elastin) and a fibrous tissue of thick bundles of collagen fibrils arranged in helical structures. Its thickness is strongly dependent on the function and location of the vessel (e.g. in cerebral arteries it is almost absent). The adventitia gives a reinforcement to the vessel wall, exhibiting a stiffer behavior with the pressure increase to prevent over-stretching and rupture.

From a modeling point of view, arteries can be described as a fiber-reinforced material with the contribution of two different components: a non-collagenous matrix which can be assimilated to an isotropic material and the contribution of two families of symmetric collagen fibers helically oriented along the longitudinal axis (possibly with different orientation in each layer when the artery is not considered as a unique layer) which account for the anisotropic response of the artery.

1.3 Pathological conditions

The studies performed in this thesis are focused mainly on two pathological conditions which may lead to stroke: carotid arteries atherosclerosis and intra-cranial cerebral aneurysms. Atherosclerosis is a complex arterial lesion whose causes are still unclear. Age, gender, family history, race or ethnicity, genetic factors, hyperlipidemia, hypertension, smoking, diabetes, obesity, diet high in saturated fat, lack of exercise are all risk factors for the development of the disease.

Atherosclerosis leads to thickening and hardening of the arteries due to the formation of a plaque. A plaque is the accumulation of fatty substances, cholesterol, cellular waste products, calcium and fibrin (a clotting material) in the inner lining of an artery.

Without detailing the molecular and biochemical processes involved in the different stages of the disease, which lie outside the purpose of this work and for which the reader is invited to refer to more complete publications (see e.g. [3]), here the classification proposed by Stary et al. [4–6] is given. This classification relates the progression of the lesion with histological data. Eight types of lesions are defined:

- type I: adaptative thickening of the intima layer which represents an adaptation to local mechanical forces;
- type II: appearence of macrophage foam cells and lipid-laden smooth muscle cells and formation of lesions designated as fatty streaks;
- type III (pre-atheroma): formation of small pool of extracellular lipid;
- type IV (atheroma): extension of the lipid volume to form a lipid core;
- type V (fibro-atheroma): fibrous thickening of the intima to form a fibrous cap (stable plaque).

Plaques of type IV and V may evolve in other types:

- type VI: complicated lesion leading to unstable plaque due to intra-plaque hemorrhage, thinning/rupture of the fibrous cap and thrombus formation;
- type VII: calcified plaque;
- type VIII: fibrotic plaque without lipid core.

Further studies (specific on MRI of carotid arteries) [7] improved this template classification including the possible presence of calcifications in type IV, V and VIII. A schematic of the evolution of the pathology is depicted in Figure 1.2.

While stable plaques impair only the blood supply to the brain, unstable plaque may embolize due to the leakage of plaque material or migration of a superficial thrombus. If either of these occurs and blocks

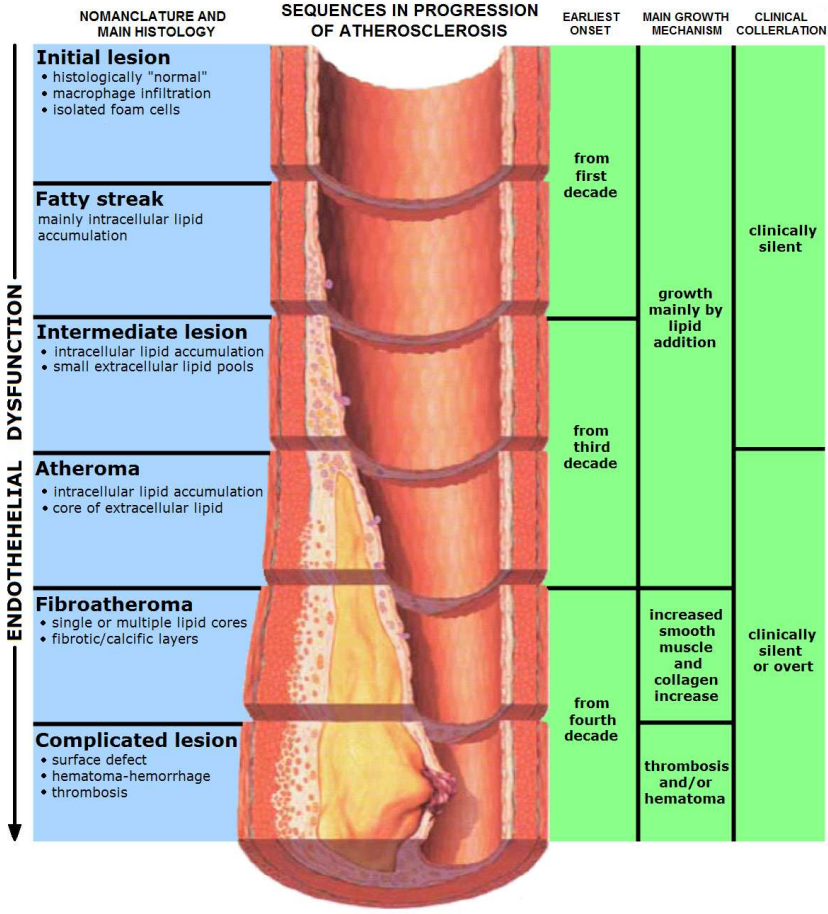

FIGURE 1.2: Schematic stages of endothelial dysfunction in atherosclerosis. Reproduced from http://en.wikipedia.org/.

the whole artery, a stroke may result. It is obvious that the heterogeneity of the plaque composition determines its complex mechanical behavior which is challenging to describe without accurate histological information.

Causes of stroke related to cerebral arteries are instead more attributable to aneurysms. An aneurysm is the bulging of the artery, due to the weakening of the vessel wall layers. Its propensity to rupture may lead to subarachnoid hemorrhage and thus stroke. The association between anatomic variations and pathological conditions (such as

hypoplasia or occlusion of a segment of the circle of Willis, high-flow arteriovenous malformations, at points of flow bifurcation) which can lead to local increase of flow-related forces, have suggested a fluid dynamic contribution to the disease. Aneurysm formation is associated with enzymatic degradation of the main structural components of the vessel wall, elastin and collagen, and smooth-cell apoptosis which lead to loss of elasticity and mechanical properties. For a more detailed discussion on the topic the review of Sforza et al. is suggested [8]. Age, family history of aneurysms, alcohol and drugs consumption, smoking, hypertension or infections are acquired risk factors.

1.4 Current treatment options

1.4.1 Carotid artery disease

The treatment options for the carotid artery disease are i) medical therapy, ii) endarterectomy (CEA) and iii) endovascular treatment (angioplasty/stenting). The treatment is mainly chosen according to the stenosis degree calculated from angiography[9] (Figure 1.3), plaque vulnerability, symptomatological history, age and co-morbidities. Guidelines for carotid artery disease treatment have been provided [10] by stratifying the patients in four categories according to the ratio benefit/risk. The medical treatment consist of anti-platelet therapy to reduce progression of the disease. This option is normally preventive for patients with or without history of previous ischemic event, and it is followed when revascularization is not recommended (stenosis $<50\%$).

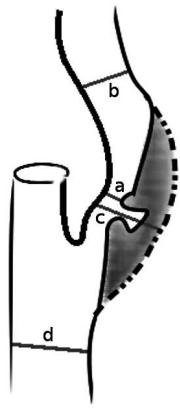

$$\text{ECTS method} : \%\,stenosis = \frac{c-a}{c} \times 100$$

$$\text{NASCET method} : \%\,stenosis = \frac{b-a}{b} \times 100$$

$$\text{CC method} : \%\,stenosis = \frac{d-a}{d} \times 100$$

Figure 1.3: Methods for measuring the degree of stenosis.

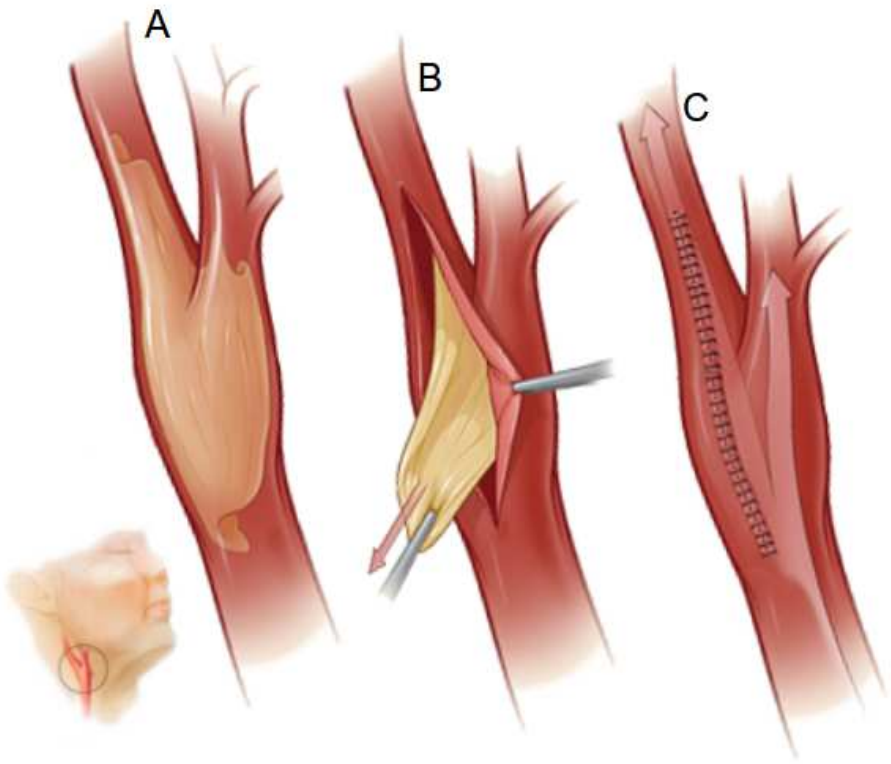

FIGURE 1.4: Schematic CEA procedure: *A*: Intact carotid; *B*: Arteriotomy and plaque removal; *C*: Suturing of the arteriotomy. Adapted from https://www.nhlbi.nih.gov/.

CEA is a treatment to surgically remove the plaque. After incision of the neck, the carotid is exposed. Clamping of distal and proximal healthy portion is performed to interrupt blood flow in the vessel. When the patient has inadequate collateral circulation shunting is chosen over clamping. The vessel is incised, the plaque dissected and removed. Sutures (or patch angioplasty for large incisions) are used to close the vessel and then the circulation is restored. CEA (depicted in Figure 1.4) is the leading treatment nowadays when medical treatment is not sufficient. For a more extensive explanation of the procedure the reader should refer to [11]. CEA is indicated for patients with low surgical risk with previous non-disabling ischemic stroke, symptomatic patients with stenosis $>50\%$ (documented by catheter angiography) and assessed risk of stroke/mortality $<6\%$, and it is suggested for asymptomatic patients with stenosis $>70\%$ of the ICA.

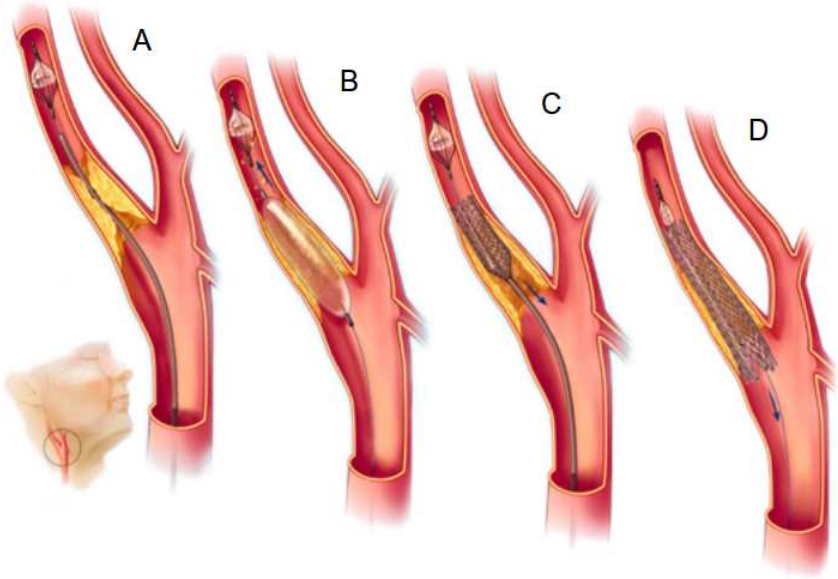

Figure 1.5: Schematic CAS procedure: *A*: Insertion of the of guidewire, sheet for stent delivery and the embolic protection for possible plaque leakage; *B*: Balboon angioplasty to enlarge the lumen by spreading and breaking the plaque; *C*: Insertion of the stent *D*: Stent placement, catheter and filter removal. Adapted from [12].

Carotid artery stenting (CAS) is a minimally invasive endovascular option to restore the vessel lumen through insertion of a self-expandable metallic tubular mesh, i.e. the stent. The CAS procedure is schematically explained in Figure 1.5. The procedure involves the insertion of a guidewire (normally by femoral access) through short sheath to reach the ICA of the diseased artery. The guidewire will serve as a rail to easily reach the stenosis by the catheters carrying the necessary devices.

An embolic protection device may be inserted and opened distally to the lesion to collect eventual debris. Balloon angioplasty may be performed to pre-dilate the stenotic lumen and thus allowing for easy access of the stent delivery system. After balloon removal, the stent is addressed to the lesion location and deployed. Finally eventual post-dilation balloon inflation is performed to improve unsatisfactory procedural outcomes. The outstanding work of Macdonald and Stansby [13] provides a detailed overview of all facets of CAS. This procedure is suggested for patients when CEA is not performable due to high risk for surgery or in case of unfavorable anatomies for surgery. It is considered an alternative to CEA for symptomatic patients with stenosis >50%

with risk of stroke/mortality <6%. CAS might also be considered in asymptomatic patients with stenosis >60%.

1.4.2 Cerebral aneurysm treatments

Three primary treatment options are available for cerebral aneurysms: observation with antihypertensive therapies, surgical clipping, (stent-assisted) endovascular coiling (Figure 1.6).

The clinical condition of the patient, the aneurysm location and morphology (diameter of the neck and its relation to the parent artery) and the presence of branches arising from the sac or the neck are important considerations when choosing the most appropriate treatment plan.

Clipping is a very invasive technique which involves craniotomy, exposure of the aneurysm and placement of a metal clip across the neck of the aneurysm to prevent blood flow into the aneurysm sac.

Endovascular coiling is a minimally invasive technique. A catheter is inserted through femoral access and advanced until the cerebral vessel sliding over the guidewire previously inserted. Once the catheter is in place, platinum coils are advanced through the catheter into the aneurysm, to conform to the shape of the aneurysm. The coils promote embolization thus preventing rupture.

Stent-supported coiling is an extension of the previous technique for wide-necked and giant aneurysms where a stent is used as a scaffold to prevent coils herniation into the parent vessel. The insertion of the coils can occur before or after stent placement. In the first case the balloon remodeling technique for coiling can be used to assist the placement of each coil in unfavorable geometries. In the latter case, catheterization of the dome can occur through the stent cells, or by placing a micro-catheter prior to stent deployment within the aneurysmal cavity, in order to secure access for subsequent coiling (jailing technique).

New stent devices known as flow diverters exhibit a very fine mesh which harbors flow circulation into the bulge, and thus induce embolization without the use of coils. However, long latency times between device placement and obliteration of the sac are considered a drawback of this procedure.

An overview of the available endovascular techniques and their associated complications is provided in [15].

While the International Subarachnoid Aneurysm Trial [16] has shown lower recurrences with coiling than micro-surgical clipping for ruptured aneurysms, the management of unruptured cerebral aneurysms remains one of the most controversial topics in neurosurgery. Komotar et al. [17]

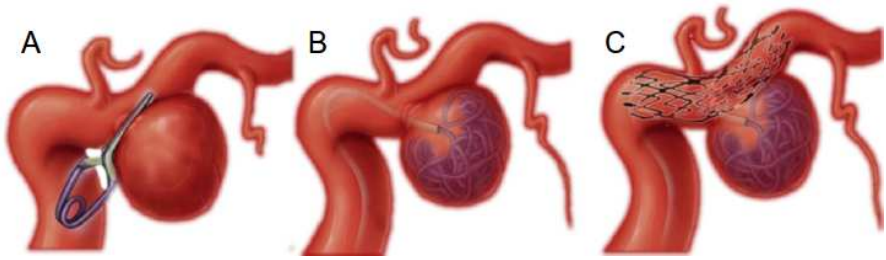

Figure 1.6: Intra-cranial cerebral aneurysm treatment options: *A*: Micro-surgical clipping; *B*: Endovascular occlusion with coils; *C*: Endovascular occlusion with stent-supported coils. Adapted with permission from [14].

provided guidelines by summarizing the large literature on the topic. Main conclusions of the research were outlined as follows:

- symptomatic unruptured aneurysms should be treated;
- small incidental aneurysms <5 mm should be managed conservatively;
- aneurysms >5 mm in patients less than 60 years of age should be treated;
- large incidental aneurysms >10 mm should be treated in patients less than 70 years of age;
- clipping should be the first choice in low-risk and long life expectancy cases due to the frequency of re-bleeding of coiling.

Other authors [18] cite different size thresholds strongly recommending treatment for unruptured aneurysms >12 mm except in older patients and in presence of significant comorbidities, for symptomatic patients and with enlarging aneurysm. It is suggested for aneurysms of 7-12 mm for young patients, for specific high risk locations (posterior circulation and posterior communicating artery), in presence of daughter sac and a family history of subarachnoid hemorrhage. It is also suggested for young patients with aneurysms <7 mm for the same high risk locations, in presence of daughter sac and a family history of subarachnoid hemorrhage. An overview of the recent indications for the treatment of unruptured aneurysms can be found in [19].

Coiling is a valid alternative to clipping and platinum coil technology has tried to address incomplete aneurysm occlusion, which increases the

risk of coil compaction and aneurysm re-canalization. The major argument against the use of stent devices is linked to the need for concurrent anti-platelet therapy which increases the risk of re-bleeding.

Other general guidelines for the management of aneurysmal subarachnoid hemorrhage from the American Heart Association/American Stroke Association [20] were also provided: treatment of hypertension, choice of endovascular coiling over clipping when the ruptured aneurysm is amenable by both procedures, preferred clipping for large hematomas and middle cerebral artery aneurysms, coiling should be preferred in the elderly (>70 years of age) and in those with aneurysms of the basilar apex, stenting of a ruptured aneurysm is associated with increased morbidity and mortality.

CHAPTER 2

Computer simulations in stroke prevention: state of the art

This chapter provides an extensive overview of the state of the art in the domain of cerebrovascular biomechanics, with numerical simulations being performed to (i) understand the evolution of the causes leading to stroke; and (ii) as predictive tool for risk assessment. This chapter has been adapted from its published version :
"Computer Simulations in Stroke Prevention: Design Tools and Virtual Strategies Towards Procedure Planning", Iannaccone, F., De Beule, M., Verhegghe, B., and Segers, P. *Cardiovascular Engineering and Technology, (2013)* [21].

2.1 Introduction

Stroke is a heterogeneous disease caused by a sustained interruption of the blood supply to part of the brain due to blockage (ischemic stroke) of an artery to the brain or due to hemorrhage after the rupture of a vessel (in most of the cases aneurysmatic) mainly located in the cerebral circulation. Prevention and treatment of this disease is of primary importance as it has been estimated to be the second leading cause of death worldwide [22]. Of all strokes, 85 to 87 % are of an ischemic nature while the remaining are intra-cerebral and subarachnoid hemorrhage strokes

[23–25]. The source of the occluding embolus in ischemic stroke may be cerebrovascular atherosclerosis, lacunar (related to small penetrating brain arteries) or cardiogenic (e.g. the consequence of atrial fibrillation), but the definite cause cannot be identified for a large amount of ischemic strokes (cryptogenic) [25,26] as depicted in Figures 2.1 and 2.2.

Due to the large number of possible embolic origins there is no general strategy for preventive treatment and evidence-based clinical recommendations are given [27,28]. Thrombolytic therapy is normally preferred for cardiogenic embolism, anti-platelet agents for non-cardioembolic stroke [27,28]. Recently the use of a new class of temporary thrombectomy devices (the so called stent retrievers, which have a similar design to stents used in stent supported coiling) showed to be effective in the treatment of acute ischemic strokes [29, 30]. Revascularization is possible in case of cerebral aneurysm (ruptured and/or unruptured) by clipping, coiling, stent supported coiling or using flow diverters.

The exact treatment strategy will depend on the location, shape and dimension of the aneurysm. The use of an surgical approach or revascularization using endovascular devices for atherosclerotic disease is still controversial (at least in certain cases, mainly due to the lack of knowledge on the long term effects of the endovascular devices) and is normally performed in patients who have sustained symptoms despite medical therapies [27,28]. For patients with hemodynamically significant

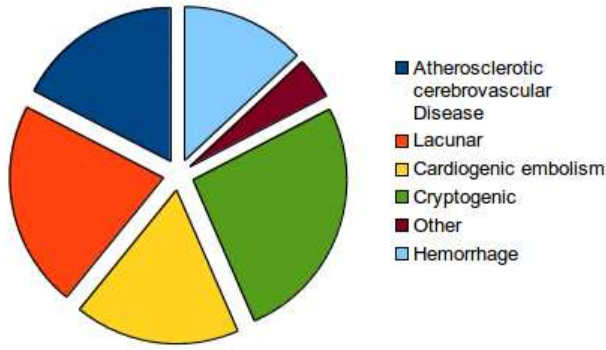

Figure 2.1: Distribution of the mechanisms leading to stroke.

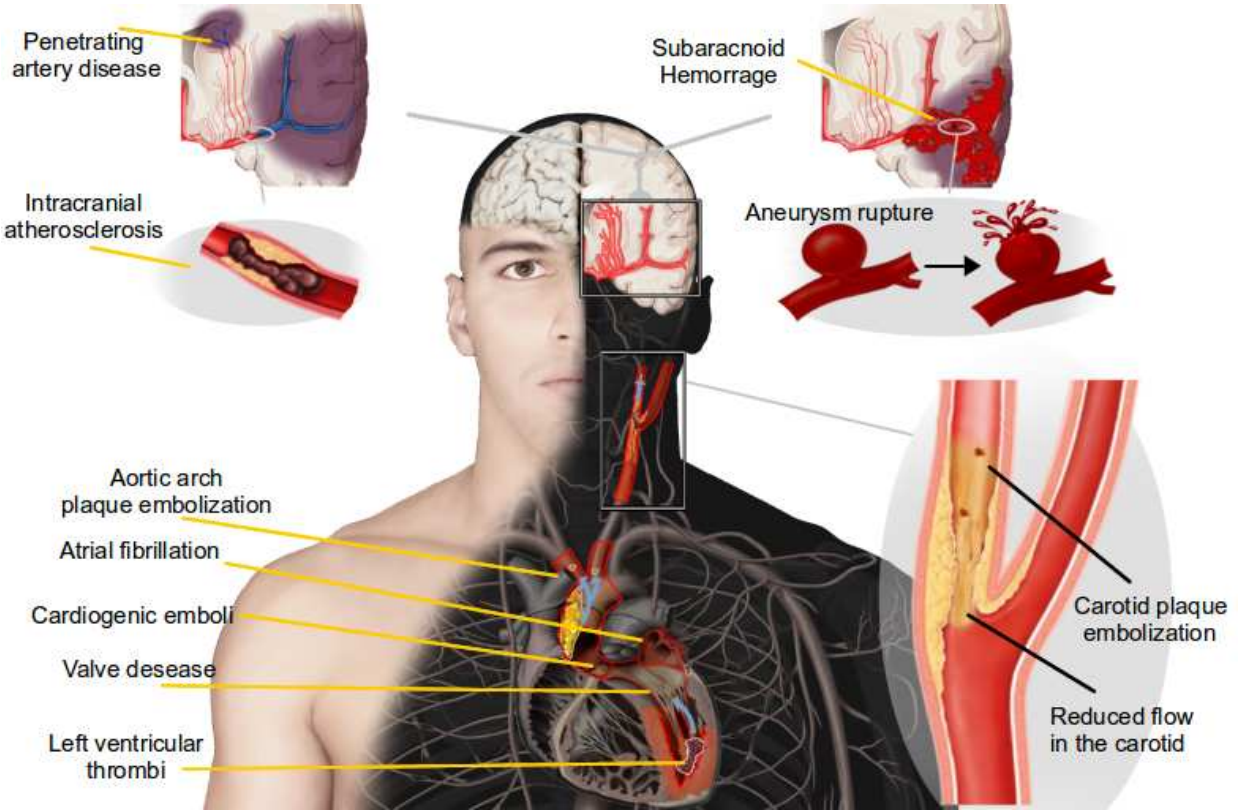

FIGURE 2.2: Most frequent sources of ischemic and hemorrhagic stroke.
Adapted from http://www.daviddarling.info/, http://www.strokecenter.org/, http://www.ikonet.com/.

intracranial stenosis, endovascular treatment (angioplasty and/or stenting) is an effective solution to improve cerebral blood flow [27, 31, 32]. Symptomatic extra-cranial vertebral stenosis without ulceration can be successfully treated with stenting reducing the risk of elastic recoil and restenosis compared to balloon angioplasty alone [33]. For atherosclerotic carotid diseases, while low degree of stenosis does not seem to have a preferential therapy, carotid endarterectomy (CEA) is still the recommended procedure for the majority of cases, except for symptomatic severe stenosis and in patients with high risk for surgery that are suited for carotid artery stenting (CAS) [34–38].

2.2 Role of computer simulations in stroke prevention

Several stroke-related cerebrovascular diseases have been associated with specific hemodynamic and biomechanical "milieus". Examples are the specific flow patterns in the carotid bifurcation region (characterized by low and oscillatory wall shear stress) which have been associated with an atherosclerosis-prone environment, mechanical stress profiles in vulnerable plaque types, or the influence of low shear stresses in the growth of cerebral aneurysms. Numerical biomechanical analysis has been introduced to analyze and quantify these biomechanical actors, and has become an extra tool to study and understand the development of some vascular diseases. More and more, the potential of this numerical analysis is recognized as possible diagnostic or risk assessment tool, and to evaluate clinical procedures. Computer simulations used in the field of cerebrovascular disease focus on the study of:

1. Structural finite element (SFE) simulations, applying structural mechanics to study critical stress/stretch conditions,

2. Computational fluid dynamics (CFD), for the study of the fluid domain in order to analyze potential hemodynamic factors,

3. Fluid structure interactions (FSI) simulations, a combination of both SFE and CFD that takes into account the relative effects of both the structural and fluid domain, in general leading to a more realistic solution.

The main issues in order to reproduce realistic numerical simulations are related to the acquisition of the realistic conditions of the environments to be reproduced: accurate geometries of both the anatomical

district and device, fluidodynamic and/or mechanical boundary conditions and material parameters (blood rheology, tissue organization and stiffness) that are specific for the subject at study. The anatomical sites that have been most intensively studied through numerical modeling are the carotid and cerebral arteries. These vascular territories will be the focus of this chapter. The organization of the rest of this chapter is as follows: first, imaging techniques are reviewed, as these provide the essential information (geometrical data and boundary conditions) underlying the patient-specific models, followed by segmentation methods to extract the model geometry. Next, computer model generation strategies are reviewed, including techniques to obtain material properties. Finally, applications are addressed, with

(i) initiation and progression of (carotid) atherosclerotic diseases,

(ii) atherosclerotic plaque rupture,

(iii) endovascular carotid treatments,

(iv) initiation, progression and rupture of intracranial aneurysm,

(v) aneurysm coiling,

(vi) aneurysm stenting,

(vii) intracranial atherosclerosis.

2.3 Imaging techniques for numerical modeling

Evaluation of vascular disease and related causes of stroke is mainly performed using medical imaging techniques thanks to the improvements of high-resolution *in vivo* imaging. Conventional angiography and in particular digital subtraction angiography (DSA), both 2D (Figure 2.3a) and 3D, is still the gold-standard to detect cerebral aneurysms and to evaluate the degree of stenosis of carotid arteries because of the high resolution (up to 150 μm) and accuracy. It is, however, associated with high costs and high risk of morbidity and mortality due its invasive nature due to the contrast injection and is therefore performed almost exclusively in the peri-operative procedure [39].

On the other hand, ultrasonography (US) is the primary noninvasive test to evaluate extra-cranial cerebral vessels due to its simplicity, low cost and ability to distinguish different structures (Figure 2.3b).

The presence of dense calcification of the plaques, however, affects its accuracy and due to operator dependence, vascular tortuosity and the proximity of the transducer to the tissue of interest, it is not always feasible to obtain good image quality. Thus US requires to be complemented with other diagnostic techniques when suspicious conditions are detected. In most cases, a diagnostic evaluation for cerebral vascular disease can be performed by using either magnetic resonance angiography (MRA) or computer tomography angiography (CTA). Contrast-enhanced (CE) MRA or CTA (Figure 2.3c, c') offer full anatomic depiction of the cervical and cerebral portions of the common and internal carotid artery [40]. The strength of current MRA techniques, however, is the ability to identify key determinants of plaques using multi-contrast imaging (typically time-of-flight angiography, T1, T2, and proton density weighted sequences) [41]. As the prevalence of stroke (for untreated atherosclerotic patients, after CAS or CEA) has demonstrated to be higher in patients with carotid plaques containing fragile components [42–45], it is important to evaluate the characteristics of a carotid artery plaque accurately before endovascular treatment. US, MRA and recent multi-detector-row CTA all seem to be able to differentiate plaque composition (and thus identify vulnerable plaques) when compared with histological results and among each other [45–47]. In particular CT and MR angiography offer high-resolution images and can demonstrate the entire circumference of the carotid arterial wall with excellent visualization of calcification (CTA) and lipid-necrotic core, intra-plaque hemorrhage, ulcers and fibrous cap (MRA) [47]. Moreover MRA and CTA can both provide measurements of the arterial wall thickness [48–50] showing good agreement with the intima-media thickness measured by US [51, 52], a parameter used for cardiovascular risk assessment in general and for risk of carotid stenosis progression in particular [53, 54]. Intracranial atherosclerosis is normally detected by CTA [39], but new high resolution MR techniques also demonstrated to be efficacious for intracranial plaque detection [54]. Due to their reproducibility, three-dimensional nature and the ability to discriminate different structures, CTA and MRA are the most used techniques for image-based numerical simulations [40, 55].

In addition to its ability to define the vessel lumen and wall, phase contrast (PC) MRI is one of the most powerful techniques for time resolved blood flow quantification *in vivo* [40]. Due to this feature PC-MRI is largely used in image-based CFD for providing *in vivo* inlet and outlet flow or velocity boundary conditions of the vessel geometries.

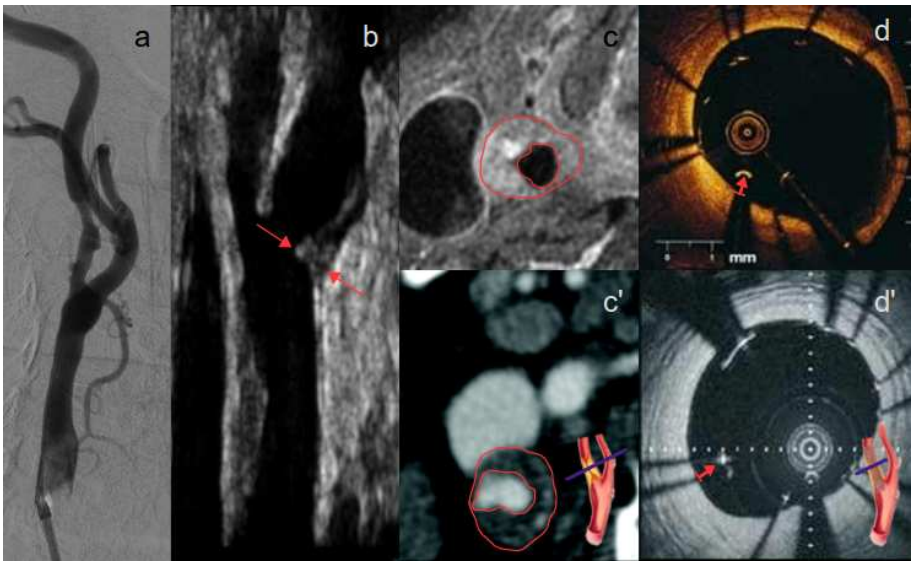

FIGURE 2.3: Common imaging techniques for cerebrovascular diseases: *a*: 2D Digital subtraction angiography; *b*: 2D Ultrasounds; *c* and *c'*: Longitudinal cross sectional of Contrast enhanced T1 Magnetic resonance angiography *c* Multi-detector-row Computer tomography angiography *c'* (lumen and external wall are tracked); *d* and *d'*: Intra-vascular Optical Coherence Tomography *d* Intra-vascular Ultrasounds *d'* (arrow indicates the gap between the stent strut and the vessel wall). Adapted with permission from [56], [57], [58], http://www.examiner.com/.

However, the presence of complex flow patterns, such as at the carotid bifurcation, or turbulence, can introduce artifacts on the velocity measurements [59]. US imaging of vascular anatomy, though widely used in the clinic, has minor relevance in image-based numerical analysis, mainly due to the lack of reference to a fixed coordinate system, making it difficult to reconstruct 3D geometries [40]. However the advantage of US to retrieve real-time blood flow measurements makes it suitable to provide realistic boundary conditions for fluidodynamic simulations [60, 61]. On the other hand 3D US systems have served for image reconstruction and CFD simulations [62, 63]. Intra-vascular US (IVUS) has a higher potential in image-based CFD modeling studies [64–66] due to its capability to acquire detailed images of the vessel structure. Due to the invasiveness of the procedure, however, IVUS has been limited to patients already referred for catheterization and is still uncommon for patient with high risk of plaque rupture even though IVUS (Figure 2.3d) can well evaluate the result of stenting procedures [67]. In addition US and IVUS coupled with SFE can be used to derive wall elasticity

by tuning the computational model with the displacements acquired by the US technique [68–70]. Intra-vascular Optical Coherence Tomography (OCT) (Figure 2.3d') has also been proven to be an effective tool to study stent strut apposition in carotid arteries, though the technique is still in an experimental phase [71, 72].

2.4 Building the model: Segmentation strategies

The segmentation, i.e. the partitioning of the image to reconstruct vascular structures (Figure 2.4a and Figure 2.4b) is of primary importance for diagnosis, treatment and surgery planning and it is a major primary step in realistic computer simulations. The processing of the large amount of data from 3D imaging modalities such as CTA and MRA is still difficult to fully automate and thus still requires significant manual operations, with significant time cost. The growing interest for (semi) automatic procedures to speed up the work flow and to obtain less inter-operator variability is therefore logical [73]. Literature offers many reviews on general vascular segmentation strategies [73, 74], grouped by medical imaging technique [75–79] or focusing on specific methods [80]. We refer to these studies for more detailed information on the topic. The different approaches can be classified as: pattern recognition techniques, model-based, tracking-based, artificial intelligence-based, neural network-based, and tube-like object detection [74]. The majority of these strategies for automated segmentation is focused on the vessel lumen extraction which is relatively easy when volumetric images have well defined lumen boundaries, such as CTA or CE-MRA images. Dealing with suboptimal images or low contrast structures like vessel walls, thrombus or plaque components leads to additional issues. Lately (semi) automatic detection tools have been proposed [81–83] based on the previously described imaging techniques in order to discriminate different structures and components of the vessel and to recognize vessel wall borders. What emerges from these studies is that, even though many steps can be seeded up with automatic algorithms, the operator intervention is still crucial in the procedure. Further optimization and validation on large datasets are thus needed.

2.5 Computational model generation

It is a challenging step to go from a segmented geometry to a meshed 3D geometrical model that is suitable for numerical analysis using CFD,

SFE or FSI (Figure 2.4c). Structured meshes (characterized by a regular connectivity that can be expressed as a two or three dimensional array) can be relatively easily built for simple vessel segments. For more complex geometries with bifurcations and/or branching vessels, unstructured meshes (tetrahedral, hexahedral) are more easily generated [84] using widely available mesh generators mainly intended for CFD simulations. A survey of unstructured mesh generators, though not up to date, can be found in [85]. Many of these software packages start from the segmented geometry to discretize the volume using 3D elements. However, the resulting meshes can be over- or under-resolved relative to the requirements of the solution [55] dramatically affecting the extraction of relevant hemodynamic parameters [86]. Only few tools for structured grids are described in literature due to the complexity of creating acceptable quality elements over the complete domain of complex geometrical structures [87–90]. Structured grids can be built to organize the elements along the main flow direction in order to assure more accurate numerical solutions especially when solving the blood flow in large vessels where the blood motion is highly directional [87]. It has been shown that structured meshes have faster convergence compared to unstructured meshes [89]. An alternative for CFD simulations is the use of tetrahedral quadratic elements with refined boundary layers composed of prismatic elements [91] or adaptive refinement methods [86, 92, 93]. 3D mesh generation becomes more difficult when bifurcations, wall thickness and multiple structures need to be included (i.e. plaques and calcifications), which is typical for structural and FSI analysis. In-house solutions have been developed to solve these issues. Even though an unstructured (tetrahedral) mesh generator can serve, it is well known that hexahedral meshes lead to a more accurate solution [94].

The basic approach to create a structured mesh of the vessel-wall is to discretize the outer and inner surface and the internal structures with an equal number of key-points and to connect these. For bifurcating vessels, additional interpolation is required at the bifurcation. This process can be done either deriving the point on the contour of the 2D segmented slices [95–98]) or either using 3D non-uniform rational basis spline (NURBS) surface reconstructions [99]. These procedures are often complex and require different software packages for every step to achieve the final mesh. The pre-processing of 3D numerical simulations are thus time consuming and not yet really suitable for routinely procedure planning.

In order to reduce the complexity, the problem may be simplified with a bi-dimensional approach. Despite the computational cost advantage of

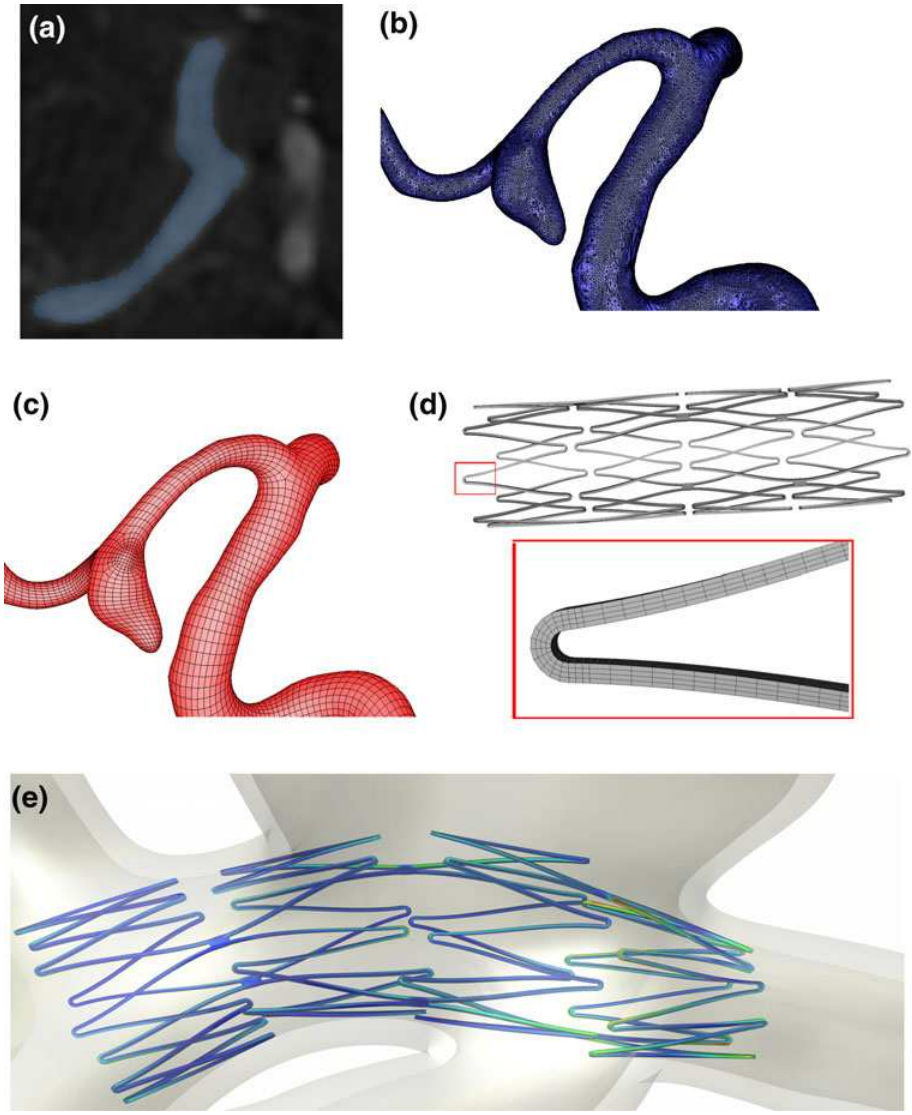

Figure 2.4: Typical work-flow for a patient specific finite element simulation: Starting from medical imaging (CT scan) *(a)*, a 3D vessel geometry is reconstructed using segmentation techniques *(b)* . Next the segmented 3D vessel model is discretized in a mesh *(c)*. Combining this vessel model with the stent mesh (d) allows to predict and evaluate the mechanical interaction between both using SFE (e).

2D models (especially when using FSI simulations), these models have great limitations especially when involving fluidodynamic simulations. For example, as highlighted by Tang et al [95], 2D models ignore non-uniform pressure and the drop in pressure at the stenotic region caused by the narrowing which has been shown to collapse arterial stenotic models. Axial stretch, which leads to radial contraction, is also often neglected and in very asymmetric models with complex plaque structure it will introduce large errors. In addition 2D SFE models do not account for shear stresses, torque, or time-varying forces acting on the lesion in the models.

A next step in complexity are simulations including the medical devices (Figure 2.4d and Figure 2.4e), which can increase enormously the difficulties associated to the mesh generation and the simulation in general. A common approach to model stent devices is the use of CAD like programs to draw the basic pattern to be meshed using additional tools [100–103]. Image-based reconstruction strategies have also been proposed for semi-automated mesh generation of stent [104], or coils device [105, 106] . CFD/FSI modeling with implanted device can be extremely challenging even with powerful codes [107,108]. An interesting approach is based on embedding methods well described in a recent review by Löhner et al [109] which seems promising for CFD simulations including stent and coils [105].

2.6 Getting the material properties

Implementation of adequate constitutive laws to describe the complex material behavior with correct (subject-specific) parameter values is extremely important for a correct SFE or FSI analysis. Most of the studies available in literature use one layered vessel models with isotropic, incompressible material behavior, which does not take into account differences in radial and axial behavior of the vessel and the plaque. Indeed the vessel wall and the plaque constituents have a highly non linear anisotropic and viscoelastic behavior, and neglecting this can lead to high differences in the derived biomechanical parameters [96, 110]. Moreover, during endovascular procedures manipulations through balloon angioplasty or stenting, arteries experience non-physiological loads showing an inelastic behavior as a result of the damage to both arterial tissue and the plaque. Damage can be expressed as a combination of stress softening and permanent deformations which might depend on plastic deformation of the fibrous components [111].

In addition, not taking into account the axial in situ pre-stretch can also lead to incorrect stress predictions [96]. This might be less critical in comparative studies, but it is important to note that exact stress magnitudes are not reliable without a complete and accurate description of the mechanical properties of the vascular structure or the virtually implanted device. There is a general lack of knowledge of human arteries and plaque material properties and only few accurate mechanical test studies have been performed [112,113]. Moreover the variability between individuals, complex characteristics of the plaque due to inhomogeneities and remodeling processes can change the arterial morphology in the long term, making realistic simulations very challenging.

2.7 Numerical simulations in atherosclerotic diseases

2.7.1 Initiation and progression of atherosclerosis

The propensity for plaque formation at bifurcations, branching, and curvatures (conditions common to the carotid and coronary arteries, infrarenal abdominal aorta and vessels of the lower extremities) has led to the hypotheses that local mechanical factors such as wall shear stress (WSS) and wall tensile stress play a role in atherogenesis [114]. First, experimental studies using *in vitro* models [115, 116] identified intimal thickening at the carotid sinus and at bifurcations (all zones where WSS is lower) and related plaque formation with low and oscillatory WSS. Next, CFD has been extensively used to demonstrate the correlation between plaque formation and both low WSS and high oscillatory shear stress *in vivo* for carotid arteries [117–119]. CFD simulations of 50 normal human carotid bifurcation samples found correlations between low and oscillatory shear stresses and between indicators of disturbed flow at the normal carotid bifurcation [120, 121] showing a significant relationship between disturbed flow and both proximal area ratio and bifurcation tortuosity, but not with bifurcation angle, planarity, or distal area ratio [120].

However, as plaque progression continues, the severity of the stenosis increases and lumen narrowing induces complex flow features with separation zones [122] which are associated with elevated local shear stress conditions [123–125] while WSS oscillations are observed downstream [122, 126]. These results suggest that other mechanical factors such as plaque wall structural stresses contribute to the disease process as the wall shear stress hypotheses alone cannot explain the plaque progression process [127]. The interaction of mechanical forces on the

upstream plaque shoulder increases the pressure on the proximal plaque region and can be measured as tensile stress. Consecutive hemodynamical changes and/or modifications of the plaque configuration increase the stress on the plaque and might lead to rupture, depending on plaque stability [128]. The relative roles of wall shear stress, tensile stress, and the metabolism of the artery wall in the progression and complication of atherosclerosis remain to be clarified.

2.7.2 Plaque Rupture

Plaque rupture is the direct underlying cause of many acute manifestations of cardiovascular disease associated with adverse events [129]. This is not only the case for vascular territories associated with stroke, but also for the coronary arteries where plaque rupture leads to myocardial infarction. As the underlying mechanical mechanisms are common, and given the more extensive literature in this field, we will in this section also refer to studies on coronary plaque mechanics. Currently, the decision for clinical intervention is based on the degree of luminal stenosis and plaque severity. Guidelines for treatment have been developed based on large clinical trials [34–36]. Nonetheless there was group of patients in the European Carotid Surgery Trial [35] that revealed higher risk of stroke in presence of ulceration [128]. Criteria for plaque vulnerability parameters were redefined [130] for a better risk stratification and include active inflammation, the presence of a thin cap with a large lipid core, endothelial denudation with superficial platelet aggregation, a fissured plaque (which is likely to induce thrombus [131, 132]) or stenosis $> 90\%$. Calcification seems to be not related to stroke symptoms [132]. Compensatory remodeling associated with atherosclerotic plaques as a response to the pathological environment as first described by Glagov et al [133] in coronaries may result in angiographically normal endoluminal dimensions that mask the presence of underlying large atheromas at risk of rupture [134, 135].

Prediction of plaque rupture is not an easy task as it depends on many interlaced factors. Rupture is not only associated with plaque morphology and composition (thin fibrous cap, soft lipid pool, thrombotic lesions), but also with biomechanical stresses that are induced hemodynamically [135]. This suggests that, provided these biomechanical stresses can be accurately determined, there is a potential usefulness of simulations for patient-specific plaque assessment. Even though the role played by hemodynamic actors in the early manifestation of atherosclerosis has been studied extensively, there are few studies describing their role on the mature plaque and the mechanisms inducing rupture [136].

The evidence that plaque rupture is likely to occur at the upstream shoulder of the plaque [136,137] has suggested that high wall shear stress is involved in the rupture. CFD studies on *in vivo* and *ex vivo* image-based stenotic carotid models have confirmed this observation [138,139]. CFD simulations have been used to correlate fluidodynamic descriptors such as WSS, time averaged (TA) WSS and oscillatory shear index (OSI) with the histology of vulnerable plaques. The findings generally confirmed the general trend of previous experimental studies (i.e. lipids and macrophages correlating negatively with WSS and TAWSS and positively with OSI) even though the results were not conclusive [140]. Note, however, that a recent *in vivo* MRI-based study of 18 atherosclerotic carotids (comparing 3D FSI simulations with histological analysis) suggested that while flow shear stress values have good correlation with the degree of stenosis, critical plaque mechanical stresses are a better predictor of plaque rupture and the sites of occurrence [141].

Structural simulations combining mechanical factors and morphological information have been introduced to study rupture in coronary and carotid plaque, in order to study patterns of tensile stresses and to define critical stress levels. SFE and FSI studies on simplified models of the lumen section have provided a better understanding of the effect of the morphology on the plaque rupture. One of the first works using SFE suggested that stress concentration on the fibrous cap is associated with high local pressure, which can be a trigger of plaque rupture [143]. Lumen curvature and fibrous cap thickness showed to be major determinants of plaque stress, while the size of the lipid core did not seem to influence the stress distribution when it is covered by a thick fibrous cap [144–146]. On the other hand thin fibrous caps in presence of moderate degree of stenosis appear to increase the risk of rupture [147]. Simulations based on *ex vivo* specimen derived from cadavers or endarterectomy have been extensively performed. Using SFE Cheng et al [148] studied 2D histological-based patient specific models of coronary arteries establishing a relation between circumferential stresses and location of plaque rupture. This study also suggested that mismatch in the exact rupture location was imputable to local defects in plaque strength which could render less stress-solicited zones prone to rupture. Huang et al [149] investigated the influence of calcification and the lipid pool on the plaque stresses comparing the real morphology with different possible scenarios of the plaque composition, suggesting that the calcification did not influence plaque stability. 2D and 3D FSI models [95] indicated that large lipid pools and thin plaque caps are associated with

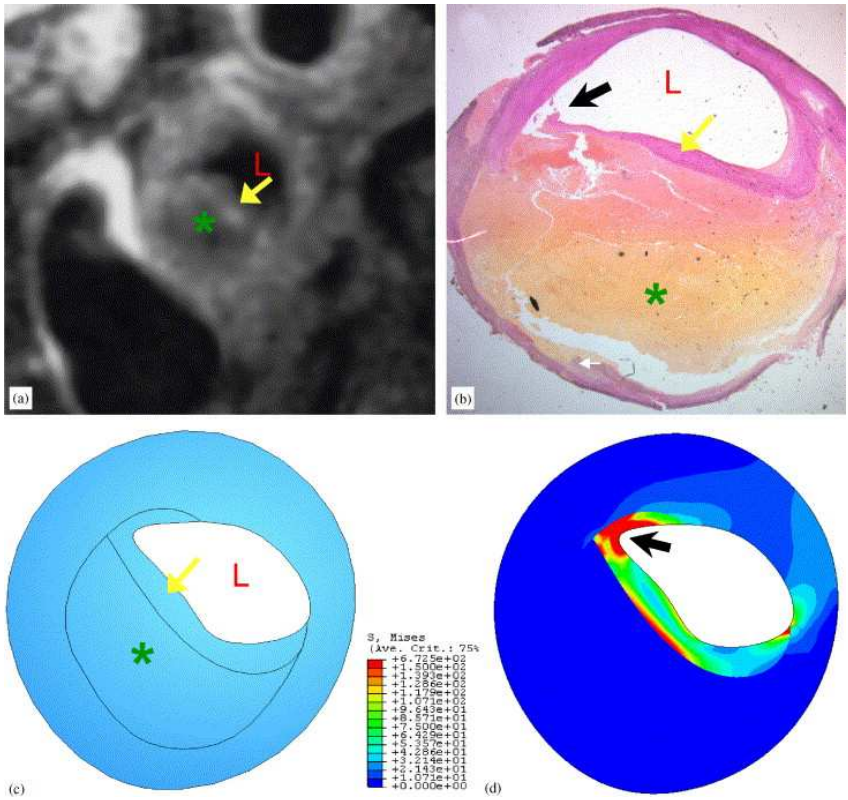

FIGURE 2.5: Correlation between maximal stress concentration and plaque rupture. *a* T1 Weighted MRI (L: lumen; fibrous cap: yellow arrow; lipid pool: green star); *b* Histological analysis shows rupture of the fibrous cap at the shoulder region (black arrow) associated with a focal hemorrhage; *c* Numerical model of the plaque; *d* Stress distribution showing high stress at the ruptured location (black thick arrow). Reproduced with permission from [142].

both extreme stress/strain levels. These results were also confirmed in 2D/3D FSI models compared with silicon experimental models in different flow conditions and it has been highlighted that stenosis severity, eccentricity, lipid pool size, shape and position, axial stretch, pressure, and fluid-structure interactions are factors leading to an increase of plaque stress. Moreover tube compression and collapse, negative pressure and high shear stress at the throat of the stenosis, flow recirculation and low shear stress upstream were observed. These critical flow and mechanical conditions may be related to platelet aggregation, thrombus formation, excessive artery fatigue and possible plaque cap rupture [123, 124, 150].

With the advent of high resolution imaging techniques, detailed morphological and structural characterization of carotid plaques could be performed *in vivo* avoiding problems that can arise from analysis on *ex vivo* specimens (possible structural alterations occurring during surgery, histological preparation, morphological configuration, altered material properties of the plaque components) and, as such, may provide a more accurate quantitative assessment of plaque stress [142]. A significant correlation has been found between plaque stress and lumen curvature, the lumen curvature being significantly larger for symptomatic patients [145, 151] and ruptured plaque exhibiting higher maximal stresses than unruptured [142, 152, 153] as shown in Figure 2.5.

These studies also showed that ulcerating regions were affected by higher WSS and it was noticed that stress concentration occurred at the shoulders and the thinnest fibrous cap regions [141,152]. These modeling studies thus provided the initial *in vivo* evidence that plaque rupture may be linked to higher plaque wall stress.

Local biomechanical stresses have been found to have a better correlation with plaque morphological features than global maximum stress [154]. Larger relative stiffness of the fibrous cap compared to lipid pool resulted in higher stresses within the cap [142]. Whether numerical analysis has an added clinical value is a topic of study. Even though stress analysis seems to be able to differentiate different groups of patients, they failed to refine risk stratification among symptomatic patients with/without hemorrhage or thrombi. Stretches, instead, were able to differentiate the two groups [153].

FSI was used to identify and verify the zone of pronounced stress in a pre-rupture stenosed carotid confirming the location and extension of the plaque rupture [155]. The same computational strategy applied in a study on 61 patients demonstrated that biomechanical structural stresses (with geometrical models based on MRI scans), are significantly associated with the development of subsequent ipsilateral cerebrovascular ischemic symptoms in patients with a predominantly lesser degree of carotid stenosis at baseline. This suggests a possible strategy for risk stratification and selection of candidates for appropriate non-invasive or surgical treatment [156]. Anyway it must be taken into account that the accuracy of the boundaries in the plaque reconstruction is crucial because it can significantly change stress values [157] and the lumen boundary extraction affects the reproducibility of fluidodynamic simulations [158].

Besides excessive stress, plaque rupture may also be a fatigue-related process as hypothesized by some authors [159, 160]. Levels of pulse pressure and mean pressure (descriptors of the fatigue process – but also of

stress level as such) indeed seem to be related to stroke events [161,162]. Large cyclic stress/strain variations observed in FSI plaque models under pulsating pressure may lead to material fatigue and possible plaque rupture [95]. SFE fatigue studies on generalized atherosclerotic cross sections related the increment of crack propagation with blood pressure and lipid stiffness [144].

2.7.3 Endovascular carotid treatment

Although CEA is still the preferred procedure to treat carotid stenosis, CAS is emerging as an alternative technique. Its benefit over CEA is, however, still controversial [37,163,164]. After CAS the peri-procedural risk of stroke is high [163] and the implanted device may induce restenosis [165]. There are indications that stent design has an influence on CAS failure [166] and that changes in the biomechanical environment due to stenting/angioplasty promote restenosis [64]. Anyway few numerical studies are available on CAS. Numerical simulations have been used to assess comparison between different stent designs when inserted in the same vessel model. A study on an idealized carotid model comparing the effect of two stent designs showed that strut length influences the final configuration of the vessel [167]. Using a patient specific stenosed carotid model, Auricchio et al [168] simulated the insertion of 6 different commercially available laser-cut stent devices to study the impact of the design on the stress configuration of the treated vessel (Figure 2.6).

They found that the closed-cell design provides a higher lumen gain, that oversizing affects the stress induced in the vessel wall and that configuration and size have a limited impact on the vessel straightening.

Important is also the scaffolding provided by the stent in order to confine the plaque. There is no standardized vessel scaffolding definition and the proposed parameters [169] compare the stents in their free-expanded state not taking into account the actual configuration of a stent implanted in a tortuous carotid bifurcation. Conti at al [170] validated their numerical simulation with a stented carotid silicon model (with the geometry based on patient data) showing good agreement with the experimental results. They evaluated two different stent designs and their ability to scaffold the vessel measuring the inter-strut angles of the stents. The closed-cell design provided superior vessel scaffolding compared to the open-cell but reduced the stent ability to accommodate to the irregular eccentric profile of the vessel cross section, leading to a gap between the stent surface and the vessel wall. Using a similar strategy

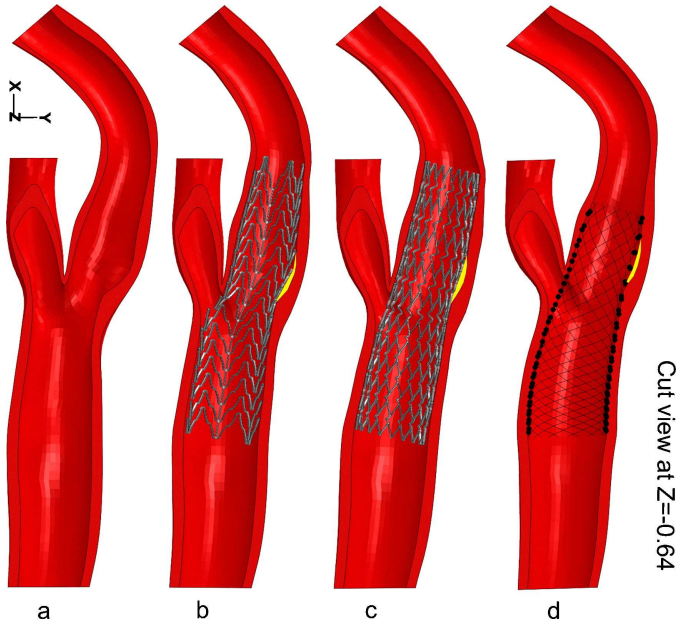

Figure 2.6: Structural simulations for different carotid stents. *a* Pre-stenting carotid artery; *b* post-stenting carotid artery with the ACCULINK (Abbott, IL, USA); *c* post-stenting carotid artery with and the XACT (Abbott, IL, USA); *d* post-stenting carotid artery with the Wallstent (Boston Scientific Co., Natick, MA, USA). The gap between the stent and the vessel is highlighted in yellow. Reproduced with permission from [168]

.

and the same model they compared four designs and analyzed the deformed cell area along the stent (as a measure of the scaffolding). This study suggested that evaluation of the expanded configuration of the stent neglects the post-implant variability, which seems to be more pronounced in open-cell designs, especially at the bifurcation segment [110]. A virtual stent implantation in a simplified model associated the effect of calcification on the stenting procedure with severe residual stenosis, dog-boning effect, and corresponding edge stress concentrations after stenting, which requires pre- and/or post-interventional management [171].

The hemodynamic effect of incomplete stent apposition to the vessel wall was demonstrated in a CFD study. A virtual stent implantation in a realistic carotid model showed that malapposed stent struts can cause disturbing flow and potentially lead to trombo-embolic events [172]. This has been confirmed in a study performed *in vivo* on stented coronary arteries, which related neo-intimal response with WSS and other hemody-

namic parameters derived from CFD [108]. Remarkable in both studies is that the implanted geometry was derived from structural analysis. Incomplete stent apposition was previously assessed using SFE for coronary stents [173,174]. Cebral et al [175] also performed CFD in a stented carotid geometry by use of virtual geometrical implantation describing flow patterns changes. Hayase et al [61] via virtual prototyping performed CFD to recommend the best design for surgical reconstruction during a carotid treatment case study.

In addition SFE has been used to study the behavior of an embolic protection device for carotid stenting in different configurations and computing the apposition of the device in a straight vessel [176].

The effect of balloon angioplasty has been rarely analyzed for carotid arteries. Lee et al [177] using 2D SFE, could predict the location of plaque rupture after angioplasty, which was simulated by simply applying pressure on the plaque. More accurate simulations of balloon angioplasty (also combined with stenting) have been reported for other districts. The effect of balloon angioplasty in a very accurate iliac artery model (both from the anatomical and material point of view) has been studied with and without stenting [96,97,178]. Coronary balloon-expandable stents have been also virtually implanted [101]. Anyway in these studies the balloon itself was either neglected or simplified. Mortier et al [179] simulated the entire procedure for coronary balloon-expandable stents with side branch access, emulating the real mechanics of the balloon inflation. They reported that the procedure may compromise the downstream branch lumen. Similarly Gastaldi et al [103] modeled the provisional side-branch stenting technique in atherosclerotic coronary bifurcations analyzing effects of stent positioning, after *in vitro* model validation. Unfortunately, *in vivo* validation of these numerical studies is rare and not performed on a statistically relevant number of cases.

2.8 Numerical simulations in intracranial aneurysm treatment

2.8.1 Formation, development and rupture of the aneurysm

The initiation, progression, and rupture of aneurysms are also related to complex interactions of flow-dependent biomechanical factors, acting with similar underlying mechanisms of the atherosclerotic disease. Hemodynamic characteristics, such as flow recirculation, secondary flows, and jet impingement may be relevant to assess. In particular WSS

has emerged as a biomechanical flow-related parameter of interest for aneurysm assessment and CFD is a valid tool for providing this information [180]. A recent review [180] analyzed in detail the added value of CFD in the aneurysm evaluation. The most important factor for accurate calculation of intra-aneurysmal flow patterns is the vessel geometry [181]. The improvements in medical imaging for detailed depiction of the brain and cerebral blood vessels have produced an increase of CFD studies on patient specific aneurysms derived from angiographic information with clinical purposes. This overview complements and extends the above mentioned interesting review paper and focuses also on relevant studies including structural simulations.

As shown by fluid dynamic modeling, complex hemodynamic forces and alteration of the WSS [182, 183], may induce pathologic remodeling of the vascular structure, transmitted by the endothelial cells [184, 185]. An *in vivo* animal model, complemented with CFD showed that localization of destructive wall remodeling, is correlated with high WSS and high WSS gradients [186]. Similar results have been found in a recent study [187] that suggested patients displaying zones of localized high WSS (>5 times the parental vessel) to be prone to aneurysm formation (Figure 2.7).

On the other hand, low wall shear stress has been observed in many aneurysm studies and could potentially be involved in the growth of the aneurysm [188, 189]. Comparing *in vivo* aneurysm with virtually reconstructed parental vessels prior to aneurysm formation, numerical simulations revealed an area of relatively low WSS at the location at which each aneurysm had developed [190]. Similarly, another study assessing the *in vivo* intracranial aneurysm at two time points in 7 patients [191], found that aneurysm growth is likely to occur in regions where the endothelial layer lining the vessel wall is exposed to abnormally low wall shear stress [187, 192, 193].

Omodaka et al [194] found that the rupture point was located in a low WSS region of the aneurysm wall in 6 patients with ruptured aneurysm. In a study on 20 cerebral aneurysms it has been found that ruptured aneurysms had higher averaged WSS in the aneurysm region than unruptured aneurysms, markedly low WSS in their tip and high WSS in the body of the aneurysm. In this work the authors speculated that the proximity of high and low WSS in a small aneurysm region promotes degeneration of the aneurysm wall [188]. A study on 62 patients (classified into different categories, depending on the complexity and stability of the flow pattern, the location and size of the flow impingement region, and

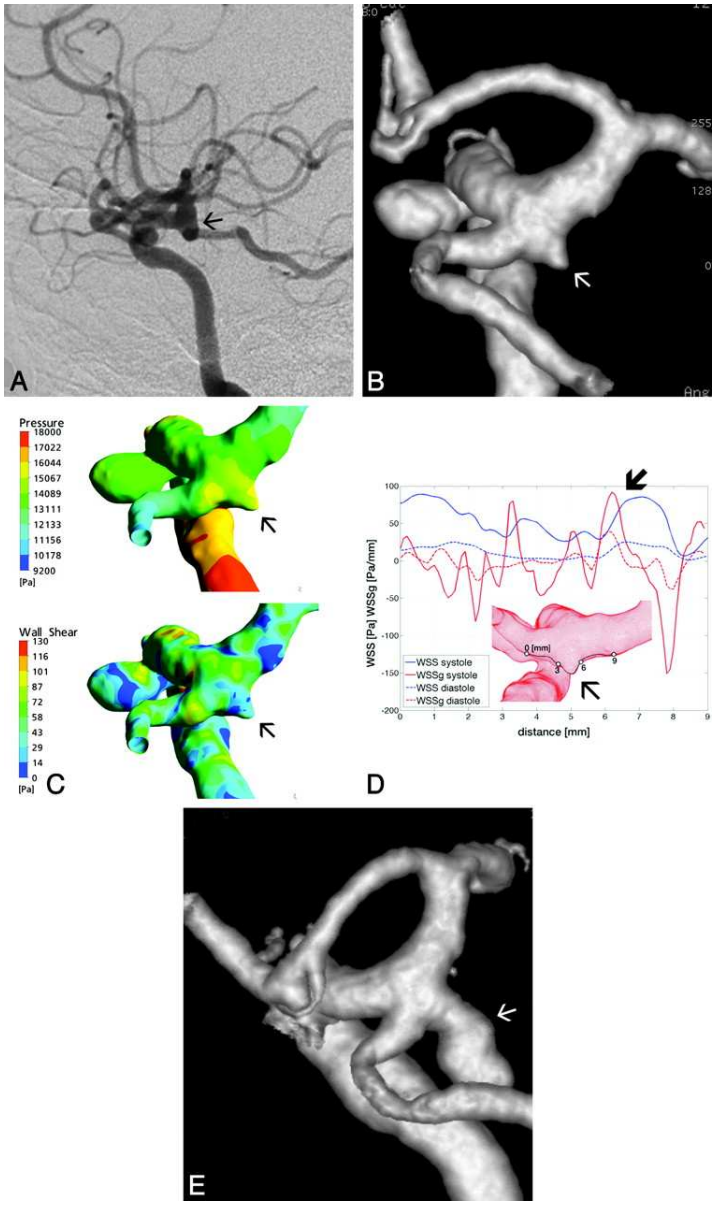

FIGURE 2.7: Evaluation of aneurysm evolution: *A* DSA of vessel in the pre-aneurysmatic condition; *B* 3D reconstruction of vessel in the pre-aneurysmatic condition; *C* pressure (upper) and WSS distribution (lower) show increased forces at the aneurysm beginning (arrows); *D* along the defined line, a first peak in SWSSG after point 3, followed by a lower WSS peak and again at points 6 and 7 respectively (thick arrow). These points correspond to the proximal and distal edges of the grown aneurysm. *E*, Evolution of the aneurysm that ruptured (arrow). Reproduced with permission from [187].

the size of the inflow jet) demonstrated an association between the size and stability of the inflow into the aneurysm and its propensity of rupture [195]. On a larger number of patients, the same authors also found that concentrated inflow jets, small impingement regions and complex and unstable flow patterns are correlated with a clinical history of prior aneurysm rupture [196]. A recent CFD study on 100 patients suggested the loss coefficient, a parameter characterizing energy expenditure and the geometric shape of vessels, as a better discriminant of aneurysm rupture than WSS [197].

The geometrical characteristic also seems to play a role in the rupture. As the arterial curvature increased, flow impingement on the distal side of the neck intensified, leading to elevations in the WSS and enlargement of the impact zone at the distal side of the aneurysm neck [198]. The morphological parameters of the aneurysm sac (discriminants of rupture such as size ratio, undulation index, ellipticity index, and non-sphericity index) have been shown in a large population study to be highly correlated with computationally derived hemodynamic descriptors (low WSS, high OSI which have been linked to rupture [199]) suggesting a possible role as clinical predictors [193].

As cerebral artery aneurysm rupture occurs when wall stress exceeds the strength of the wall tissue, FSI simulations seem more appropriate for predicting rupture [200]. Using FSI the effect of hypertension was studied, suggesting that blood pressure and deformation of the aneurysm wall can influence rupture [201] and they are closely related to the aneurysm shape [202]. Similarly a study on 7 patient-specific aneurysms found that flow patterns, pressure, WSS and displacement of the aneurysm wall exhibit large variations, depending on the morphology of the artery [203]. These results seem to suggest that WSS is not directly responsible for the aneurysm rupture but rather for a vascular remodeling process leading to rupture that is often related to low values of WSS, while other hemodynamic factors (such as pressure or flow impingement) can directly lead to rupture.

2.8.2 Aneurysm Coiling

A further challenge for numerical simulations is to account for the presence of endovascular devices to treat cerebral aneurysms, such as coils and/or stents/ flow diverters that promote clot formation and thrombosis to prevent rupture.

For clinical purposes , a priori knowledge of the mechanical and hemodynamic effects of the implantation is useful to evaluate and optimize

treatment options for example to compute the amounts of coils and their optimal placement for flow occlusion [105,204]. A CFD study on 17 patients demonstrated that, after occlusion induced by coil embolization, the increase of maximum WSS and partially averaged WSS can discriminate recanalized (a typical adverse event deriving from coils compaction) and stable aneurysms [205].

Numerical simulations including coils have been developed using different strategies. The simplest approach is to model the coils as blocked cells in the aneurysm lumen mesh [206]. In these studies the relative pressure amplitudes did not change under different simulated aneurysm filling conditions. It has been reported that coils can relieve the influx of pulsating blood and allow for initial clotting provided that at least 20% of the volume is filled.

Byun et al [207] analyzed the blood flow fields of lateral aneurysm models for different coil locations (modeled as a sphere) and parent vessel geometries suggesting that distal neck coiling better promotes embolization. Ahmed et al [208] with a similar modeling strategy used FSI to study inflow rate, WSS, apparent viscosity and effective stress of coiled aneurysm models as a possible tool to address additional treatment. An interesting approach was developed by Kakalis et al [209] modeling the coiled part of the aneurysm as a porous medium with characteristics determined by the coil sizes. CFD results showed that insertion of coils rapidly changes intra-aneurysmal blood flow and causes reduction in trans-mural pressure and blood velocity up to stagnation, providing favorable conditions for thrombus formation. Cebral et al [105] showed a more realistic technique for coil implantation based on *in vivo* data and an embedding grid technique. Morales et al [106] used a virtual coiling technique based on a dynamic path planning approach to insert one-by-one the coils inside a closed geometry consecutively selecting the next position of the coil tip (Figure 2.8). Morales et al. also found that coils configuration reduce its influence on the hemodynamics as the packing density increases.

Due to the complexity of the procedure, real-time simulation of coil insertion as a possible training tool have been proposed based on SFE [210] and a combination of a novel method to solve fluidodynamic problems and SFE that takes into account the relative interaction between flow and coils [211].

2.8.3 Aneurysm Stenting

Stent-supported coiling is used as a treatment option for fusiform and wide-neck aneurysms to avoid coil protrusion in the parent vessel. In

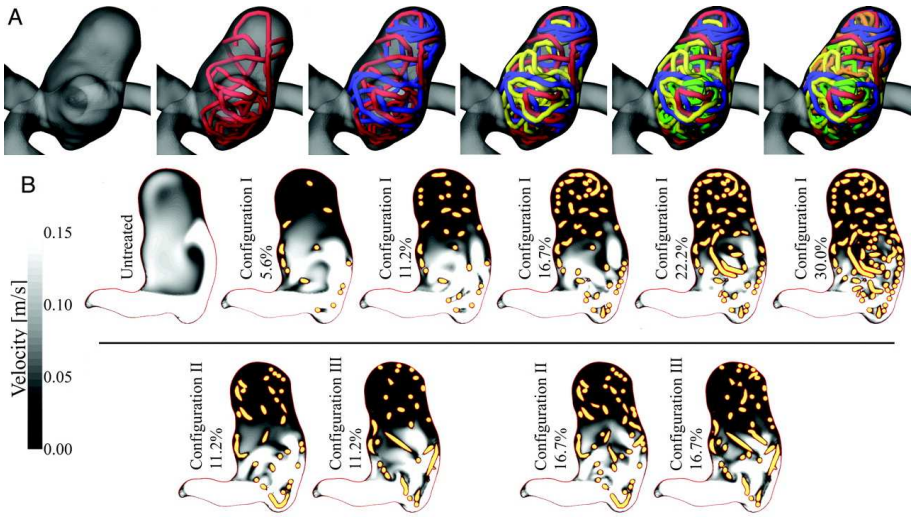

Figure 2.8: Virtual coiling for real aneurysm geometries. *A* configuration of the implanted coils. From the left untreated model and models with coil packing densities of 5.6%, 11.2%, 16.7%, 22.2%, and 30.0%. *B* Blood flow velocity magnitudes in gray-scale for an aneurysm cross-section at peak systole. Changes in the velocity are presented with a different coil configuration and increasing packing density. Reproduced with permission from [106]

.

case of flow diverters (stents with low porosity), the stent is used alone to reduce the flow in the aneurysm. Stent placement induces hemodynamic changes in the aneurysm dome which effects are not known.

CFD simulation used to analyze the effect of flow diverters in actual cases showed that rupture of giant aneurysm is influenced by an increase of pressure in the aneurysm [212]. This effect has been also described in a CFD study comparing different idealized stent designs (both braided and laser cut) in an internal carotid aneurysm model [213]. Two commercial stents were deployed at various locations and the computed residence times were evaluated and compared, demonstrating the advantage associated with a lower stent porosity with respect to the maximum wall shear stress in the aneurysm sac [214] (Figure 2.9).

A different approach used by Augsburger et al [215] is to model the stent as a porous medium, which seems to give results comparable with real stent geometries.

Even though these CFD studies are appealing from a clinical point of view they suffer of a major limitation in the stent placement technique. The stent in fact is often deployed using geometrical projection methods

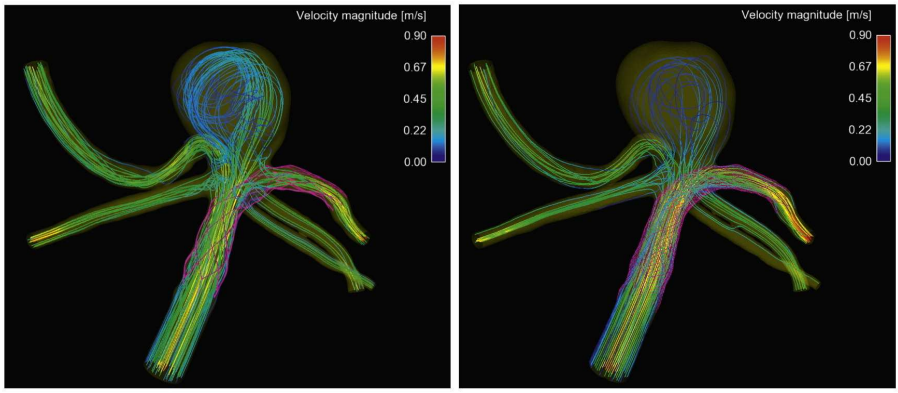

FIGURE 2.9: Flow streamlines in an aneurysmatic artery virtually treated with a stent for stent-supported coiling (left) and a flow diverter (right). Reproduced with permission from [214].

to the vessel wall [214, 216, 217] that neglect the stent mechanics and do not reckon with the actual behavior of the stent and its effects on the vessel wall. It has been shown *in vitro* that the deployment method used to deliver the vascular reconstruction device plays a critical role in stent apposition to the vessel wall [218] which has already been associated with adverse effects such as late stent thrombosis in the coronary circulation [219]. Moreover stent placement induces changes in the vessel geometry [220] that are not reflected using geometrical fitting of the stent for the numerical simulations. SFE can reproduce the real mechanics of stent deployment.

Bernardini et al [221] compared different stent simulation techniques (SFE vs geometrical) showing that the final configuration of the stent is affected by neglecting the mechanical material properties. A SFE analysis simulating the insertion of a pipeline-like flow diverter mimicking a complete endovascular procedure highlighted the importance of retraction and pushing steps of the device to obtain maximal flow diversion and best apposition [222]. A CFD study validated *in vitro* showed that the stent configuration has a strong impact on the flow in the aneurysm dome, primarily due to strut protrusion [223], confirming the importance of a realistic virtual stent insertion.

An interesting SFE study on vessel ring geometry addressed the effect of the arterial clamping and validated it with an *in vivo* animal experiment [224].

2.9 Intracranial atherosclerosis

There are only few studies investigating cerebral stenosis. The reason is partially due to the limited resolution of stenotic lumen imaged by current imaging techniques which precludes the development of a realistic geometry for use in finite element modeling and CFD analysis [225]. CEMRI – based CFD modeling was used to determine WSS in one patient [225]. The authors reported an increase of WSS at the stenotic region and they suggested that the border zone infarct in the patient may have corresponded to thromboembolism that developed at the plaque surface under the influence of hypo-perfusion. This shows the main difference with larger arteries where the plaque vulnerability is more likely leading to stroke. Using pre- and post-stenting vessel geometries in one patient [226] a decrease in WSS has been shown after stenting which could predict minimal chance of restenosis and intimal hyperplasia [227]. The main limitation of the study was the lack of stent in the model.

2.10 Conclusion

Numerical analysis is gaining importance as a tool for clinical purposes. CFD, SFE and FSI allow studying different facets of and the interactions between the patho-physiological biomechanical environment and the risk of stroke. With the advancement in imaging techniques it is possible to acquire non-invasively the complex structure of pathological vessels and this under *in vivo* conditions. Numerical simulations allow to study the relationship of biomechanical factors with initiation and development of the disease leading to major catastrophic cerebrovascular events. WSS has an assumed important role in the first stages of atherosclerotic disease and possibly in the aneurysm formation, implying a role for fluido-dynamic analysis. Structural analysis has the potential to be a predictor of plaque rupture and could be involved in the risk stratification in the clinical arena. Also for patient treatment using endovascular devices, there is a possible role for numerical simulations in the choice of the treatment or the selection of the best device design according to the patient specific conditions. Nevertheless, the numbers of studies supporting the inclusion of numerical simulations in the clinical decision making process is still scarce and further *in vivo* validation is absolutely required. In addition, for efficient inclusion in clinical practice there are still some issues to be solved. Computational cost of the 3D simulation, especially involving fluid-structure interactions are a large hurdle

for diagnostic and procedure planning routine. Regarding assessment of plaque rupture there are missing tools for automated segmentation of the plaque components, which is still highly time consuming and operator dependent. Moreover realistic material properties and boundary conditions, ideally specific for the individual patient, are needed for a correct evaluation. Mesh generation is still highly challenging for complex *in vivo* structures and in the presence of endovascular devices. Image resolution is still suboptimal to retrieve correct geometrical information or information on the vessel wall structure in the cerebral circulation. An additional major issue is the lack of a reliable, well established strategy to include mechanobiology which can take into account the remodeling response of the vessel and could predict the long term effect of the mechanical changes in pathological conditions and in presence of devices.

2.11 Thesis rationale and outline

The investigation performed in this thesis was motivated by unsolved issues in CAS and stent-supported coiling, as discussed previously. Perioperative failure of the procedure can lead to catastrophic events whose causes are not yet completely clear. Finite element modeling can help understanding the interaction between the vessel and the device, and analyze conditions which are impossible or difficult to study *in vivo*.

The research shown in the following chapters aims to provide insights into the mechanics of the stenting procedure applied to intra and extracranial vascular districts, using both parametric and patient specific geometries and focusing on the geometrical descriptors of the device and the stented vessel as potential tools to evaluate the procedural outcome. Flow related wall shear stresses are not the focus of this work.

Previous work on the mechanics of stenting (see sections 2.8.3 and 2.7.3) has been limited by simplified parametric geometrical models and material properties, and though *in vitro* validation has been reported, *in vivo* studies are very limited. The *in silico* modeling performed in this thesis aimed to capture the behavior of the device during and after deployment hopefully helping paving the road for the use of numerical simulation as a predictive tool in procedure planning.

The work described in this dissertation is organized as follows:

- Advances in finite element modeling are described for the creation of both stent and vessel models and virtual stent placement strategies.

- A parametric study on anatomically realistic carotid models is performed to study the effect of plaque morphology and vessel pathological anatomy on the stenting procedure.
- *In vivo* pre- and peri-operative data of two patients who underwent carotid artery stenting were used to emulate the stenting procedure using finite element modeling. After validation of the numerical results, an analysis of clinically relevant geometrical parameters to evaluate the procedural outcome is performed.
- Three patient specific aneurysmatic cerebral vessels were virtually treated with three stent designs. The deployed configurations were compared highlighting different effects of closed and open cell devices.
- Finally, the previous stenting methodology (designed for an optimal stent insertion) is adapted to account for collateral effect of one specific stent design reported in clinical studies. A patient specific aneurysm was virtually treated and post-operative CT scans were used to validate the finite element results.
- The main results of this research are summarized and conclusions are drawn providing guidelines and advices towards future research on virtual stenting.

Two

Advances in modeling strategies

CHAPTER 3

Advances in modeling strategies

The first step to be taken for the mechanical simulation of the endovascular procedure is the reconstruction of both the design of the device employed and the vessel geometry as well as their realistic mechanical behavior. Adequate strategies for virtual stent implantation are also an important step for the reliability of the numerical results. In this chapter the methodologies adopted to overcome these issues are described.

3.1 Stent modeling

3.1.1 Building a stent

Stent geometries used in this thesis have been retrieved from 3D models of the real device when samples where available, analytically or from image sources otherwise. The pattern of the stent meshes for endovascular peripheral treatment (normally laser cut from a cylindrical metallic tube), can often be easily identified by a repetitive cell unit. However, latest generations of stent designs have more complex shapes to improve design performance and undergo mechanical treatments to further modify the shape of the device in order to improve specific features. A typical example is the tapering of the stent to follow the natural narrowing of the vessels moving downstream the peripheral vasculature and after branch splitting (typically used for carotid stents e.g. Acculink stent - Abbott Vascular, Boston, IL, Cristallo Ideale - Medtronic, Minneapolis, MN,

etc) and provide proper sizing along the vasculature. Another example is the use of flaring ends to enhance apposition to the wall (e.g. the Enterprise stent-Cordis Corporation, Miami, FL) [228]. These methods can modify the original pattern of the stent, complicating the task of deriving the initial parametrized design and simulating the actual technological procedure especially with geometries which are not created by the replication of few repetitive units. For this reason the strategy adopted in this thesis is to draw and analytically modify the stent geometry without emulating the mechanical process leading to the final shape.
All available devices were scanned by the center for X-ray tomography UGCT (`http://www.ugct.ugent.be`) using X-ray micro-tomography (μ CT). This non destructive imaging technique uses X-rays with stationary source and detector to create cross-sections of an object (rotating during the scan) with resolution in the micrometer range. The final dataset of stacked 2D images is further processed to build a 3D virtual model using common segmentation programs, such as the open source program 3Dslicer (`http://www.slicer.org/`). Thanks to the high quality of the images due to the high contrast between stent and air, the stent geometry can be easily segmented by choosing an appropriate threshold for the intensity levels of the images. Normally the threshold was chosen to give thickness and width dimensions which matched measurements retrieved by more accurate techniques, in particular optical microscopy, retrieved from literature studies or from internal facilities. Direct user corrections are sometimes needed to remove scattering artifacts of the radio-opaque markers.

The result of the segmentation is a 3D model of the stent which is then exported as a 3D triangulated surface (STL). The STL is processed in pyFormex (http://www.pyFormex.org) to virtually longitudinally cut and unroll the geometry using a cylindrical coordinate transformation in order to retrieve the flattened mesh of the stent laying on a single plane in a bi-dimensional coordinate system. This then serves as drawing basis to trace the computational model (Figure 3.1A and B).

While the mentioned operation results in a 2D pattern for cylindrical stents, additional transformations are needed for tapered or flared stents. The tapered stent will result in a 2D flat pattern rotated in 3D on the longitudinal plane with an angle depending on the tapering. In this case the flat geometry can be easily rotated to be aligned with the longitudinal direction. The flared stents, instead, result in a more complex 3D pattern which needs further adjustment. The adopted strategy is to find an analytical description of the flaring to translate the points of the flares on the bi-dimensional plane (Figure 3.1B).

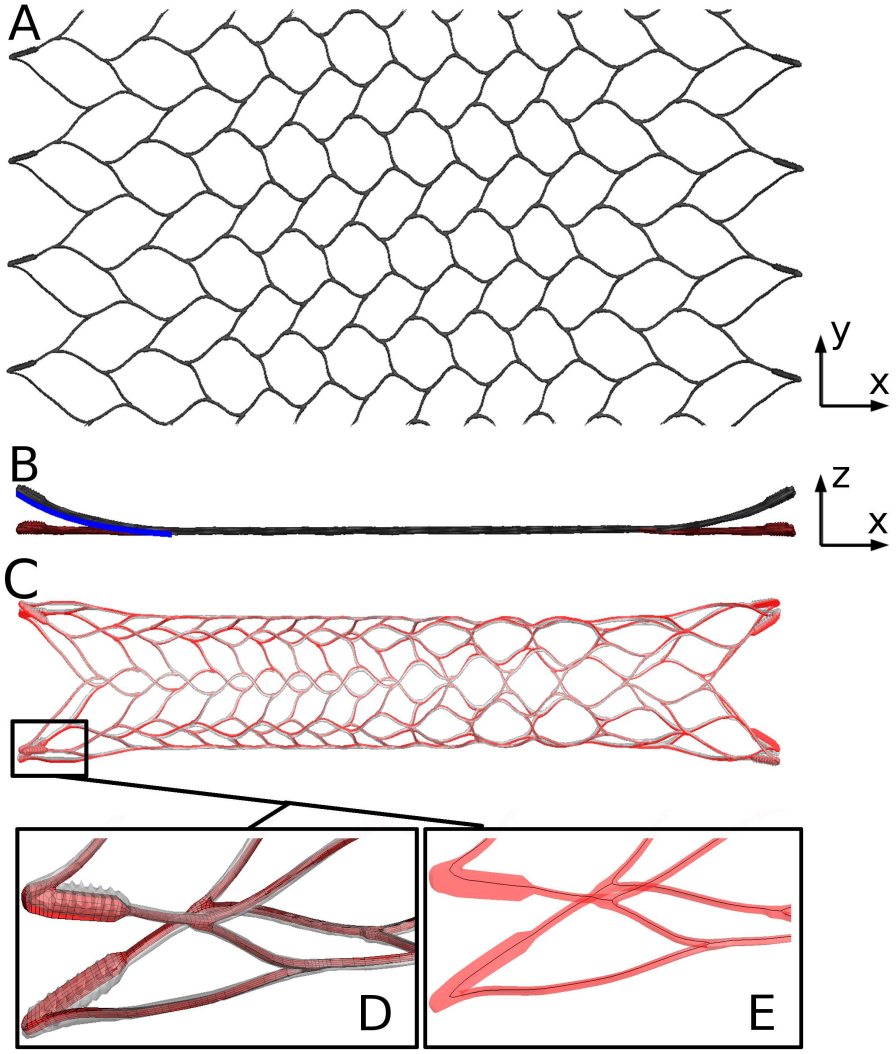

FIGURE 3.1: Processing of a scanned device with flairs at its endings to create the computational model: *A* Unrolled stent in the XY plane; *B* Unrolled stent in XZ plane. The black profile is derived from to cylindrical transformation. The flared curvature is approximated with an analytical function (blue line) which is used to compute the distance to the XY plane to flatten the pattern (red profile); *C* Superposition of the real device geometry (light gray) and the meshed stent(red); *D* Detail of the superposition of the real device geometry (light gray) and the meshed stent(red); *E* Peeling of the original hexahedral numerical model (in red), to obtain its centerline to be modeled as beam elements.

When the STL of the device was not available other strategies were used, in particular following an analytical description of the device or images of the unrolled stent available in literature. This was the case when a repetitive pattern was identifiable allowing a simple parametrization of the stent.
Once the 2D drawing pattern is obtained, the creation of the 3D stent models for the numerical simulations was performed in pyFormex following and improving the approach used in previous works [170]. In order to simplify the reconstruction of the stents a library of predefined shapes was built based on bezier splines. The use of spline functions allow a high flexibility and versatility to adjust the curvature of the struts and to create connectors among the struts (Figure 3.2A). Providing the initial and the final point of the centerline of the struts and controlling the initial and final direction of the spline, a wide range of curved struts can be obtained as shown in Figure 3.2B. The splines are then approximated by piecewise polyline and the final struts are modeled by sweeping the desired section along the centerline pattern. The local tangent of the centerline is smoothed to provide a gradual transition of the sections directions. This guarantees the quality of the element shape which can otherwise introduce inaccuracies in the mechanical simulation (Figure 3.2B).

Connectors between the struts (Figure 3.1B) are created automatically by getting the vertices of the struts, computing the normals of the line joining the vertices of a single strut and finally connecting the adjacent points with bezier splines. Starting and ending tangent control the direction of the spline. In addition a parametrical tip has been created to allow strut connection of the cell crowns (Figure 3.1B).

With these three basic shapes it was possible to model all the stent designs studied in this thesis.

Note that the use of splines simplifies a common CAD design pipeline. Actual measurements of curvature angles or circle radii are not taken into account during the design process but they are only controlled through the spline parameters. Defining analytical relations among to the distances of the stent cells allows automation of the strut centerline creation, speeding up the design process. In this way it was possible to have a good approximation of the real stent geometry that, as mentioned before, might suffer from (small) deviations from the original design due to the manufacturing process.

Once the pattern was traced, opportune rotations or flaring and inverse cylindrical transformation operations allowed to obtain the final

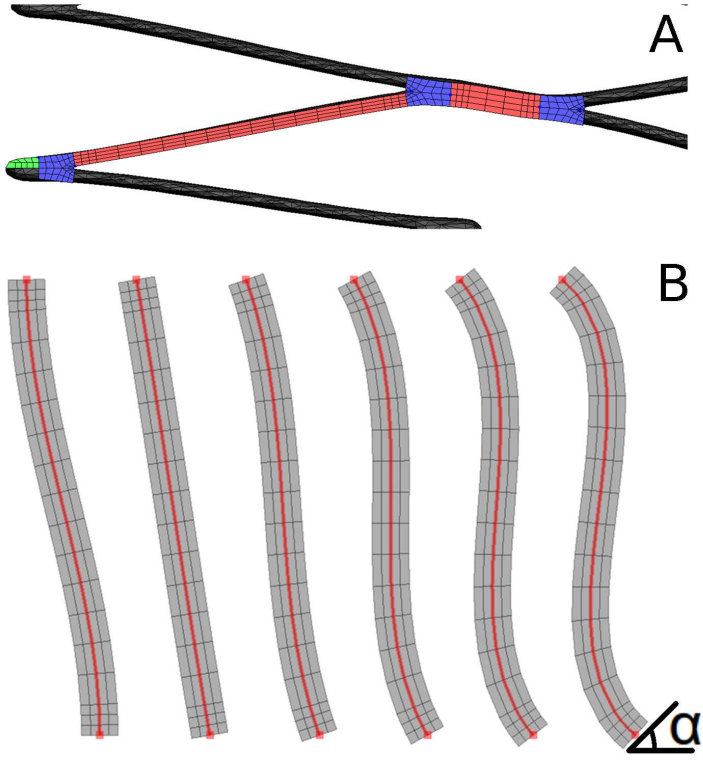

FIGURE 3.2: Stent meshing technique: *A* Library of the predefined shapes: linear struts (in red), struts connectors (in blue) and tips (in green); *B* Different shapes of the stent struts obtained by changing the initial angle α of the strut centerline (in red).

3D stent model with a highly accurate replication of the original device (Figure 3.1C and D). Additional operations on the final hexahedral model can be performed to "peel" the mesh in order to retrieve the centerline of the stent and convert the solid elements to beam elements as shown in Figure 3.1E.

Though the strategy allows for a high flexibility in the stent design, the procedure is far from being automated and requires substantial manual interaction. On the other hand, it is a relatively fast technique for accurate modeling of the device sample with a ready-to-use mesh for computational simulations.

3.1.2 Insertion of the stent

To model the stent insertion an efficient strategy has been developed. Two deformable sheets acting as the stent delivery system were used to simulate the catheter which holds the stent before the implantation and the guidewire along with the catheter slides to guide the stent to the target lesion. The deformations of the stent occur through displacement driven contact with these sheets.

The problem is approached analytically by virtually defining the nodal displacements of the catheter and the guide-wire through dedicated user defined ABAQUS subroutines (DISP and VDISP) which allowed to control the complete deployment procedure.

Two different insertion methods were developed. A first simplified and more efficient strategy, depicted in Figure 3.3, includes:

- Reduction of the catheter radius around the stent to simulate the crimped state of the device in the delivery system prior to the implantation;
- Simultaneous bending of the catheter and the guide-wire along the vessel centerline to position the stent inside the artery;
- Gradual expansion of the catheter from the distal end to release the stent inside the vessel.

A second version of the same code which allowed a more realistic simulation of the procedure (Figure 3.4) includes:

- Crimping of the catheter as described above;
- Bending of the guide-wire along the centerline of the vessel;
- Pushing of the catheter along the guide-wire to advance the stent inside the vessel until the implantation site;
- Catheter retrieval to allow the stent expansion inside the vessel;
- Guide-wire retrieval.

A dedicated user interface was coded to provide the input parameters of the subroutine. The vessel centerline, used to drive the motion of the catheter and the guide-wire, is computed using the open source program vmtk `http://www.vmtk.org/`. Using pyFormex it was smoothed using

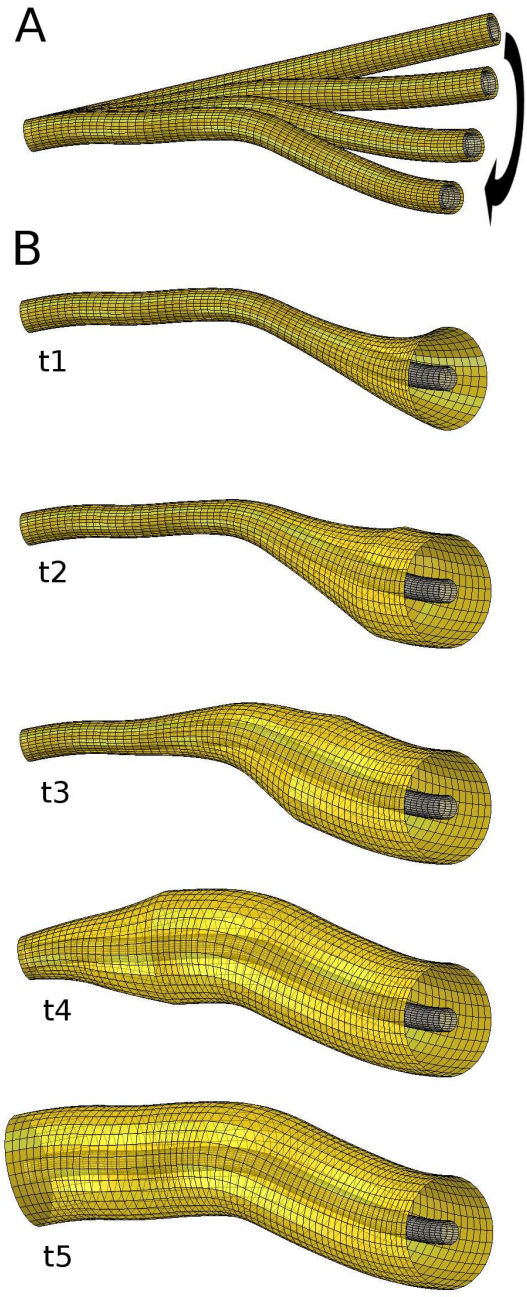

FIGURE 3.3: Schematic overview of the simplified delivery technique. *A* Bending of the catheter along the simulation; *B* Gradual opening of the catheter at different time steps.

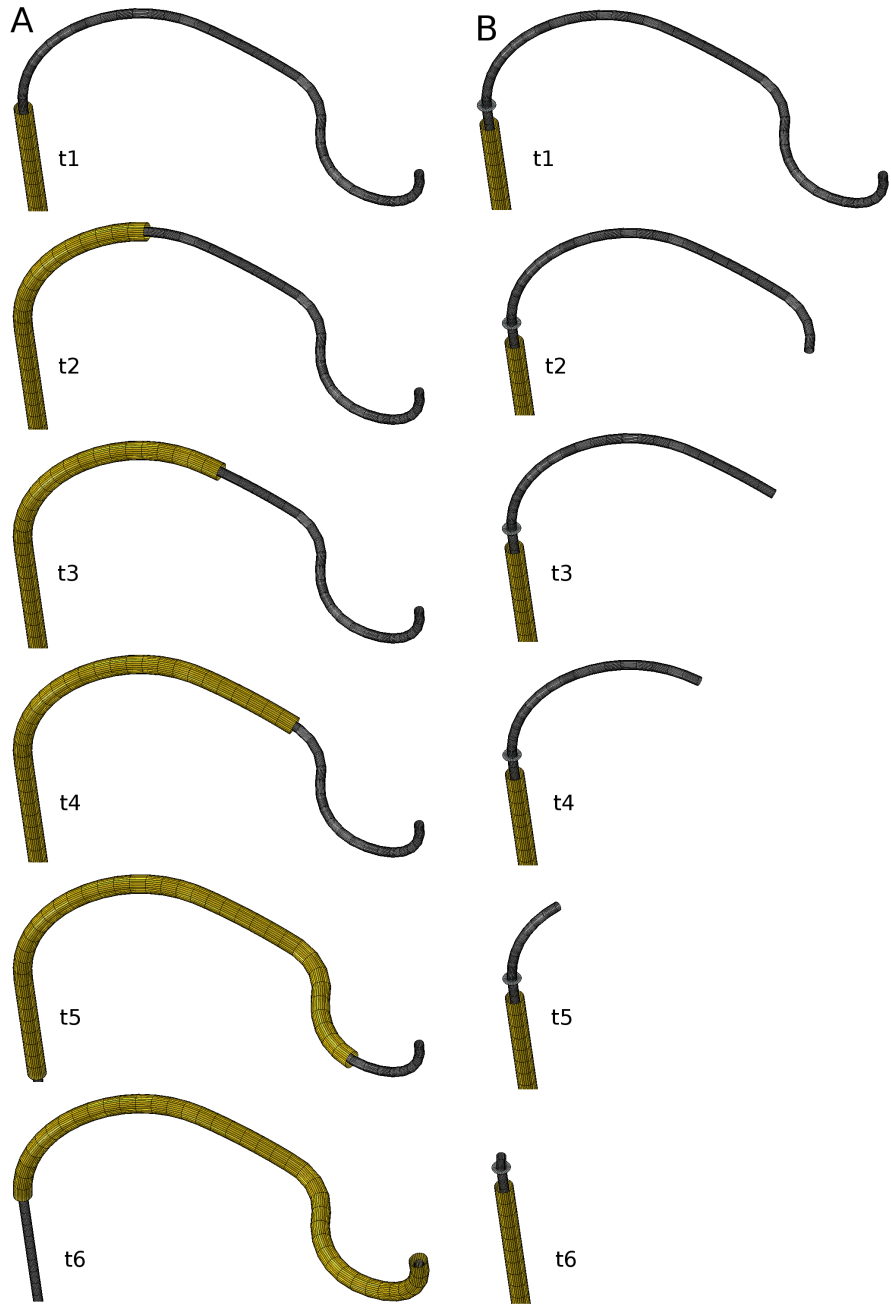

Figure 3.4: Schematic overview of the realistic delivery technique. *A* Pushing of the catheter (in yellow) over the guidewire (in gray). The pulling back of the catheter follows inverse displacements; *B* Gradual retrieval of the guidewire at different time steps.

a NURBS approximation and cut at the initial and the ending points chosen for the stent insertion. The centerline is then re-sampled using polylines with a number of points sufficient to avoid discretization error. The choice of the number of points depends on the tortuosity of the vessel and the relative length of the stent. The cases studied in this thesis were typically discretized with a minimum of 50 segments. Finally the centerline is rotated to have the first polyline segment oriented in the Z-direction.

Then the centerline is approximated with circular arcs in order to have its complete analytical description. However, the approximation is not automatic and requires user dependency. As shown in Figure 3.5, through the user interface, a plane is moved through the points of the centerline. A circular arc is fitted between the initial and the end point of the selected portion. When the user, by visual inspection, retains that the centerline segment is adequately estimated by its planar approximation, the input parameters of the subroutine are stored. The remaining portion of the centerline is oriented again to the Z-direction, and the operation is repeated. Subsequent regions are processed until depletion of the segments.

The information stored will be used as input for the subroutine. A schematic illustration of the parameters needed for the subroutine to impose the displacement to the virtual delivery system is shown in Figure 3.6:

1. Full length of the approximated centerline to define the length of the catheter/guide-wire;

2. Length L_i of each portion of the approximated centerline;

3. Bending angle γ_y of each portion, i.e. the curvature angle of the segment on the plane laying on the Z-direction;

4. Rotation angle γ_z of each portion with respect to the previous one to set the direction of the bending for each segment.

The final bending radius R_b of each segment is derived from the length of the centerline portion L_i and the final bending angle γ_y. The decrease of the bending radius R_b is controlled at each time increment $t_{current}$ during the simulation until the final time step t_{final} by the following equation:

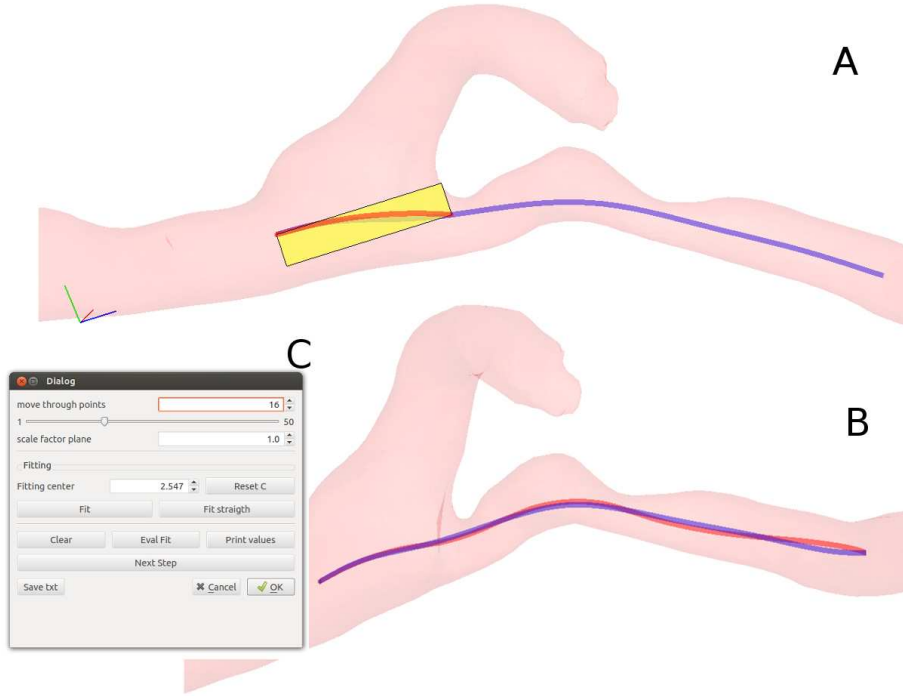

Figure 3.5: Environment for the analytical approximation of the centerline. *A* Moving plane for the visual evaluation of segment planarity; *B* Final approximation (red line) of the original centerline (blue line); *B* User interface for the centerline approximation showing main features.

$$R_b = \frac{L_i}{\gamma_y} \frac{t_{final}}{t_{current}} \tag{3.1}$$

There are some advantages linked to this strategy. First, it helps the convergence of the contact algorithm in ABAQUS, as the smooth changes in the deformed configuration avoids abrupt differences in the contact surface distances and contact status. Second, the subroutine only needs a few parameters, provided by the dedicated pyFormex user interface, to fully describe any specific case. This means that, given a stent and vessel models, the pre-processing time needed to set the displacements of the catheter and guidewire, only depends on the analytical fitting of the centerline. This operation takes only few minutes, speeding up the pre-processing when multiple configurations have to be tested. This is the case with *in vivo* validations, which require several tests to match

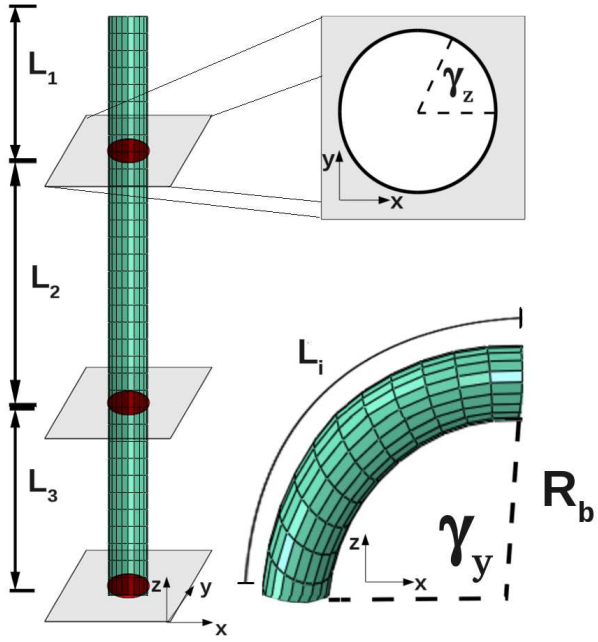

FIGURE 3.6: Parameters of the bending procedure: The catheter is discretized in segments of length L_i. Bending angle γ_y and bending radius R_b control the final deformation of each segment while γ_z set the direction of the bending for each segment.

the stented location as seen in the clinical outcomes (as in chapter 5 and 7).

The methodology is very versatile and it has been used also in other vascular districts [229].

When the pulling and retraction of the catheter is simulated, the initial settings of the subroutine remain the same. However the final geometrical parameters (such as the bending radius) are not changed over the time step. The current time step of the simulation is used to control the position of the catheter along the centerline and to check at which portion of the centerline it should belong. This methodology offers a more realistic replication of the actual delivery procedure. Though, this advantage comes at cost of computational time. Fast simulations can suffer of unrealistic deformations by compacting the stent while retrieving the stent-carrying catheter.

The choice between the two approaches was lead by the effects of the delivery procedure. From the literature study performed in this

thesis, while for carotid treatments the delivery procedure has never been reported to have an impact on the stent configuration, it can be crucial when cerebral aneurysms are treated with coils supported by specific stent design which can experience incomplete strut apposition [218] as shown in chapter 7.

3.2 Vessel modeling

For the purpose of this thesis different approaches were used for the construction of the vessel models. Initially, an in-house developed code was used for vessel meshing (as in chapter 6 of this thesis) which was proven to be able to create high quality hexahedral structured meshes for the fluid domain [89]. However, the lack of automation and interaction with the viewport made the code not suitable to be used with complex vessel shapes especially when the algorithm needed to be adapted for structural models where the vessel wall had to be meshed. In particular stenosed vessels can exhibit very different shapes between the lumen and the external wall hampering the control of the hexahedral element quality. According to the author no code commercial or in-house is available for automatic meshing of hollow geometries (such as vascular structures) starting from already available STL geometries. For this reason strategies for meshing the arterial wall were developed and the problem was approached in two different ways depending on whether the vessel model is patient specific or parametric.

3.2.1 Parametric vessel models

The lack of accurate stenotic bifurcation carotid models, both from the anatomically and morphological point of view, had motivated the creation of a realistic parametric finite element model. Only one *in silico* model of carotid bifurcations emerged from the literature study [167]. From the paper it is clear that the condition were not addressable for stenting considering current treatment guideline derived from major clinical trials [10, 34, 35]. The stenosis (56%) was computed based on the lumen area which corresponds to a 33% stenosis according to NASCET or ECTS criteria using the reported diameter dimensions.

The model developed in this work was entirely built in pyFormex and a dedicated script was coded to create a geometry consisting of a common carotid artery branching into the internal and external carotid arteries. The vessel wall was modeled with different layers to take into account the heterogeneous composition of the artery. The internal carotid

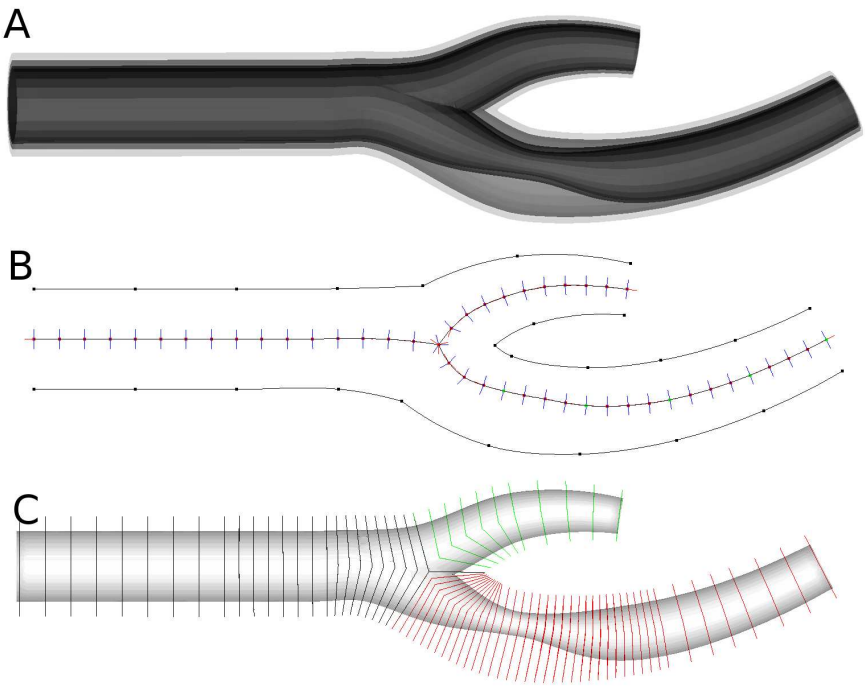

FIGURE 3.7: Initial setup for the creation of the parametric model: *A* Creation of the STL geometries for each layer; *B* Computing the tangential and perpendicular direction of the centerline point to define cutting planes directions; *C* Cut arcs of vessel shells.

artery contains a stenosis. The model is fully parametric, with the most important parameters being length and wall thickness of the common carotid and its branches, length and minimum diameter of the stenosis and lumen shape (circular or ellyptic).

First the centerlines from the common carotid to the two branches were traced using Bezier splines. A circular section was swept along the patterns creating two tubular structures, each one representing the common carotid elongated to one of its branches. Angles and curvatures were adapted from a patient specific case. However, by changing the directions of the centerlines other anatomies can be created.

The sections were tapered along the pattern to emulate the natural narrowing of the arteries towards the peripheral region of the vascular tree. Using the gts library (`http://gts.sourceforge.net/`) the tubular structures, converted to STLs, are merged to obtain the vessel geometry.

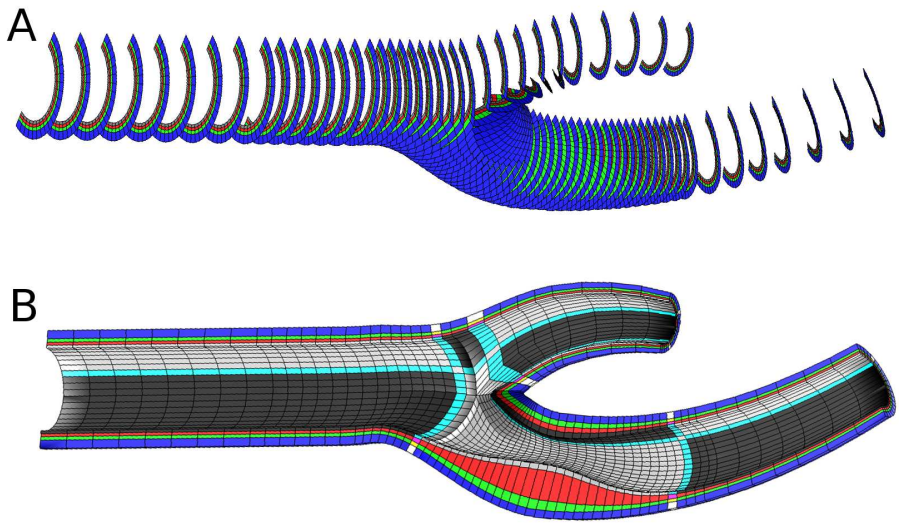

Figure 3.8: Creation of the initial coarse mesh. *A* Section of the vessel wall obtained by connecting the cut arcs in the radial direction; *B* Connection of all the sections to built the hexahedral mesh. Similar color identify regions that will be re-sampled with same number of subdivisions.

The operation was repeated by adjusting the section radii to build the outer vessel layer, i.e the shells identifying the adventitia.

For the lumen, the diameter reduction of the stenosis needed particular attention. The location of the stenosis was chosen in the internal carotid artery. The section at the narrowest blockage site was set to have a radius with the desired degree of stenosis with respect to the non deseased lumen section. For the presented case the degree of stenosis was 85% computed on the lumen area and a stenosis of 61% according to the ECTS criteria presented in chapter 1. The centerline at the occlusion was translated to account for plaque eccentricity. Choosing the length of the blockage site, the radius of the stenosis was symmetrically enlarged until restoring the original lumen. In order to have a smooth transition from the lesion to the non diseased lumen, the radius was increased with a Gaussian function. The mean of the function represents the position of the maximum stenotic location on the centerline, the standard deviation controls the length of the lesion, while the peak value describes the maximum protrusion of the plaque from the "pre-lesion" lumen.

Different shells were included in the model, hence defining different layers in the arterial wall: the external vessel wall, the adventitia/media-

intima interface, the media-intima/fibrous cap layers, the lumen of the vessel (Figure 3.7A).

Once all the STLs of each interface between two different layers were created, they were processed to obtain the final hexahedral finite element mesh. The centerlines were discretized with polylines. The density of the discretization controlled the density of the final hexahedral mesh in the longitudinal direction. The direction of every segment, previously smoothed to allow a more gradual transition of the normals, was used to determine the position of the cutting planes which were used to slice the STLs (Figure 3.7B and C). This cutting operation resulted in a series of polyline slices. The slices were re-sampled with the same number of segments to ensure correspondence of their connectivity and finally joined along the radial direction to obtain the vessel sections (Figure 3.8A). Next the section meshes (composed of quadrilateral elements) were connected in the longitudinal direction to create a first coarse hexahedral mesh with only one element per layer in the radial direction (Figure 3.8B). A smart selection of the vessel mesh districts allowed to increase the element density at the region of interest while providing a coarser seeding elsewhere (Figure 3.9A). For this purpose a function for a uniform element subdivision was coded and special element subdivision is performed to create transition regions between different element densities parts as shown Figure 3.9B and C.

3.2.2 Patient specific vessel models

The previous approach can be convenient with parametric models where the equations describing the vessel layers are known. When dealing, however, with complex 3D patient specific structures which can exhibit more tortuous patterns, it is hardly adaptable and other strategies need to be used. Block-structured techniques can be employed to generate structural meshes when dealing with geometries with non-trivial boundaries such as anatomical domains. The domain is broken up into topological blocks (see Figure 3.10) allowing for geometric flexibility while retaining computational efficiency. The open source mesher IA-FEMesh (`http://www.ccad.uiowa.edu/`), based on this technique, accelerates the development of anatomically correct finite element models, also thanks to the integration with the 3Dslicer graphical environment. This tool, however, is limited to the creation of surface or bulk meshes from closed STLs. Meshing of the vascular wall can then be very tedious and time consuming, because it will require the positioning of the blocks around the sectors of the vessel wall. A strategy to recycle the capability

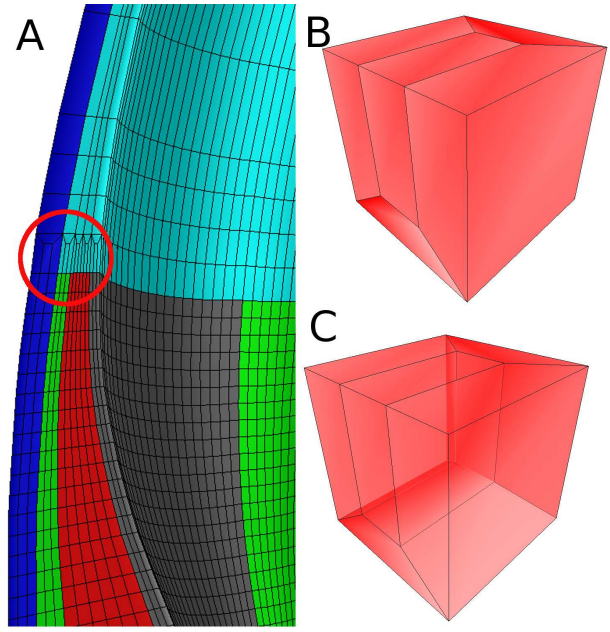

Figure 3.9: Final seeding of the parametric carotid models. *A* The coarse mesh has been re-sampled with different element densities. The red circle surrounds transition elements between this regions; *B* and *C* Structure of the transition elements.

of IA-FEMesh for this purpose is hereby proposed, in combination with pyFormex. The strategy is meant for the reconstruction of the vessel wall when different vascular layers are provided. It also allows to include different diseased regions.

The procedure can be schematically summarized in the following steps:

1. The multi-block structure is created in IA-FEMesh around the inner surface of the vessel wall (Figure 3.10A);

2. The quadrilateral mesh of the outer surface of the vessel wall is exported by choosing an adequate number of subdivisions for the block discretization;

3. A copy of the previously created multi-block structure is now adjusted around the lumen surface by repositioning the nodes of the blocks on the new surface (Figure 3.10B);

4. The quadrilateral mesh of the lumen surface is exported using the same parameters used for the outer wall;

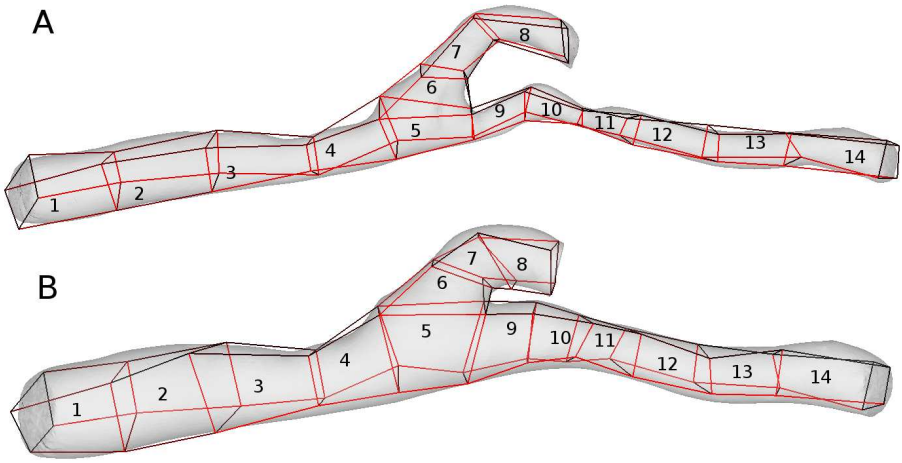

FIGURE 3.10: Multi-block structures created in IA-FEMesh: *A* Blocks are built around the patient specific lumen; *B* Keeping the same structure topology, the nodes of each block are adjusted around the STL of the external surface of the vessel.

5. The two meshes are imported in pyFormex and connected to create the hexahedral mesh. The use of the same multi-block topology, and the same number of subdivisions will ensure correspondence of the connectivity tables of the quadrilateral meshes (Figure 3.11A);

6. Eventual additional mesh improvement (such as smoothing and mesh refinement) is performed (Figure 3.11B and C). Special functions for element splitting and subdivision are implemented. This allows reducing the seeding of the IA-FEMesh meshes to avoid possible problems of mesh quality of the hexahedral mesh after connecting the quadrilateral geometries. If the quadrilateral meshes are too fine, intersections can occur leading to negative volumes, badly shaped elements (which can introduce inaccuracy of the FEA results) or small sized elements (which can increase computational times);

7. The elements of the mesh to which to assign the plaque material are selected by testing the points falling inside the STLs geometries of the plaque (Figure 3.11D).

As the outputs of the mesher are in the open source Visualization ToolKit (VTK) format (`http://www.vtk.org/`) a dedicated interface

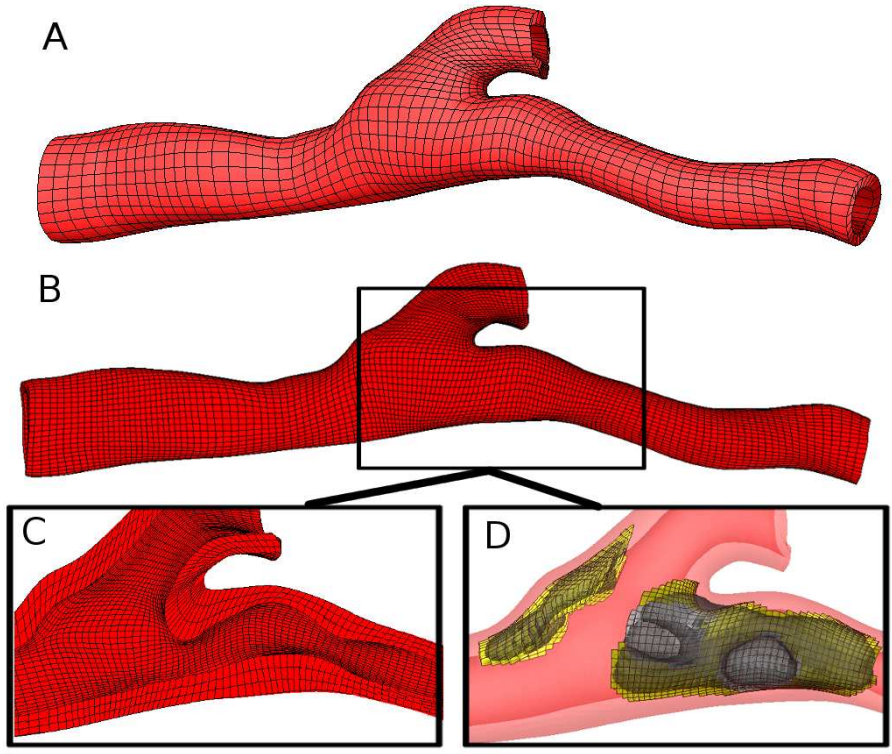

Figure 3.11: Processing of the quadrilateral meshes obtained in IA-FEMesh. *A* Quadrilateral meshes of the inner and outer surface are connected in pyFormex to create the hexahedral mesh; *B* The final mesh is smoothed to improve the element quality and refined by element subdivisions; *C* Detail of a longitudinal section of the final vessel mesh; *D* Selection of the elements laying in the diseased regions of the vessel wall.

has been coded in pyFormex to allow for the interaction with the resulting formats of the meshing tool. All the implemented function to recognize points inside a closed object and to perform the mesh subdivision are made available in pyFormex. This hybrid open-source environment can thus be a powerful tool for patient specific finite element vascular modeling.

Three

Virtual carotid artery stenting

CHAPTER 4

The influence of vascular anatomy on carotid artery stenting : a parametric study for damage assessment

The modelling strategies described in the previous chapter are applied in this chapter to a parametric study to assess the influence of plaque morphology and composition on carotid artery stenting. Particular attention is devoted to the potential damage of the artery due to the procedure. The results of this study have been published in :
"The Influence of Vascular Anatomy on Carotid Artery Stenting: A Parametric Study for Damage Assessment." Iannaccone, F., N. Debusschere, S. De Bock, M. De Beule, D. Van Loo, F. Vermassen, P. Segers, and B. Verhegghe. *Journal of Biomechanics, (2014)* [230].

4.1 Introduction

Atherosclerotic cerebrovascular diseases, in particular carotid artery occlusive disease, have been estimated to be responsible for about 20%of all ischemic strokes [27,231], the second major cause of death and morbidity worldwide [22]. Carotid artery stenting (CAS) is emerging as an alternative technique to surgery [232]for the treatment of severe carotid stenosis

(>70%) in an elective patient population. The minimally invasive nature of the procedure, the lack of need for general anesthesia and the increased number of trained physicians contribute to the introduction of CAS into routine clinical practice [233].

Nevertheless both short- and long-term efficacy of CAS is debated and the causes which lead to procedural failure are yet not completely understood [37,163,164]. The peri-procedural risk of stroke is high [163] and multi-center randomized trials demonstrated that the incidence of restenosis is higher at one year compared to the surgical counterpart [234].

Severe restenosis were strongly dependent on poor initial results, mostly attributable to inadequate early angioplasty techniques which were also suspected to induce neointimal hyperplasia due to excessive dilation of the vessel. Thus, a balance is needed between post-implant stenosis and vessel dilation [165]. These clinical results seem to support the hypothesis that restenosis is related to tissue injury and response due to local stress concentrations which initiate the remodeling process leading to re-occlusion of the vessel [64,235].

Currently, interventional diagnosis is based on the degree of luminal stenosis and plaque severity [34–36,236]. However, the degree of stenosis alone may not adequately reflect the risk associated with the lesion. High-risk vulnerable plaques are characterized by a large necrotic lipid core, a thin overlying fibrous cap and ulceration while large calcifications seem not to be related to stroke symptoms [131,132]. Plaque vulnerability is extremely important in the context of CAS, where the plaque is manipulated by the endoluminal devices [237]. Large randomized trials have shown that the incidence of peri-procedural major adverse events increases with age [238,239]. In elderly patients larger lipid cores, and more calcified plaques are present as compared with younger patients who show more fibrotic plaque tissue [239]. High prevalence of lipid cores is associated with higher risk of embolism during and after CAS [240] and superficially calcified lesions could potentially embolize during stent deployment causing stroke [67].

Numerical simulations seem promising in assessing the plaque rupture risk. Thanks to advances in diagnostic imaging, plaque composition is now detectable *in vivo* allowing for the reconstruction of patient specific models for numerical analysis. Fluid-structure interaction and structural finite element analysis (SFEA) of *in vivo* MRI based atherosclerotic carotid models were able to relate sites of rupture with plaque structural stresses [141], differentiate ruptured and unruptured

plaques [147, 152, 153], refine risk stratification among symptomatic patient with/without hemorrhage or thrombi [153], correlate plaque stress and lumen curvature [145, 151] and correlate biomechanical structural stresses with ipsilateral cerebrovascular ischemic symptoms [156]. Stress concentration was found to occur at the shoulders and at the thinnest fibrous cap regions while thicker fibrous caps prevent high stresses in the lipid core [144–146]. Computational frameworks have also been used to analyze the impact of different stent designs and interventional techniques on the outcome of endovascular procedures in various vascular districts [97, 167, 168, 179].

However, the effect of anatomical differences and plaque composition on endovascular procedure outcomes has been rarely studied [241]. The majority of the aforementioned studies suffers of different limitations: 2D or simplified 3D geometries not taking into account the complex plaque morphology, inadequate material descriptions which do not reflect the anisotropic behavior of both diseased and healthy tissues [242] which lead to significantly different results compared to isotropic material models [243]. The assumption of an anisotropic model can be sufficiently general to study the pathophysiological atherosclerotic condition [99] but over-stretching of the artery induces damage which can influence the biomechanical interpretation of the interactions between vessel and devices [244]. Thus, procedure related conditions and adequate anatomical and material models challenge a complete accurate computational analysis that captures the correct mechanics of the interventional procedure.

In order to gain further insight on CAS, a virtual environment based on SFEA was built to emulate the stenting procedure on generalized carotid models with inhomogeneous plaque composition focusing on anatomical changes. Different morphology and composition of the atherosclerotic plaque (lipidic, fibrotic, calcified) were considered, incorporating a damage model to describe the vessel injury due to the angioplasty and stenting procedure.

4.2 Materials and methods

4.2.1 Mesh generation

4.2.1.1 Carotid models

Three realistic carotid bifurcation models were created using the open-source script based program pyFormex (`http://www.pyFormex.org`) using the strategy described in detail in chapter 3. For all models, a fixed

diameter of 7 mm was chosen for the common carotid lumen, while internal and external carotid diameters were smoothly reduced to 5 and 4 mm respectively [245]. Vessel wall thickness was assumed to be 30% of the lumen diameter [112]. The geometries were designed to have an eccentric plaque with minimum cross-section area of 15% of the original lumen (corresponding to 85% stenosis) and 20 mm length. The stenosis is smoothly reduced until restoring the normal diameter using a normalized gaussian shaped function. Only two layers were considered for the healthy vessel (adventitia, media-intima) in order to apply experimentally derived material model data [112], while fibrotic media, lipid pool, fibrous cap regions were considered for the lesion. Assuming a circular vessel shape with a fibrous cap of 0.25 mm as baseline, the other geometries were modified i) to increase the fibrous cap to 0.5 mm and ii) create an elliptic lumen shape (to account for lumen curvature changes) as shown in Figure 4.1 and Figure 4.2. The mesh was generated with 76200 hexahedral elements. The density of the elements was increased at the plaque location, while coarser seeding was applied elsewhere (Figure 4.1). Sensitivity analysis was not performed as the number of elements was almost 6 times higher than a previous study on carotid artery stenting [168] which demonstrated the 13000 elements were sufficient for accuracy of the stress analysis. Moreover the smart seeding guarantees a higher number of elements at the stented location, increasing the accuracy of the results in this location.

4.2.1.2 Material model

To mimic the mechanical response of the diseased vessel, we implemented the anisotropic hyperelastic constitutive model proposed by

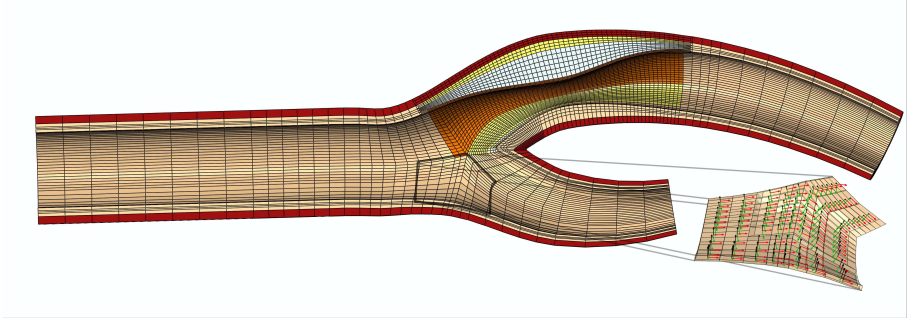

Figure 4.1: Axial section of the baseline model with a detail of the element's local coordinate system.

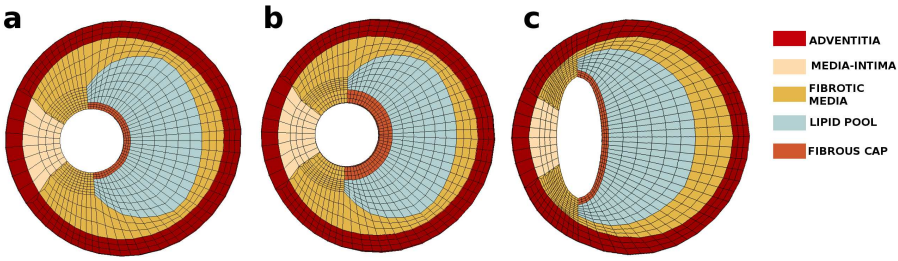

FIGURE 4.2: Cross-sections of the internal carotid artery of *a* the baseline , *b* increased fibrous cap thickness and *c* elliptical shape. The legend indicates the different material regions considered in the model.

[246] in a dedicated ABAQUS subroutine (VUANYSOHYPER) to define anisotropic materials . This model describes the hyperelastic strain energy function Ψ as the addition of the isotropic contribution of the tissue matrix Ψ_{mat} and the anisotropic contribution Ψ_{fib} of two families of collagen fibers Ψ_{fib_4} and Ψ_{fib_6} described by the following equations:

$$\Psi = \Psi_{mat} + \Psi_{fib} \tag{4.1}$$

$$\Psi_{mat} = C_{10}(I_1 - 3) \tag{4.2}$$

$$\Psi_{fib} = \sum_{i=4,6} \frac{k_1}{k_2} exp(E_i) \tag{4.3}$$

$$E_i = (1-\rho)(I_1 - 3)^2 + \rho(I_i - 1)^2 \tag{4.4}$$

where C_{10}, k_1, k_2 are material parameters and ρ controls the dispersion of the fibers. In this representation, a value of $\rho = 1$ means that the fibers are fully dispersed and do not show any preferential orientation resulting in an isotropic model, while a value of $\rho = 0$ represents the ideal case where all fibers are aligned. To allow for an explicit solution scheme in the finite element solver ABAQUS, a dilatational component Ψ_{dil} was added to the strain energy function Ψ :

$$\Psi_{dil} = \frac{1}{D}\left(\frac{J^2 - 1}{2} - ln(J)\right) \tag{4.5}$$

where J is the elastic volume ratio and D is a parameter dependent on the bulk modulus. To account for the rupture of collagen fibers upon

stretch, we included a damage model as described by Famaey et al. [224] motivated in previous studies [244]. In this model, Ψ_{mat} and Ψ_{fib} are multiplied by a scalar damage value $1 - d$:

$$\Psi = \sum_{i=mat,fib_4,fib_6} (1 - d_i)\Psi_i \tag{4.6}$$

where d_i is function of the undamaged strain energy :

$$d_i = \gamma_i \left(1 - exp\left(\frac{-\beta_i(\Psi_i)}{\tau_i}\right)\right) \tag{4.7}$$

$$\beta_i = sup(\Psi_i^t) - \Psi_i^{ini})\forall t \tag{4.8}$$

In these expressions, β_i keeps track of the maximum occurrence of the undamaged function Ψ_i^t and Ψ_i^{ini} is an initial offset. The maximum value of the damage is determined by γ_i, whereas τ_i is a scaling constant.

The parameters of the vascular material models were taken from literature for both the healthy carotid [247] and the atherosclerotic components in iliac arteries [242]. The lipid pool was considered as a butter-like material while the calcifications were assumed to be a stiff ceramic-like material, as suggested by [242]. Table 4.1 and Figure 4.3a, b, d resume all the materials used in the model. The values of D for the dilatational part were set to obtain a poisson ratio of 0.475 [248]. Though in the mentioned studies the angle (Table 4.1) between the collagen fibers (considered arranged in symmetrical spirals [249]) and the circumferential direction was derived from an optimization process without a histological comparison. Local material orientations needed to orient the fibers were calculated per element (that due to the modelling strategy are aligned in the longitudinal direction) and locally averaged to avoid discontinuous orientations (Figure 4.1).

4.2.1.3 Material damage model calibration

To calibrate the constants of the damage model a similar approach as described by [224] was used. A first simulation was run on the baseline geometry to record the initial values of the strain energy for the matrix and the families of fibers. Differently from [224], who set the threshold to a physiological systolic pressure (SP) we considered a more conservative model hypothesizing that damage only occurs at the double of a SP of 120 mmHg (i.e. 240mmHg). Lacking experimental data to fit the model, we assumed that 95%of the "damageable" part of the material is

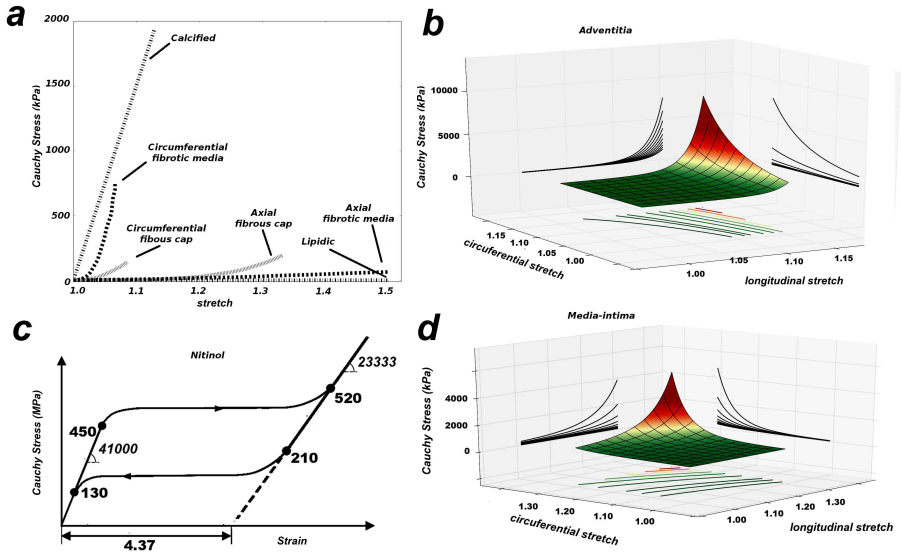

FIGURE 4.3: Curves describing the material behaviors for the stenting procedure. Experimental data of axial and circumferential uniaxial tensile test for fibrous cap, fibrotic media, calcification [242] and lipidic material *a*; adventitia *b* and media-intima *d* layer behavior reconstructed from the material coefficients [247]; nitinol stent material properties *c*.

totally damaged at a value of β_i being 2.5 times the strain energy value associated with SP, which according to our simulation was leading to stresses close to rupture (around 600 KPa for the healthy vessel components, taken as reference) reported in experimental works [242]. The values of τ_i were assumed to be all equal to 0.9 as in [224]. Parameters are summarized in Table 4.1.

4.2.2 Stent model

4.2.2.1 Mesh generation

The stent model was built starting from a μCT scan of an 8x20 mm Acculink stent (Abbott Vascular, Boston, IL). 3DSlicer (`http://www.slicer.org/`) was used to perform accurate geometrical measurements of the stent and to generate a detailed triangulated stent geometry (Figure 4.4a). The geometry was then imported in pyFormex, virtually unrolled using a cylindrical coordinate transformation to obtain the planar device pattern. The repetitive units of the stent were then drawn by "tracing" the flattened geometry (Figure 4.4b). Hexahedral meshes for

Table 4.1: Summary of the material properties and damage parameters for the vessel domain.

Model	Material parameters					Source	Damage parameters			
	C_{10} (kPa)	k_1 (kPa)	k_2	ρ	Fibers angles (°)		Ψ_{mat}^{ini}	Ψ_{fib}^{ini}	τ_{mat}	τ_{fib}
Adventitia	29.8	180.9	109.8	0.8	30.1	Sommer et al., 2012 [247]	3.58	5.0	2.98	4.17
Media-intima	61.15	24.7	16.5	0.8	6.9	Sommer et al., 2012 [247]	7.0	6.0	5.84	5.0
Fibrotic media	21.53	919.8	1919.6	1.0	23.59	Holzapfel et al., 2004 [242]	5.1	1.7	4.25	1.4Z
Fibrous cap	13.98	40.08	65.35	0.75	77.55	Holzapfel et al., 2004 [242]	5.0	5.6	4.17	4.67
Lipid	0.5	–	–	–	–	–	–	–	–	–
Calcification	2250	–	–	–	–	–	–	–	–	–

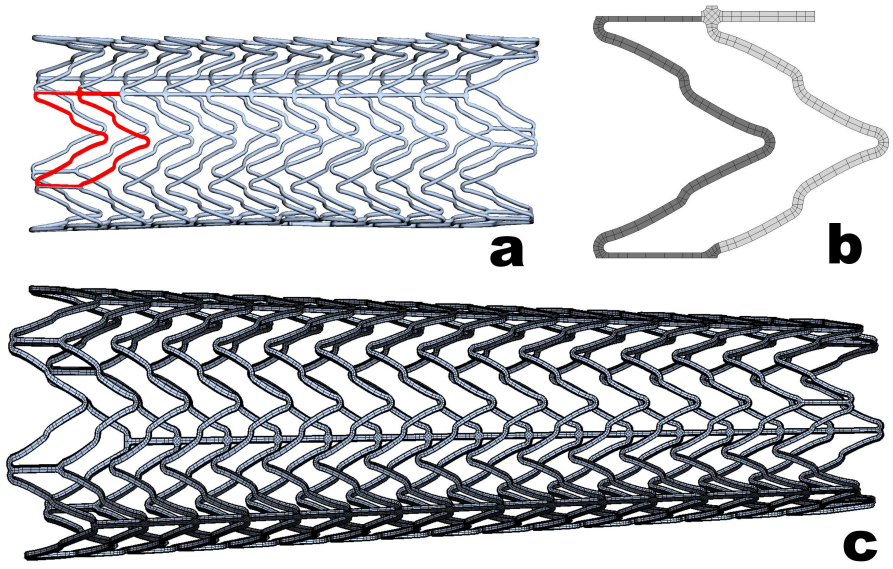

FIGURE 4.4: Mesh generation procedure of the tapered Acculink stent model (7x10x30 mm). Segmented geometry from the μCT scans *a* , creation of the of the parametrized repetitive unit cell *b*, generation of the hexahedral stent mesh *c*.

the SFEA were obtained using the approach described in [250]. The parametric model was adapted to create a 7x10x30 mm tapered stent (Figure 4.4c) to respect the indication of the stent manufacturer for the target vessel. Stent strut thickness and width of the implanted stent were assumed equal to the available sample (0.17 mm and 0.12 mm).

4.2.2.2 Material Model

In order to mimic the behaviour of the self expandable nitinol Acculink stent, the stress–strain relationship of the nitinol alloy (Ti–55.8wt%Ni) was retrieved from literature [251] and defined using an embedded user subroutine in ABAQUS based on the model of [252] (Figure 4.3c). Symmetry in compression was assumed.

4.2.3 Virtual stent deplyment procedure

The commercial finite element solver ABAQUS/Explicit (Simulia Corp, Providence, RI) was used to perform a quasi static analysis of the virtual CAS because of the non-linearity of the material model, large deformations, and complex contact problems. Five simulations were performed

inserting the stent in the different atherosclerotic models. We considered the three previously described models and the baseline was modified to substitute the lipid core with fibrotic material and calcifications (Table 4.2). The nodes of the open branches of the carotid model were constrained to allow only radial displacement. No vascular pre-stretch was considered. The stent placement was performed in five major steps: catheter driven stent crimping and bending along the vessel centerline, balloon dilation at the stenotic location, balloon release, stent deployment by gradually expanding the catheter in the radial direction. Both the catheter and the balloon were modeled as rigid cylinders and their displacements were imposed analytically using a dedicated ABAQUS subroutine (VDISP). A detailed description of the strategy is presented in [250] and outlined in chapter 3. To reduce the potential damage of the vessel, the balloon size was chosen such that it matches the pre-lesion vessel diameter at the stenotic location (5 mm). This conforms with stent manufacturer guidelines. Reduced integration elements with hourglass enhancement were chosen for both stent and vascular domain while for the rigid tubular structures quadrilateral surface elements with reduced integration were used.

4.2.4 Data analysis

In order to evaluate the impact of the virtual procedure the following data were analyzed:

1. The 99 percentile of the maximum principal Cauchy stresses (99PCS) of the different vascular regions to study possible zones of plaque rupture and tissue failure.

2. The volume of damaged arterial tissue (using the material model damage criteria) beyond 50% (VD50%) at the stented location,

Table 4.2: Description of the carotid artery models considering different lumen shapes and plaque components.

Model	Lumen shape	Fibrous cap thickness (mm)	Lipid core material
Baseline	circular	0.25	lipid
CIRC/025/FIB	circular	0.25	fibrotic media
CIRC/025/CALC	circular	0.25	calcification
CIRC/050/LIP	circular	0.5	lipid
ELL/025/LIP	elliptic	0.25	lipid

which could initiate the restenotic process. The volumes of damaged extracellular matrix and collagen fibers are considered separately.

3. The relative lumen gain at the maximum stenosed location (the ratio between the area increase and the initial stenotic area) to indicate poor early outcomes of CAS which can contribute to restenosis.

4.3 Results

4.3.1 Stress analysis

Figure 4.5 shows the results of the virtual stent deployments. The open cell design of the Acculink stent adapts well to the tortuous stenotic location with only limited gaps and, consequently, good scaffolding of the plaque. The stress distribution contour plot is thresholded at 250 kPa, the experimentally determined stress at rupture for fibrous cap in severely stenosed iliac arteries [242]. The geometries with lipid core

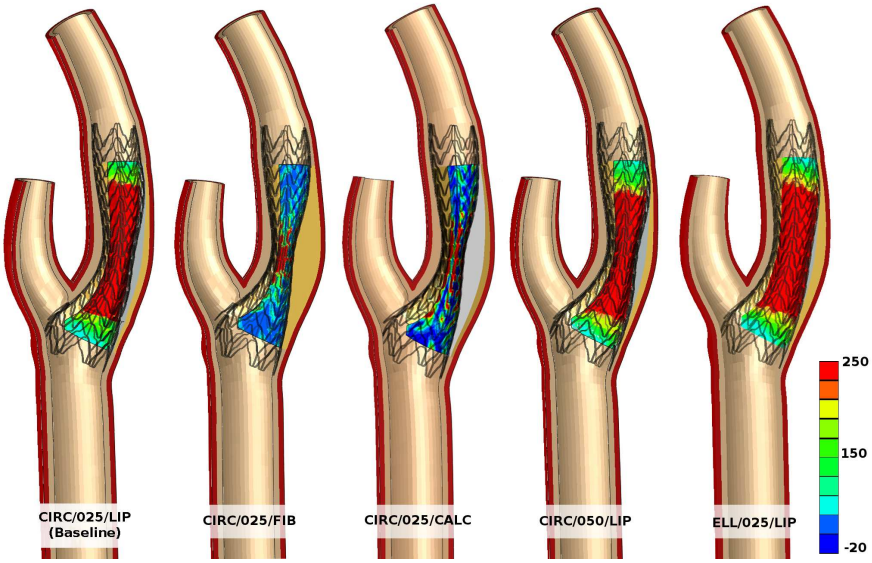

Figure 4.5: Deployed configuration after performing the virtual procedure. Maximum principal Cauchy stresses (kPa) are depicted for the fibrous cap. Positive values are thresholded at 250 kPa, the chosen fibrous cap rupture limit according to experimental data ([242]).

(CIRC/025/LIP, CIRC/050/LIP, ELL/025/LIP), show a larger area with higher stresses than the cases in which the lipid pool has been substituted with calcified and fibrotic tissue (CIRC/025/FIB and CIRC/025/CALC).

No substantial differences are observed between these two stenosis with stiffer materials, while an increased fibrous cap thickness (CIRC/050/LIP) reduces the area of the maximum stresses.

A detail of the Cauchy stresses at the maximum stenosed location after stenting is depicted in Figure 4.6. Stiffer plaques (CIRC/025/FIB and CIRC/025/CALC) induce a larger area of stress concentration around the vessel lumen. In particular, the calcification seems to create a zone of compressive stress at the fibrous cap / calcification interface and a better shielding of the underlying tissues. The models with large lipid core (CIRC/050/LIP, ELL/025/LIP) show a similar stress distribution with compression of the fatty plaque, high tensile stresses concentrated in the fibrous cap and a smaller area of stress concentration around the lumen region opposite to the plaque.

The thicker fibrous cap slightly reduces the stresses induced into the lipid pool (CIRC/050/LIP), while the elliptic shape (ELL/025/LIP) has the opposite effect. The elliptic lumen also causes an increase of stresses at the opposite side of the plaque. This might be explained by the larger post-stented area and smaller initial thickness of the healthy region.

Table 4.3 lists the volumes of the damaged artery, 99PCS in each region and the lumen gain at the highest stenotic location. Due to the symmetry of the model, the damage of the fibers in every element is very close, so the maximum values of fiber-contributed damaged volumes is considered. The results can be interpreted considering the differences between soft (lipidic) vs hard (fibrotic and calcified) plaques. While the 99PCS of the adventitia and the fibrous media is comparable in all models, in case of hard plaques the values of stress in the media are much higher, while in the fibrous cap stresses are significantly smaller. The softer mechanical behavior of fatty plaques allows larger deformation of the fibrous cap, leading to higher stress values. This is in line with previous computational studies [253]. The lipid pool shows lower 99PCS in the modified geometries. In particular, lower stresses are found in the model CIRC/050/LIP, demonstrating the shielding effect of a thicker fibrous cap.

However, as shown in Figure 4.6 at the largest stenosed location, higher compressive stresses were found in the model ELL/025/LIP. Combined with stresses close to rupture in the fibrous cap, this might increase the risk of plaque material leaking into blood circulation and suggests

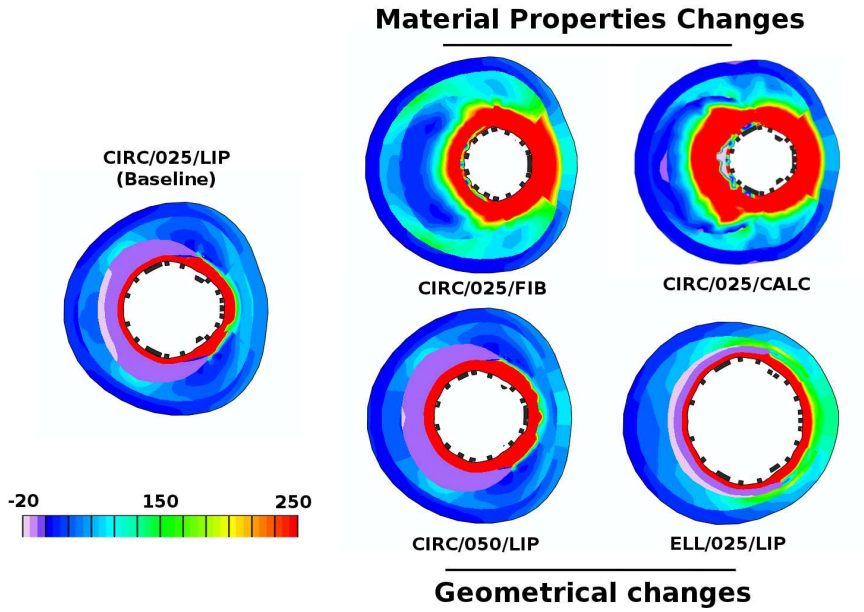

FIGURE 4.6: Maximum principal Cauchy stresses (kPa) at the maximum stenotic location after stenting. Positive values are thresholded at 250 kPa, the chosen fibrous cap rupture limit according to experimental data ([242]).

that global indicators can mask zones of localized risk, as previously reported [154].

4.3.2 Damaged volume

The VD50% of the extracellular matrix in the adventitia is almost zero in all models, while the damage of the fibers is considerable only for hard plaques, suggesting that soft plaques can protect a larger area of the underlying tissue but can induce higher stresses in localized regions. The healthy media shows an overall lower damage for soft plaques. Contrarily, the VD50% of the fibers of the fibrous cap is generally lower in hard plaques while it shows no changes among the fatty core models. This is in agreement with the stress distribution in Figure 7.

4.3.3 Lumen gain

Stiffer material properties of the plaque, in similar procedural conditions result in a smaller increase of the narrowed lumen, i.e. higher residual stenosis, and may potentially lead to the restenotic process. A thicker fibrous cap on the one hand is able to shield the lipid pool but results

Table 4.3: Summary of the carotid artery model's results considering different lumen shape and plaque components.

	Damage										Cauchy stress					Lumen gain
	Volume of damaged matrix (%)					Volume of damaged matrix (%)					99 Percentile (kPa)					(%)
Model	**ADV**	**MED**	**FC**	**LIP**	**FM**	**ADV**	**MED**	**FC**	**LIP**	**FM**	**ADV**	**MED**	**FC**	**LIP**	**FM**	
Baseline	0.0	13.0	3.0	–	9.0	0.0	7.1	70.0	–	6.0	99	243	1423	10	553	60
CIRC/025/FIB	0.0	24.6	7.0	–	56.0	25.0	16.7	40.0	–	58.0	105	405	633	414	544	30
CIRC/025/CALC	0.0	18.0	12.0	–	27.0	10.8	15.0	34.0	–	43.0	101	421	612	792	517	30
CIRC/050/LIP	0.0	13.8	3.0	–	9.0	0.0	7.0	69.0	–	6.0	100	260	1088	0	509	50
ELL/025/LIP	0.0	5.0	0.0	–	4.0	0.0	3.6	61.0	–	3.0	112	258	1217	2	441	70

in smaller lumen gain. The elliptic model shows the best result with the lowest residual stenosis.

4.4 Discussion

In this work we studied the effects of different plaque constitutions and lumen shapes on CAS. In general, the procedure leads to a good clinical outcome, but peri- and post-procedural complications still occur, such as embolization and restenosis.

Higher residual stenosis in case of hard plaques compared to soft plaque has previously been reported for coronary artery stenting [254–256] supporting the results obtained in this work. This is consistent with the biomechanical properties of soft plaques that, because of the low elastic modulus, experience higher strains [148,253,257].

The higher stresses in the fibrous cap region of soft plaques demonstrate their vulnerability to potential plaque fragmentation and embolization, as shown by clinical evidence [239,240].

It has also been reported that eccentricity of the plaque results in higher lumen gain and a larger amount of plaque reduction [255,258]. This can partially explain the higher lumen gain of the elliptic shaped model (more eccentric than the circular lumen geometry) and the higher compressive stresses at the maximum stenotic location. Additionally, our results show that an elliptical lumen with a soft plaque allows for a higher lumen gain due to the larger surface interacting with the lipid pool.

Soft plaques have shown to give better post-procedural results, yet they are also more prone to restenosis [256]. In the present work, the models with lipid core have a larger area of the fibrous cap with high stresses. This can comply with the higher risk of restenosis, which occurs as a vascular response to injury [259,260].

Animal studies have demonstrated that stent configuration is related to vascular injury, thrombosis and neointimal hyperplasia [260,261] and numerical studies have indicated that the stent mesh influences differences in stress distribution in the vascular wall [168,262,263] which seems to explain why stent design has been reported to affect restenosis [264].

Note, however, that in these aforementioned computational studies, the results were obtained on a single vascular geometry while our results suggest that the same stent inserted in similar procedural conditions is influenced by the vascular morphology and plaque constituents. This is

similar to what has been reported after virtual procedures on concentric atherosclerotic coronary arteries with different plaque composition [241].

In addition, our study shows that eccentricity leads to an uneven stress distribution in the vessel, with high stresses in the regions not masked by the plaque. This seems to provide a biomechanical basis to the evidence that eccentric plaques are more prone to procedural failure [265, 266]. Lumen shape, by affecting stress distribution, is known to have an impact on plaque fracture location [144]. This may be relevant for calcified plaques with low fracture stresses, that have a high risk of thrombosis, though become more vulnerable after endoluminal treatment [241].

Our approach allows to study the peri-operative CAS environment from a structural point of view only, thus neglecting the effect of stent placement on flow changes. The stent struts may induce clot formation [267, 268] and, as in our cases, the flow to the external carotid artery may be obstructed. Computational fluid dynamic results compared with experimental data have shown that shear stresses induced by local flow patterns due to the stent struts, promote neointimal proliferation [108,269] suggesting that the vascular characteristics, which drive the deployed stent configuration, can also affect restenosis via pathways related to the blood flow.

According to our results, the plaque shoulder regions, that exhibit stress concentrations induced by the *in vivo* loading conditions in unstented lesions [145,151], seem not to have an impact on the stress distribution due to the stent placement. This is particularly visible comparing the elliptical with the baseline model.

Even though the computational complexity of the presented models is high, there are some limitations which might influence the interpretation of the achieved results. The virtual insertion was performed by bending the stent along the vessel centerline, without simulating the advancement of the stent through the vascular network. Though due to the superelastic behaviour of nitinol (with no plastic deformation at working conditions), the mechanical history of the device should not substantially affect the final stent configuration. The stent placement was simulated by gradually opening the cylindrical catheter in the radial direction without considering the catheter retraction which may slightly affect stent positioning in real cases. Thus an ideal stent positioning was simulated, excluding operator dependency. The balloon expansion was modeled as a rigid surface displacement, regardless of a possible non uniform expansion of the angioplasty balloon [103, 179].

Experimental data on human arteries are needed to correctly evaluate the injury of the plaque and the vascular wall. The models also neglect the *in vivo* pre-stretch condition which can cause an underestimation of the numerical stress results [112]. The hard plaque morphologies have a very high recoil. For these stiff materials, a hyperelastic formulation with or without a damage model may not be adequate to describe the endovascular procedure, and permanent deformations of the vascular components should be included to obtain more realistic results [111]. Given, however, the comparative nature of this study, we believe that these simplifications and limitations are acceptable.

CHAPTER 5

Feasibility of a priori numerical assessment of plaque scaffolding after carotid artery stenting in clinical routine

The previously described virtual carotid stenting environment is now pushed forward to analyze patient specific geometries from clinical data. The real procedure is emulated in the numerical setting and the resulting outcome is validated with the post-operative datasets. Additionally relevant geometrical parameters have been computed on the deployed device to evaluate the quality of the procedure by analyzing potential causes of procedural failure. The results of this study have been resumed in a manuscript submitted to:
"Feasibility of a priori numerical assessment of plaque scaffolding after carotid artery stenting in clinical routine: proof-of-concept", Iannaccone, F., S. De Bock, M. De Beule, F. Vermassen, I. Van Herzeele, P. Verdonck, P. Segers, and B. Verhegghe. *International Journal of Artificial Organs*.

5.1 Introduction

Carotid artery stenting (CAS) is an alternative procedure for treatment of severely stenosed symptomatic (stenosis>=50%) or asymptomatic

carotid (stenosis>=60%) artery lesions in high-risk patients and is associated with a similar stroke, death and myocardial infarction rate, compared with carotid endarterectomy (CEA) [37, 270]. Younger patients (<69 years of age) have been shown to have lower event rates with CAS compared with CEA in 2 large randomized trials [271]. While the physician's and center experience in this technique is growing, the peri-operative risks of the procedure are decreasing [166,271–273]shifting the major events to post-procedural complications [272] in well-selected patients. It has been suggested that stroke after CAS may be caused by embolization when the stent mesh is unable to adequately confine and scaffold the plaque[166]. In 75% of all procedures, all type of stents are likely to obtain similar results. However, the rest of the procedures need accurate screening. In these cases carotid stent choice is influenced by arterial anatomy and lesion morphology [274–276] as scaffolding of the plaque by the stent is one of the key parameters for procedural success.

One of the requirements for carotid stent design is good apposition of the stent to the vessel wall [169,277] as clot formation on the metallic stent surface is accelerated by the decreased blood flow velocity at the stenotic lesion by stent placement [267,268]. While the effect of incomplete stent apposition (ISA) has been studied in coronary arteries and appears to be a factor potentially contributing to late stent thrombosis [278], limited data is present in literature about consequences of ISA on the clinical outcome of carotid stenting. Even though one study showed that ISA is not related to adverse clinical events [268], the associated risk of restenosis is yet to be clarified. This post-procedural risk is, at present, not trivial to assess by imaging. Mono and biplane angiography, currently the gold standard to assess CAS [34], is not an optimal technique for the detection of stent malapposition. Other techniques such as OCT [279] or IVUS [67] have been proven to be safe and effective in quantifying stent malapposition and plaque prolapse (associated with major adverse events) but they are not commonly used in CAS.

Whether stent design influences the peri-procedural and early post-procedural neurologic outcome is also still an unsolved topic, mostly due to the lack of data relating stent designs to the clinical outcome [166, 280–283]. When re-analyzing the SPACE trial data, Jansen et al. [280] showed a statistically significant difference between open and closed stent designs, demonstrating a lower rate of events associated with closed cell design in these symptomatic patients, which is known to be associated with an increased risk for peri-operative stroke [42]. A retrospective analysis of patients treated with various carotid stents in symptomatic

and asymptomatic carotid artery disease noted increased post-procedural event rates for the 4 open cell stents and for one of the 3 closed cell stents used in the different considered studies [166]. When the stents were sub-grouped according to the free cell area (FCA) higher post-procedural event rates were correlated with an increase of FCA. The differences were more pronounced in symptomatic patients confirming findings of previous works [284]. However, criticism has been raised due to possible biases and confounders [285–287] in particular because no objective measurement of silent brain infarction such as diffusion-weighted magnetic resonance imaging (DW-MRI) was performed. In contrast, others have failed to prove any difference in stroke and death risk between patients treated with open / closed stent designs or grouped by FCA [281, 286, 287]. Still, uncertanty remains especially since the occurrence of any stroke is unclear [288,289] and may have an impact on the interpretation of the results [286]. Moreover, open cell stent design has also been associated with fewer new DW-MRI lesions [287], although in this study in contrast to others [283], no embolic protection device was used. More recently a meta-analysis of Tadros et al. [290] noted that symptomatic patients with favorable anatomy treated with a closed cell design, have fewer major adverse events, reopening the debate.

Geometrical features of the device may definitely play a role in CAS outcomes and newer devices are focusing on the improvement of the scaffolding capabilities [289], which includes membrane stent systems such as MembraX (Abbott Vascular, Behringen, Switzerland). Geometrical scaffolding parameters have been previously proposed on the free expanded configuration [169], although the same device can have a different behavior in situ depending on the anatomical site [274–276].

Technical tools that are able to predict stent appositioning and its mechanical behavior in the treated vessel are appealing, and may be beneficial for procedure planning. Numerical studies are helpful in the process of virtual carotid stent design and optimization and have demonstrated to be a valid predictive tool when tested *in vitro* [170], and useful to study the behavior of different stent designs implanted in a single carotid model [110,167,168,172]. Although, to the authors knowledge, no CAS *in vivo* validation has been previously reported. The present work introduces a novel virtual patient-specific pre-operative environment to evaluate the feasibility of numerical prediction of clinical outcomes after CAS focusing on plaque scaffolding. Mechanical simulations have been coupled with novel analysis tools to quantify scaffolding parameters in situ. Two real patient cases treated with the Acculink stent (Abbott

Vascular, North Chicago, IL) were studied to proof the concept. Routine pre- and post-stenting imaging were compared with the computer simulations to validate the virtual operative procedure.

5.2 Materials and methods

5.2.1 Patient data

Two patient datasets (obtained after informed patient consent for the use of their data in this work) were available for the study referred as patient A (male, 75 years, 75% degree of stenosis in the internal carotid artery - ICA) and patient B (female, 61 years, 85% degree of stenosis in the ICA). Both asymptomatic patients were treated via the trans femoral route using an embolic protection device (Emboshield NAV 6, Vascular, North Chicago,IL) and an Acculink stent was implanted by an experienced team: tapered 7 mm x 10 mm x 40 mm for patient A and tapered 7 mm x 10 mm x 30 mm for patient B. Pre-operative Computer Tomography Angiography (CTA) images were acquired with a Siemens Somatom Sensation Cardiac scanner with resolution of 0.37 mm x 0.37 mm x 1 mm for patient A and Siemens Somatom Definition Flash scanner with resolution of 0.54 mm x 0.54 mm x 3 mm for patient B. Post operative monoplane angiography were acquired using a Philips AlluraXPer FD10.

5.2.2 Vessels models

From the pre-operative 3D CTA, geometries of the vessel lumen and of the calcified plaques were segmented (Figure 5.1A) using 3DSlicer (`http://www.slicer.org/`). Other tissues (such as soft plaques and vessel wall) were not visible on CTA. To create an approximate model of the vessel wall the following steps were taken:

1. the geometry of the calcified plaque and the vessel lumen were combined and manually corrected to create an approximated shape of the assumed healthy lumen before lesion development (Figure 5.1B);

2. the actual lumen and calcified plaque were subtracted from the geometry of the healthy lumen in order to obtain the non calcified plaque geometries (Figure 5.1B);

3. subsequently, the 3D triangulated models were generated for the diseased lumen, the plaques components and the healthy lumen;

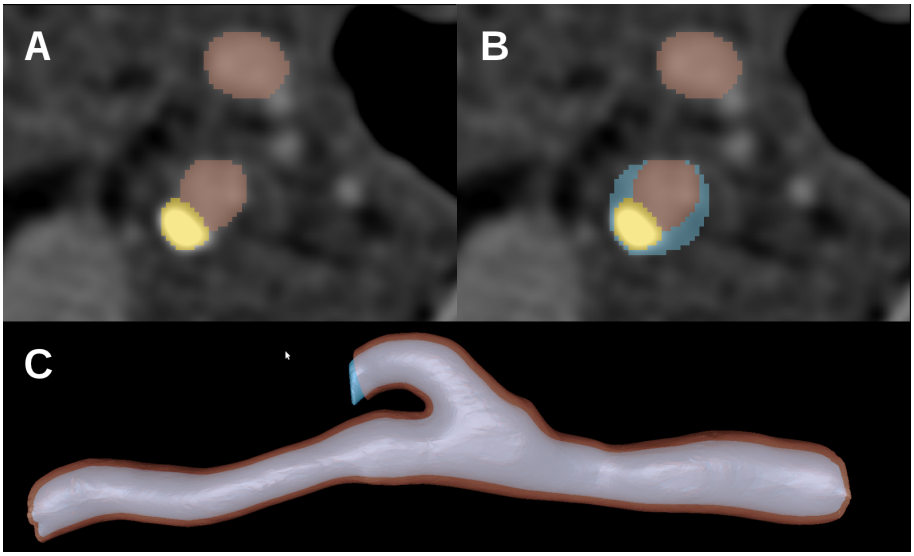

FIGURE 5.1: Work-flow of the vessel model reconstruction: *A* segmentation of the vessel lumen and calcified plaque, *B* manual adjustment of the lumen shape to create the assumed healthy lumen and retrieve the subtracted non calcified lesion depicted in blue , *C* expansion of the healthy lumen to create the outer vessel wall.

4. the healthy lumen geometry was expanded to create the outer vessel wall geometry. The healthy lumen distance to the centerline of the vessel (computed in vmtk `http://www.vmtk.org/` was increased by 30% in the normal direction to the surface, a realistic value of the carotid artery wall thickness [112].

5. Starting from the geometry of the real lumen and the reconstructed outer wall, the 3D hexahedral mesh of the vessel (Figure 5.2) for the numerical solver is created using IA-FEmesh, a meshing tool embedded in 3DSlicer [291], as described in chapter 3.

The vessel was considered as single-layered. We used a stress-strain curve for the arterial wall published in a previous study [98]. We then scaled the curve to calibrate the actual deformations induced by the stent (using the pre- and post operative imaging data) , and coefficients of several hyperelastic constitutive models were fitted to the material response curve using the tool "Evaluate" of the ABAQUS (Simulia Corp, Providence, RI) material property menu. Mainly due to stability concerns, we opted for a third order Ogden hyperelastic material model formulation, whose general strain energy potential Ψ is given by:

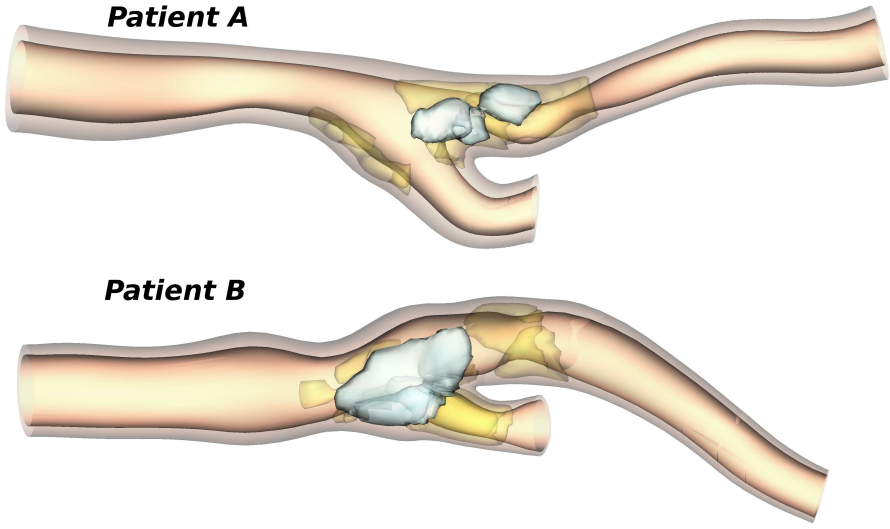

Figure 5.2: Reconstructed vessel geometries of the 2 patients. Calcifications are depicted in white and the assumed hypocellular plaque in yellow.

$$\Psi = \sum_{i=1}^{N} 2\frac{\mu_i}{\alpha_i^2}(\overline{\lambda_1}^{\alpha_i} + \overline{\lambda_2}^{\alpha_i} + \overline{\lambda_3}^{\alpha_i} - 3) \tag{5.1}$$

where $\overline{\lambda_1}$ are the deviatoric principal stretches ; N is a material parameter; and α_i, μ_i are temperature-dependent material parameters.

In order to assign different material properties at the plaque location, the segmented geometries of the plaques were used to select the elements of the vessel mesh located inside the plaques surfaces. The material properties of the plaques were derived from Loree et al. [113] and fitted using a first order hyperlastic Ogden model using the afore mentioned ABAQUS tool. To roughly emulate the rupture of the plaque we assumed a constant plastic behavior at the reported values of plaque rupture (400 kPa). All material parameters are summarized in Table 5.1, 5.2 and 5.3 .

5.2.3 Stent models

The stent models were built starting from a micro-CT scan of a 8 mm x 20 mm Acculink straight design to retrieve the basic cell geometry of the implanted stents. After segmentation of the stent geometry (in 3DSlicer), a parametric hexahedral stent model was built in pyFormex

TABLE 5.1: Material parameters for the calibrated vessel wall.

	III order Ogden parameters					
	$\mu_1(kPa)$	α_1	$\mu_2(kPa)$	α_2	$\mu_3(kPa)$	α_3
Calibrated healthy wall	-3820	0.94	3490	2.75	620	-11.43

TABLE 5.2: Material parameters for the the fitted plaques components. Data are retrieved from [113].

	I order Ogden parameters		
	$\mu(kPa)$	α	Plasticity (kPa)
Hypocellular plaque	21.8	24.72	400
Calcified plaque	72.34	25	400

TABLE 5.3: Nitinol material parameters for the stent devices. Symmetry in compression was assumed.

Variable	**Value**
Austenite elasticity (MPa)	41000
Austenite Poisson ratio	0.3
Martensite elasticity (MPa)	23333
Martensite Poisson ratio	0.3
Transformation strain	0.0437
Start of transformation loading (MPa)	450
End of transformation loading (MPa)	520
Reference temperature (°C)	37
Start of transformation unloading (MPa)	210
End of transformation unloading (MPa)	130
Start of transformation stress in compression (MPa)	450

(`http://www.pyFormex.org`) using the approach described in De Bock et al. [250]. The parametric model was adapted to create the tapered stents (7 mm x 10 mm x 30 mm and 7 mm x 10 mm x 40 mm) shown in Figure 5.3.

Stent strut thickness and width were assumed equal to the ones of the available sample, measured in 3DSlicer (0.17 mm and 0.12 mm respectively). The stress–strain relationship of the nitinol alloy (Ti–55.8 wt% Ni) was retrieved from literature [251] and defined using an embedded user subroutine in Abaqus based on the model of Auricchio et al. [252]. Symmetry in compression was assumed (Table 5.3).

5.2.4 Virtual stent deployment procedure

The commercial finite element solver ABAQUS/Explicit with quasi static analysis was used to mimic the real stent implantation. The numerical simulation involved non-linearity due to the material properties, large deformations, and complex contact problems. The general contact algorithm was used to handle the interactions assuming a friction value of 0.05 for all the contact surfaces [167]. The stent placement was emulated imposing analytical displacements to a cylindrical catheter (4-node surface elements with reduced integration - SFM3D4R) by a VDISP subroutine to drive crimping, smooth bending along the centerline of the

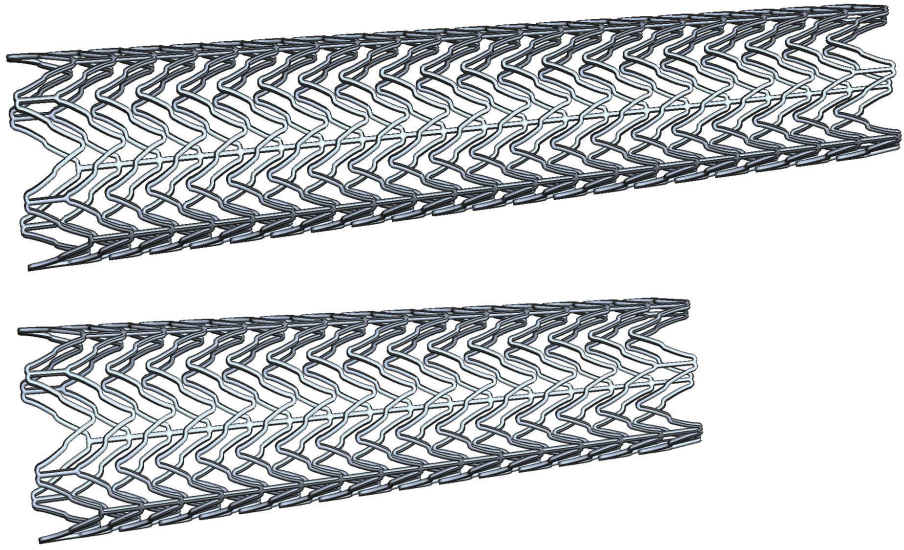

Figure 5.3: Schematic description of the evaluated scaffolding parameters.

vessel and deployment of the stent at the arterial lesion as previously described [250]. A similar cylindrical geometry was used to emulate balloon pre-dilation of the vessel up to the assumed diameter of the normal vessel.

5.2.5 Validation

To validate the numerical results we compared the post-procedural monoplane angiographic images and the virtual implantation qualitatively showing the stent struts shape. A quantitative validation was performed measuring the relative errors ε between the diameters D of the stented location with respect to the clinical data measured as:

$$\varepsilon = \frac{D_{simulation} - D_{in\,vivo}}{D_{in\,vivo}} \cdot 100 \tag{5.2}$$

The monoplane angiograms were previously calibrated from the catheter size used during CAS. The numerical results were imported in pyFormex to extract the vessel lumen and the angle of view of the deformed model was manually adjusted in the viewer to match the position of the *in vivo* dataset. *In vivo* and simulated implantation images were calibrated to match the diameter of the non-stented vessel portions.

5.2.6 Post-processing for scaffolding evaluation

Three different parameters were measured to evaluate the scaffolding of the stent, i.e. the support given by the stent to the arterial lesion, schematically depicted in Figure 5.4:

1. Incomplete strut apposition (ISA) to the vessel wall, computed as the distance from the external stent surface nodes to the closest vessel surface element. The percentage area of stent struts within a threshold distance of the vessel wall, relative to the total stent area was computed as quantitative parameter of ISA. The threshold of 0.2 mm was chosen to identify most critical areas undergoing ISA [279].

2. Stent cells areas of the implanted stent. The cell area was computed from the minimal surfaces that could fill the FCAs. The surface was created on the undeformed stent, triangulating the cell nodes and keeping trace of the connectivity of each triangle. Using the connectivity table, the surface was then deformed according to the new position of the cell nodes after the implant.

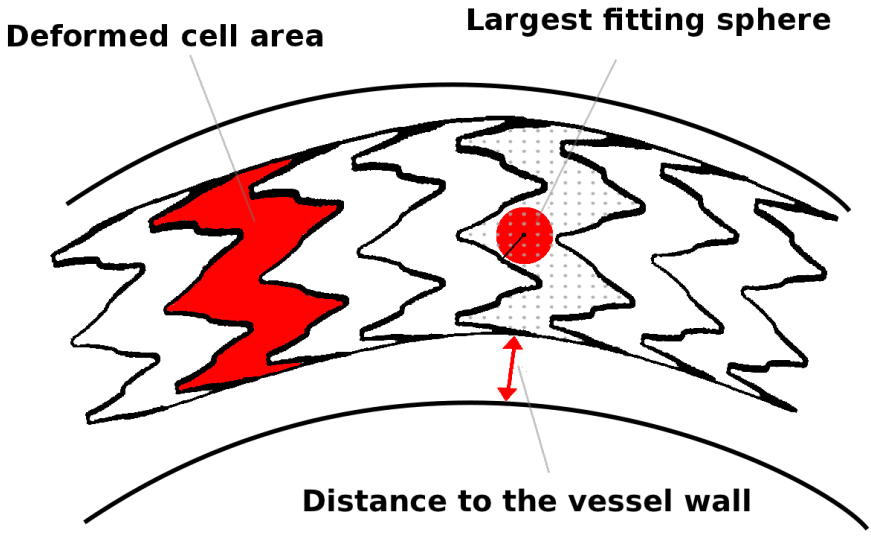

Figure 5.4: Implanted tapered Acculink stent models (7 mm x 10mm x 40 mm and 7mm x 10 mm x 30 mm).

3. Largest fitting sphere (LFS) going through the FCAs. The surface fitting the FCA has been seeded with an adequate number of points (determined after convergence estimation). The minimum distance of each point to the free edges of the cell is computed. The point (center of the sphere) with the largest distance (radius of the sphere) is then selected.

5.3 Results and Discussion

5.3.1 Validation

The numerical simulations were able to emulate the overall shape of the implanted stents retrieved from the clinical monoplane angiographic images (Figure 5.5 and 5.6).

Table 5.4 summarizes the relative error of the lumen diameter for the indicated sections. Mean relative errors of the lumen diameters are 5.31±8.05% for patient A and 4.12±9.84% for patient B.

Both the qualitative and quantitative comparison between post-procedural angiography and the projected image of the virtually implanted stent show an overall good agreement, catching the main features of the deformed stent shape. In particular patient A showed a better match of

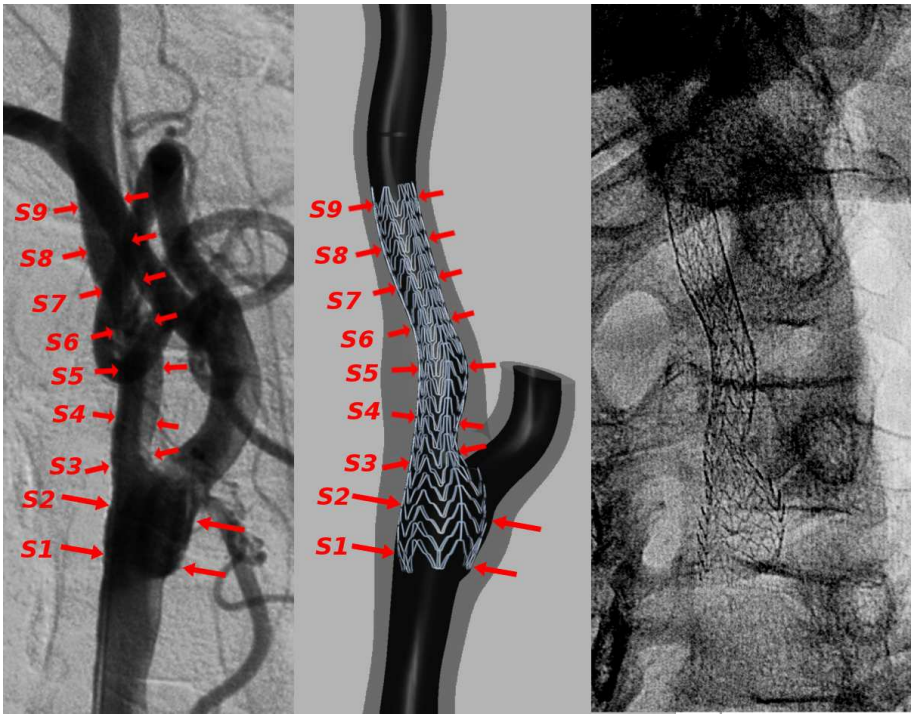

FIGURE 5.5: Qualitative comparison of the implanted stent configuration for patient A showing the clinical and numerical results. From left to right: angiography of stented lumen, numerical results and X-ray of the implanted stent. Red arrows indicate the location of the measured diameters.

TABLE 5.4: Absolute values of the diameters of the stented vessel and the relative error between the numerical simulation and the clinical data, computed at 9 different sections. .

	Diameters	**Section**									**average**
		S1	**S2**	**S3**	**S4**	**S5**	**S6**	**S7**	**S8**	**S9**	
	Numerical (mm)	7.38	8.59	4.82	4.20	4.59	3.71	4.14	4.42	4.30	
Patient A	Clinical (mm)	7.44	8.12	3.99	3.78	4.17	3.94	3.94	4.30	4.37	
	ε%	-0.85	5.82	21.06	11.01	10.15	-5.73	5.20	2.79	-1.61	5.31±8.05
	Numerical (mm)	6.45	6.18	6.54	5.89	5.30	4.96	5.21	5.96	5.37	
Patient B	Clinical (mm)	6.45	5.71	5.80	5.97	6.37	5.62	5.63	6.29	5.76	
	ε%	0.00	-7.62	-11.25	1.26	20.28	13.33	8.10	5.55	7.40	4.12± 9.84

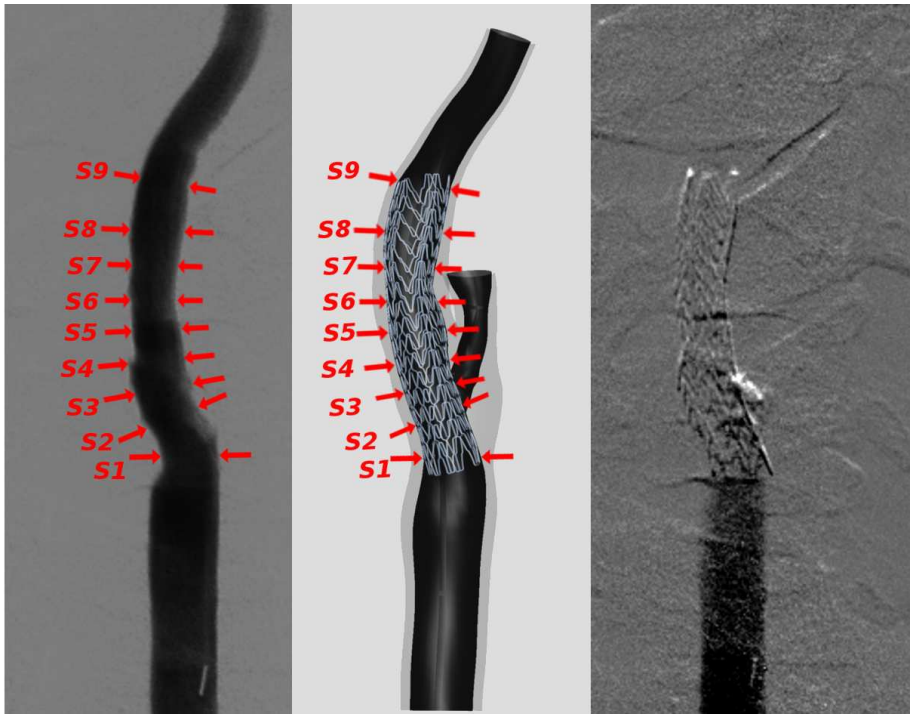

Figure 5.6: Qualitative comparison of the implanted stent configuration for patient B showing the clinical and numerical results. From left to right: angiography of stented lumen, numerical results, and X-ray of the implanted stent. Red arrows indicate the location of the measured diameters.

the stent shape compared to patient B even though average diameters errors are similar in both cases.

5.3.2 Scaffolding

Results of the scaffolding evaluation are summarized in Table 5.5 and Figures 5.7, 5.8 and 5.9.

As can be observed in Figure 5.7, the open cell design shows ISA to the vessel wall in the most tortuous and anatomically complex regions.

The percentage of stent struts area with ISA is remarkably higher for the patient A (8.8% vs 2.4%) but results can be misleading due to the fact that patient B has a completely occluded external carotid artery and patient A had a larger part of the stent deployed at the bifurcation region where there is a higher mismatch between stent and vessel diameter, consequently leading to a higher areas of ISA. Both cases show good apposition to the ICA. For patient B the sections at the bifurcation and

TABLE 5.5: Average results of incomplete strut apposition (ISA), free cell areas (FCA) and the radius of the largest fitting spheres (LFS).

Model	Global scaffolding parameters		
	Stent area with ISA (%)	**FCAs (mm^2)**	**Radius of LFSs (mm)**
Patient A	8.8%	7.69±3.05	0.45±0.11
Patient B	2.4%	7.59±2.80	0.46±0.11

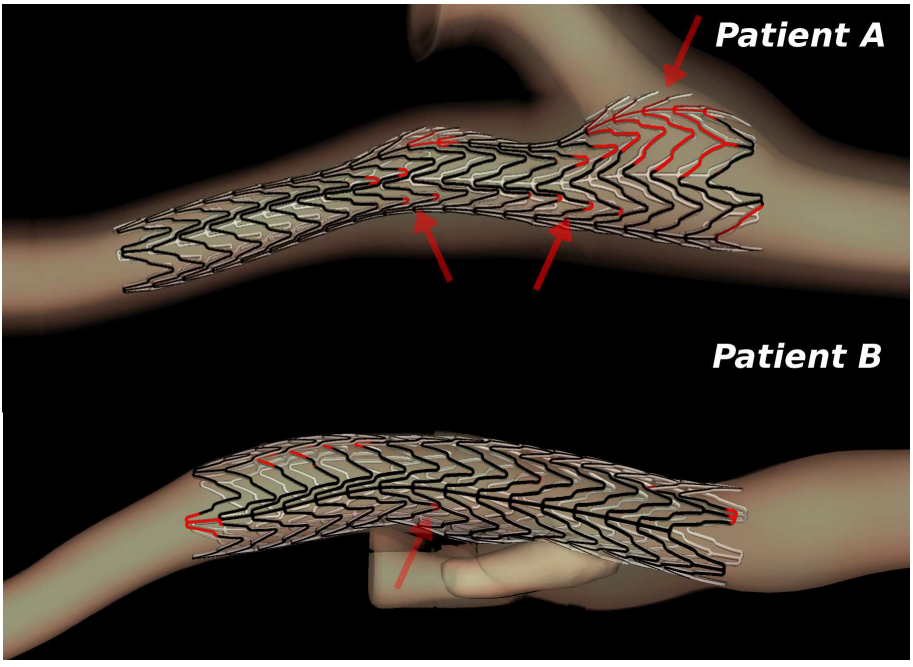

FIGURE 5.7: Incomplete strut apposition (ISA) of the implanted stents (struts colored in red). Threshold was set at 0.2 mm. The arrows indicate the regions where the fish scaling effect occurs.

at the ICA were similar, giving a better apposition to the vessel wall, also due to smaller curvature of the vessel. At the inner curvature of the vessel wall ISA is noted in both cases, showing the "fish scaling" effect typical for open cell design, which is very apparent in patient A at the bifurcation (Figure 5.7). Distal ISA, which has previously been reported [268], occurred in patient B while proximal ISA occurred in both patients. The analysis of the deformed FCAs shows that the target diameter of the vessel highly influences scaffolding provided by the device. In fact, patient A, with a smaller ICA diameter resulted in smaller FCAs compared to patient B with a larger ICA diameter (Figure 5.8). Also, in patient B, the cross sectional change of the vessel following stent deployment is less pronounced, leading to a more uniform cell shape deformation.

Largest fitting spheres (Figure 5.9) do not pace the free cell areas distribution. Maximum values of FCAs do not necessarily correspond to higher values of the LFSs.

For patient B the FCAs are similar at the bifurcation and at the mid part of the stent, while the LFSs are more inhomogeneous, ranging from 0.36 to 0.7 mm. High values of LFSs are found at the ICA, mainly

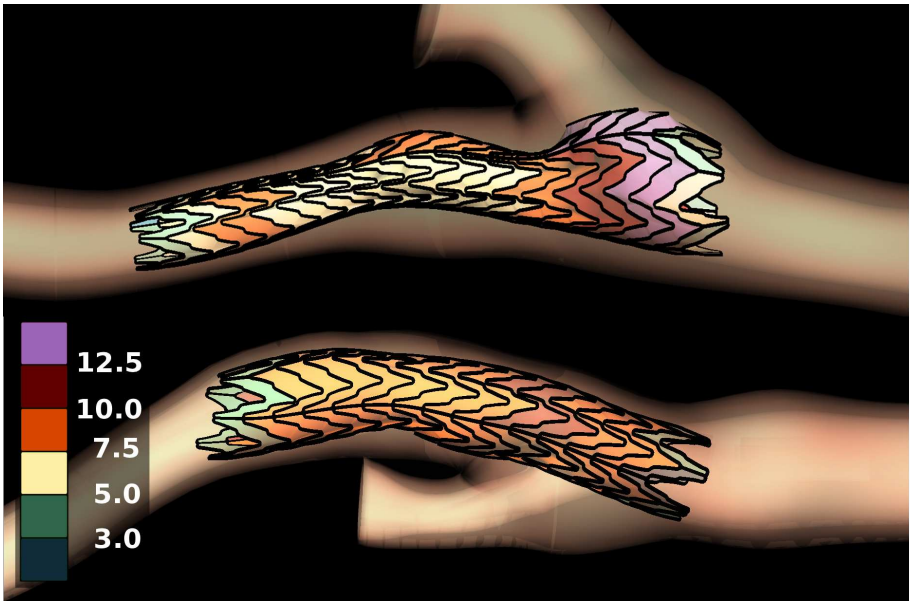

Figure 5.8: Free cell areas (FCAs) of the implanted stents (in mm^2). Top: patient A, bottom: patient B.

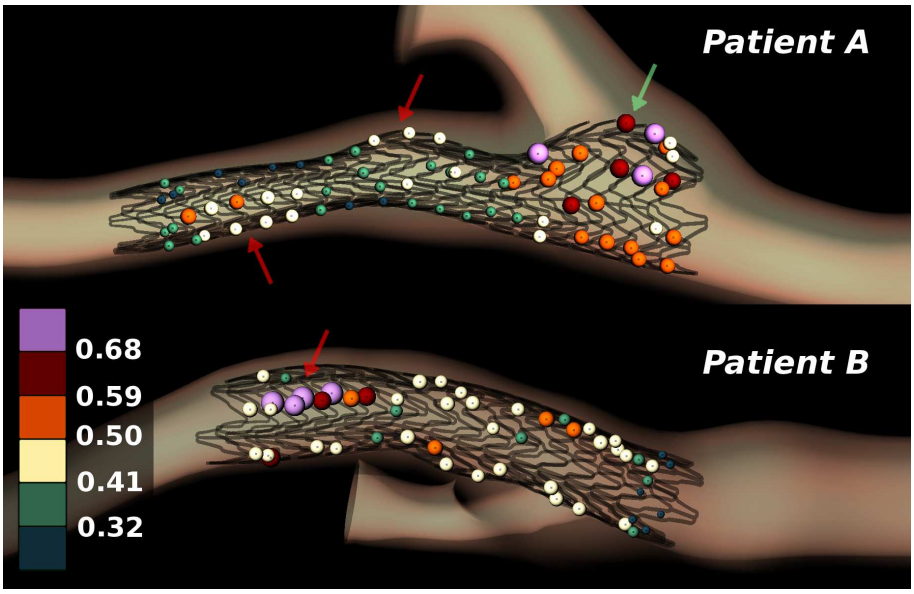

FIGURE 5.9: Radius of the largest fitting spheres (LFSs) of the implanted stents (in mm). Red arrows show the concave regions of the vessel, which are associated with relatively large spheres compared to the convex regions. The green arrow shows how the fish scaling can influence the sphere dimensions.

concerning the cells apposing at the concave region of the vessel. Similar considerations can be made for patient A. The chosen stent, which corresponds to the diameter requirements of the distal ICA, was undersized for the bifurcation diameter resulting in an under-expansion of the stent, leading to a free expanded-like configuration with higher FCAs and also high LFSs. It can be noticed that high values of LFCs are also found at the distal location of the ICA, again at a concave part of the vessel although the FCA is small. This seems reasonable when thinking of a bending bar: at the inner curvature stent struts get closer, while at outer curvatures they widen. The values are also influenced by ISA. In fact, if the cell "opens" in the radial directions, due to fish scaling, this results in higher LFSs compared to a more planar configuration, as indicated by the green arrow in Figure 5.9.

As highlighted in our study the fish-scaling effect (the tendency of the stent struts to protrude into the vessel lumen) is present even with moderate tortuosity at the convex lumen regions, which will clearly be more accentuated with a more complex lumen shape. It has been speculated that fish scaling contributes to restenosis and stent fracture [277]. The

price for the absence of shortening, optimal conformability and flexibility of the open cell design leads to plaque scaffolding with lower plaque coverage, possibly promoting plaque protrusion through the interstices of the stent struts allowing plaque material to embolize after implantation [292]. Nevertheless, in the analyzed patients due to a straight post-stented vessel geometry and adequate sizing, the stent seems to offer a good scaffolding of the lesion.

Another variable to take into account may be device oversizing. Even though manufacturers provide guidelines, the choice for a certain degree of oversizing still depends on the operator's preference and experience and the high variability of the carotid anatomy. In patient A the stent has a larger degree of oversizing, resulting in a higher closure of the stent cells at the ICA, offering more lesion protection and increasing surface covering. Oversizing may, however, lead to increased tension on the vessel wall, that may cause neointimal hyperplasia and restenosis [235]. In a previous finite element study Conti et al. [110] constructed a single atherosclerotic carotid model which was virtually treated with four different types of stents (including Acculink) and analyzed the FCAs. The authors found a higher reduction of the cell area at the middle location as in patient A. Further comparisons are not possible due to the different anatomy, the lower degree of stenosis, and different stent positioning. In the same study, it has been highlighted that LFSs in the free expanded configuration (as described by Mueller-Huesbeck et al. [169]) cannot catch differences in stent designs. Nevertheless, it is our opinion that LFSs in the deformed configuration can, however, be relevant to measure the maximum plaque particles potentially protruding through the stent struts, especially when similar devices are compared in different conditions. LFSs may improve and refine the FCA analysis. In fact, cells with similar FCAs may result in various deformed shapes which influence the LFSs (see the ICA segment in Figure 5.8) and Figure 5.9) for both patients), suggesting that both measures are complementary scaffolding parameters. LFSs may be regarded as a measure of how opposite struts of a single cell are tied, i.e. how the cell is assembled.

An obvious observation from our results is that the specificity of the lesion influences stent behavior and its scaffolding capability. CAS success is often thought to be influenced by grouping stent designs, i.e. open versus closed stent design, but this may be too basic as previously suggested [252]. To refine the discrimination, other studies refer to FCA in the free expanded configuration (more than open versus closed design) to

be an important parameter in CAS failure [166]. Other stent characteristics, however, such as conformability in angulated arteries and low radial force, play a role in selecting the appropriate stent [169,277,285,292].

Measurements of the maximum free cell area and the cell pore diameter of the free expanded stent previously proposed [169] can be misleading as the deformed configuration of the deployed stent in a tortuous vessel is neglected. Our approach may be more suitable to analyze the cell support at the lesion. Our results also suggest that global values may not be adequate for an appropriate analysis as they can mask zones at higher risk for embolization (i.e. at the lipidic plaque location). According to Table 5.5, the mean values of FCAs and LFSs do not show any difference between the two patients, even though the two stents behave very differently. On the other hand a visual evaluation of the scaffolding parameters of the virtual implantation allows a direct assessment of the possible CAS outcome scenarios.

A recent study, using a similar strategy as ours, compared vessel changes after virtual balloon expanded coronary stenting with clinical images from two patients [293]. They could reproduce the general geometrical features of the stented vessel and performed both a qualitative validation (comparing the conventional angiographic images of the interventional outcome and the numerical results) and a quantitative analysis measuring the straightening of the vessel in one patient for whom 3D CTA data were available. Although their results suggest the feasibility of their numerical approach, the differences in the interventional procedure, vascular district and parameters used for the validation, make a direct comparison with the results of our work difficult.

5.4 Limitations

The main limitations of our study are related to the imaging techniques used to retrieve pre and post-operative data. The routine pre-operative CTA scans do not provide accurate information about the vessel wall and more importantly about soft plaques.

Validation of the results should ideally be based on imaging techniques that allow a direct comparison with the post-op 3D stent configuration and/or are able to quantify the ISA which cannot be measured by conventional angiography. Post procedural angiography in a hybrid angiosuite offers a higher detail compared with CTA. Inadequate CTA resolutions can mask abrupt changes of the plaque morphology introducing inaccuracies of the pre-stented vessel geometry, which may be

amplified by the smoothing algorithms applied to obtain a "clean" surface for model meshing. The arterial configuration is acquired by CTA at a certain phase of the cardiac cycle, which may be different during post-procedural imaging due to a different pressure load. The position of the neck also changes the carotid configuration [169, 294] potentially raising mismatches between the numerical and the actual configuration.

The difficulties that may be encountered in linking pre- and post-treatment imaging data can be shown by some of the pre-treatment sequences obtained in patient B (for whom the computational results showed less agreement with the clinical data). Figure 5.10A shows how translation of the artery (due either to patient movements, heart rate or blood pressure changes) during the injection of the contrast agent (pre-stenting) modifies the curvature and configuration of the vessel.

Rigorous validation using *in vivo* data thus requires strict protocols, to obtain high resolution CTA. Ideally, an identical position of the patient should be used during the procedure with stable hemodynamics. We believe that these factors contribute to an initial mismatch between pre and post operative data as displayed in Figure 5.10B. Moreover the angiographic pictures show irregularities and ulceration of the plaque anatomy which could not be detected by the CTA scans due to the low resolution in the axial direction (arrows in Figure 5.10).

Although the level of complexity in the simulations is high, there are still important simplifications on the *in vivo* loading (ignoring blood pressure, pre-stretching and pre-stresses) and on the lesion morphology (lack of ulceration, thrombus or fibrous cap, assumptions on vessel thickness) as many of these features are not detected by clinical routine CTA scanner. Multi detector scanner and specific reconstruction algorithms may improve the lesion imaging [295]. These factors, together with the high variability of the biological materials, complicate a correct per-patient calibration of the anisotropic material models. We used an isotropic material model, which might not adequately describe the real biomechanics of the vascular tissue [243]. We therefore implemented a faster and easier tuning of the material behavior as described in the methods section. We needed to scale the original arterial stress-strain curve to obtain a stiffer material which achieved a better matching with the *in vivo* data in both cases. This is in line with the results of Auricchio et al. [243] who found larger vessel deformation with the mentioned model when compared with other literature data. Even though the limited number of cases does not allow any statistical consideration, one might speculate that when dealing with *in vivo* structures even accurate *ex-vivo*

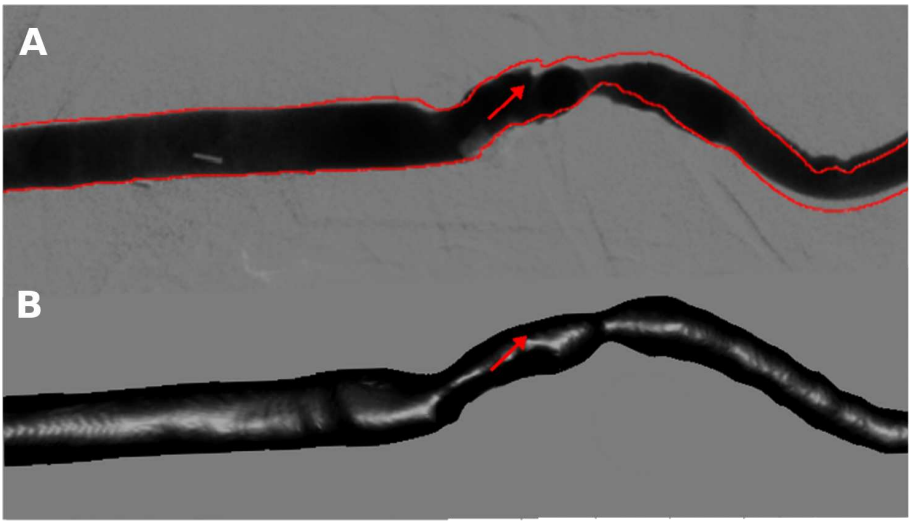

FIGURE 5.10: Mismatches of the pre-operative condition between conventional angiography and the reconstructed model. *A* Arterial configuration changes during contrast agent injection. The border (in red) of the vessel from angiography at a certain instant is overlaid to the angiography at a subsequent instant clearly showing the modification of the lumen shape due to loading factors. *B* The arterial geometry from the CTA is depicted. The red arrows indicates the irregularities not detected in the CTA *B*, which are visible in the angiography *A*.

experimental material description may underestimate the real stiffness of the treated vessel if the pre-stress condition and the interaction with surrounding structures are neglected. To overcome the latter problem, alternatively to our approach, spring elements might be considered to describe these interactions as previously suggested [241].

5.5 Conclusion

In the present study we used finite element computer model simulations to imitate CAS procedures, and applied automatic tools to quantify vessel scaffolding in two patients. Results show the feasibility of the proposed method with an overestimation of the predicted stented lumen diameter of $5.31 \pm 8.05\%$ and $4.12 \pm 9.84\%$ for the two patients compared to the clinical outcome. The quantitative measurements of the incomplete stent apposition, free cell areas and largest fitting spheres highlight the variability of device behavior in relation with the target lesion. In general free cell area depends on the target diameter and oversizing while

largest fitting spheres and apposition values are influenced by the local concavity and convexity of the vessel region. The proposed method, pending a more accurate 3D *in vivo* validation with a larger number of datasets, may be an additional tool for cardiovascular interventionists in complex anatomy. This may result in a proper selection of stent design and more accurate positioning resulting in reduced number of post-procedural stroke by better assessing the potential risk of embolization a priori.

Four

Virtual cerebral artery stenting

CHAPTER 6

Influence of stent design and vessel anatomy on intracranial aneurysm stenting

In this section of the thesis the vascular district of interest changes, moving towards the cerebral branches of the internal carotid artery. In this chapter three patient specific cerebral aneurysms were virtually treated with simulated deployment technique using three different stents. The differences in outcome due to the stent designs (open vs closed cell) are highlighted in each vessel geometry using geometrical parameters. The results were published in :
"Our capricious vessels: The influence of stent design and vessel geometry on the mechanics of intracranial aneurysm stent deployment". [1]De Bock, S., [1]Iannaccone, F., De Santis, G., De Beule, M., Mortier, P., Verhegghe, B., Segers, P., *Journal of biomechanics, (2012)* [250].

6.1 Introduction

A cerebral aneurysm is a vascular disorder in which a blood vessel in the brain shows a balloon-like swelling of the wall, due to a weakening of the vessel wall layers, with a propensity for rupture. Intracranial

[1]First joint co-authorship

aneurysms are not uncommon, with an estimated prevalence in the adult population between 1 and 5% [14]. Fortunately, an estimated 50 to 80 % of cerebral aneurysms do not rupture during a person's lifetime [296]. However, aneurysm rupture, leading to subarachnoid hemorrhage, is associated with a high mortality (45–75%) and morbidity [297], preventive treatment to reduce rupture risk is very appealing.

To reduce the risk of rupture, detection is usually followed by elective therapy. Treatment options are clipping of the aneurysm by craniotomy, endovascular coiling with platinum wires and stent supported coiling. This last option is commonly performed for wide-necked and fusiform aneurysms, with the stent serving as a scaffold for the coils. From a mechanical point of view, these stents must have longitudinal flexibility to adapt to the curved vasculature, and a sufficiently low radial stiffness to prevent vascular damage. The current intracranial stents in use can be categorized by design in two major groups: open and closed-cell self-expanding nitinol stents. Although it has been shown that both designs can successfully assist coiling, each type is associated with its own limitations [298, 299].

These issues were the rationale for [298] to investigate the influence of stent mesh pattern on the mechanical properties of closed and open cell designs, coupling finite element modeling (FEM) and experimental bench testing of fabricated nitinol stents. There has been an increasing interest in simulating the mechanical deployment of stents, both in simplified [167, 173, 300] and patient specific vessel models [168, 301]. Although computational tools are being developed for the pre-operative decision making process and planning, the state-of-art of virtual endovascular aneurysm treatment is often based on a geometrical projection method that does not take into account the deformation of the vessel model and neglects the stent mechanics [216, 302].

It is known that stent placement induces changes in the vessel geometry [149] and that incomplete strut apposition may be associated with adverse effects such as late stent thrombosis [219] in the coronary circulation. The position of stent struts have been shown to have considerable impact on the local blood flow patterns and wall shear stress [213, 302]. Clinical studies have evaluated thromboembolic and ischemic events associated with stent assisted aneurysm coiling [303, 304], and while low and oscillatory flow and shear stress may be associated with these adverse effects, they also induce thrombus formation in the aneurysm, and hence decrease its risk of rupture [305, 306].

Previous experimental and numerical research on intracranial stenting has focused on idealized vessel geometries and experimental setups when assessing the mechanical behavior of stents [298,299,307].

While allowing for a straightforward comparison of stent behavior, the model simplifications do not allow to capture certain *in vivo* conditions. In an attempt to further increase the realism and usability of cerebral stenting simulations, the presented study hopes to contribute and improve virtual aneurysm treatment, using a new patient specific environment as a possible pre-operative tool to evaluate different stent geometries. In this study we examine the virtual deployment of three stent designs in three different intracranial aneurysm geometries, quantifying the strut coverage of the stented aneurysm neck, induced vessel straightening and stent apposition to the vessel wall.

6.2 Materials and methods

6.2.1 Patient specific aneurysm models

Three different cerebral aneurysms were selected from an image database, collected by the Biofluids Mechanics Lab (Charité—University Hospital, Berlin). As can be seen from the models in Figure 6.1, and the geometrical parameters in Table 6.1, no two aneurysms or parent vessels are alike. The selected geometries consist of one narrow necked (A3) and two wide necked (A1 and A2) aneurysms, geometrically defined by [308] as aneurysms with a neck diameter larger than 4 mm. The parent vessels show different diameters and diameter tapering over the aneurysm, a different branching configuration, and a difference in tortuosity. The most notable feature is the large vessel curvature proximal of the aneurysm in geometry A2.

The geometries were obtained as a triangular surface mesh (STL), with segmentation being previously performed [309]. Because information on the wall thickness was not available, a uniform wall thickness of 0.5 mm was assumed [310]. The 3D vessel wall was reconstructed and meshed using the method proposed in [172], implemented in pyFormex (http://www.pyFormex.org), a program for generating and manipulating geometrical models of 3D structures by mathematical operations. Starting from a surface model of the vessel lumen a multi-block structured and conformal hexahedral mesh of the vessel wall was generated. The mesh element type was incompressible quadratic brick with reduced integration (C3D20RH by Abaqus convention) and the material model was isotropic second order hyperelastic polynomial (with material parameters from [311].

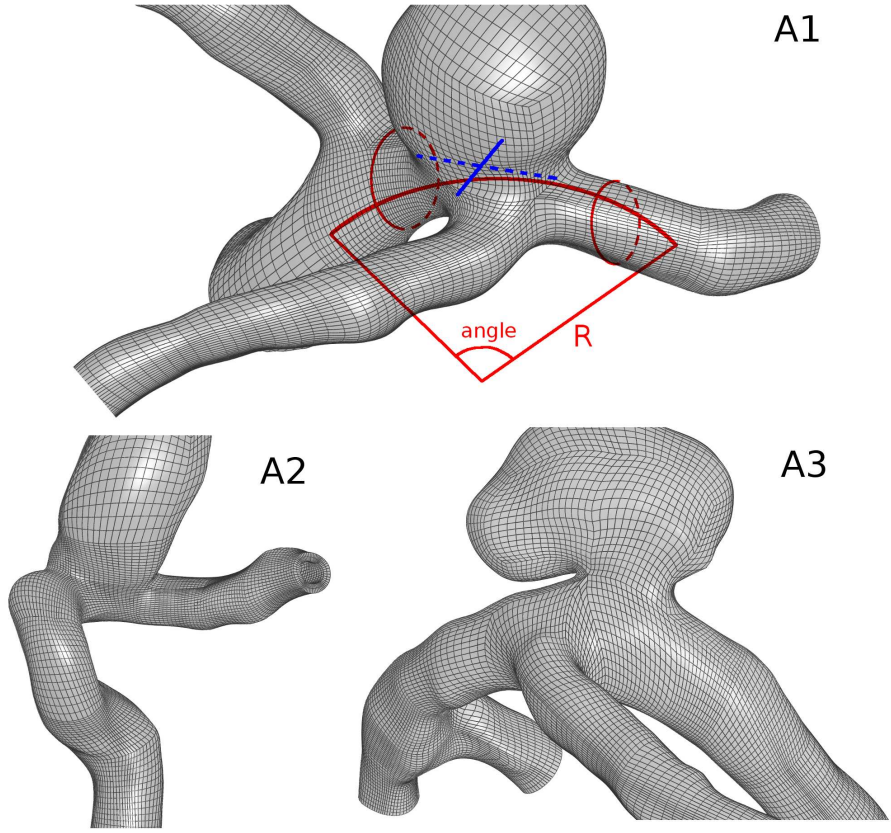

Figure 6.1: The meshed aneurysm geometries; vessel A1, A2 abd A3 Geometric vessel and aneurysm parameters are indicated A: vessel diameter proximal and distal to the aneurysm location, circle segment approximation angle and radius R, and the aneurysm neck dimensions in circumferential (full line) and longitudinal (dashed line) directions.

Table 6.1: Geometrical aneurysm dimensions; circumferential and longitudinal diameter measurements of the aneurysm neck, proximal and distal vessel diameter measurements, angle and radius R of a circle segment approximating vessel in the stented region, the original diameter of the inserted stent, and the number of elements used to mesh the geometry.

	Neck dimensions (mm × mm)	**Dist–prox vessel ⌀ (mm)**	**Angle (°)**	**Radius (mm)**	**Stent ⌀ (mm)**	**# elements**
A1	4.7×5.2	2.0–3.0	51	10.6	3.5	30720
A2	4.5×5.1	1.6–2.4	118	7.4	3	20480
A3	2.8×3.3	2.6–3.0	92	7.2	3.5	35840

6.2.2 Stent models

Three stent geometries were selected for the analysis: two generic closed-cell designs (C1,C2) and a design resembling the open cell Neuroform (Stryker Neurovascular, Fremont, California, USA) stent (N1) (Figure 6.2). The geometries of the closed-cell models were composed of hexagons according to Pythagorean tessellation theory [298]. All stents were constructed with the same strut thickness and width of 0.06 and 0.065 mm respectively. All stents were 0.5 mm oversized with respect to the vessel diameter (for undeployed stent diameters see Table 6.1), to allow for adequate deployment and stability of the stent. As a consequence, six stent geometries were created: three stents with diameters of 3.5 mm inserted in A1 and A3 and three stents with diameter of 3 mm inserted in A2. The geometric parameters and number of mesh elements can be found in Table 6.2. The stent meshes were generated with pyFormex, using a database of 2D building blocks for the straight and curved struts, and the strut connections (Figure 6.2). The blocks were assembled to create the repeating stent unit cell. The 3D stent was created by replication, extrusion and a cylindrical coordinate transformation on this unit cell. This bottom up approach results in a structured mesh, with direct control on the element quality.

The stress–strain relationship of the nitinol alloy (Ti—55.8 wt% Ni) was obtained from literature [251] and implemented using a user subroutine in Abaqus following the model of [252]. As in the paper by [251] only uniaxial tension tests were conducted, we assumed symmetry in compression. For all models, quadratic hexahedral elements with reduced integration (C3D20R) were used, as they have been shown to yield a more accurate solution compared to linear tetrahedral elements for mechanical simulations, in particular when using non-linear material behavior [94, 312, 313]. Quadratic hexahedral elements are robust and stable and although they are, per element, computationally more expensive, it is possible to achieve a good accuracy with coarser meshes. A mesh sensitivity analysis was performed, and established the stability and convergence of the FEM results.

TABLE 6.2: Stent dimensions and mesh sizes.

	Thickness (mm)	**Width (mm)**	**# repetitive units over L**	**L (mm)**	**# elements**
C1	0.06	0.065	5	10	15072
C2	0.06	0.065	5	10	15072
N1	0.06	0.065	4	10	12480

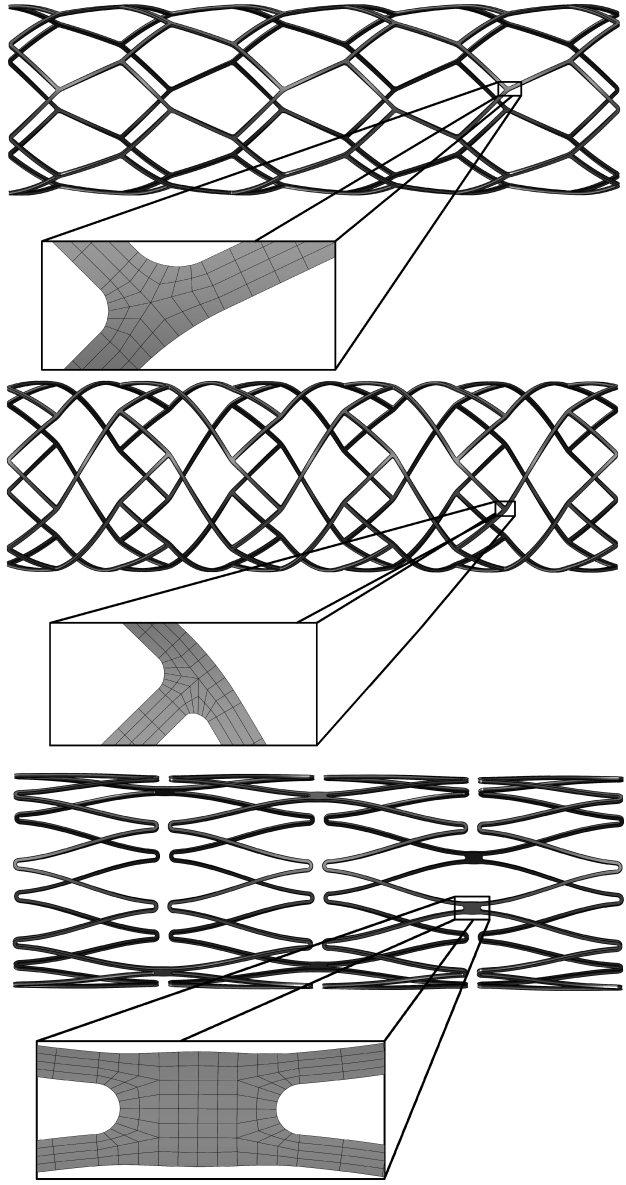

Figure 6.2: The 3 stent designs used in the study, with a detail of the second order hexahedral mesh; from top to bottom: C1,C2 and N1.

6.2.3 Virtual stent deployment procedure

The commercial finite element solver ABAQUS/Standard (Simulia Corp, Providence, RI, USA) in combination with the open source pyFormex pre- and post-processor was used to virtually implant each stent in all three vessel models. The simulations were performed using large deformation analysis and Newton's method as a numerical technique for solving the nonlinear equilibrium equations. The stent placement was simulated in three steps: crimping, bending and the subsequent deployment in the patient-specific geometry. All steps were solved as a displacement driven contact problem, using the surface to surface contact discretization with finite sliding tracking approach. The penalty method constraint enforcement method was used to approximate hard pressure-overclosure behavior. The motion was imposed on a cylindrical sheath that represented the actual delivery system accommodating the stent. The virtual displacement of the catheter was imposed using a user subroutine (DISP) to analytically define the nodal displacements. The centerline of the vessel was extracted from the vessel geometry using vmtk `http://www.vmtk.org/`. To enable analytical computations, the centerline was approximated using circular arcs. The sheath was bent according to these arcs. The radius of curvature was modified in relation to the analysis time step. In this way the bending of the stent occurred smoothly, helping the convergence of the implicit simulation. The complete procedure is explained more in detail in chapter 3. The stent deployment procedure at different procedural times is shown in Figure 6.3.

6.2.4 Treatment evaluation

We evaluated the impact of the implanted stents in the different aneurysm geometries, focusing on the following, potentially clinically relevant, parameters:

1. the strut coverage in the aneurysm neck, defined as the percentage in neck area that is covered by the expanded stent surface. This is calculated by taking a view cut of the vessel at the location of the aneurysm neck, with the view perpendicular to the vessel centerline and circumference. The percentage of stent surface in the aneurysm neck is quantified using an image based pixel count method;

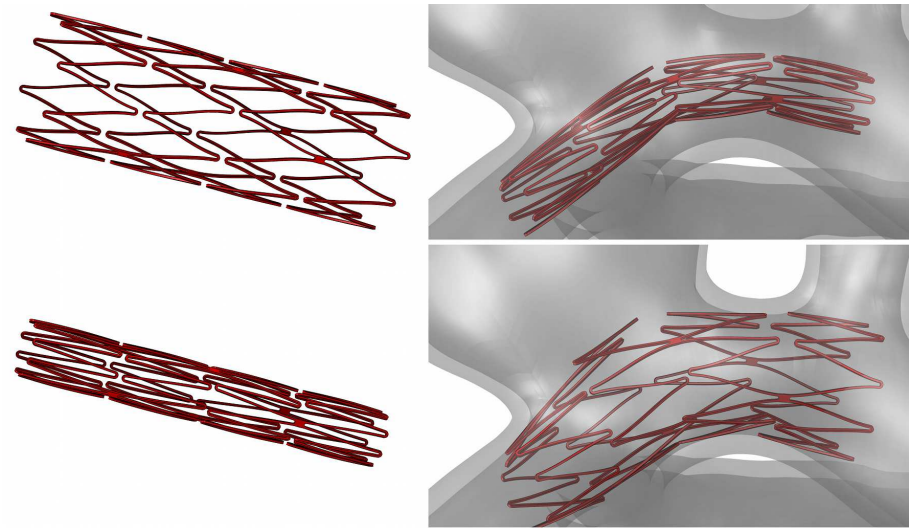

Figure 6.3: The complete deployment procedure, starting from the undeformed stent. The stent is crimped and bent according to the vessel geometry. Upon release, the super-elastic stent expands to fit the vessel geometry.

2. vessel tortuosity is calculated pre- and post-stenting, as a measure of the vessel straightening induced by the stent insertion. It is defined as

$$\tau = \frac{L}{D} - 1 \tag{6.1}$$

where L is the length of the (tortuous) centerline from the origin to the end of the stented region and D is the straight distance between these two points [314]. The tortuosity measure describes the fractional increase of the vessel length, relative to the shortest path between its two endpoints (a straight vessel having a $\tau = 0$).

3. incomplete strut apposition to the vessel wall, computed as the distance from the external stent surface nodes to the closest vessel surface element. In order to quantify the amount of stent struts that are well apposed, we computed the percentage area of stent struts within a threshold distance of the vessel wall, relative to the total stent area. Two thresholds (0.1 and 0.2 mm) were chosen to differentiate in the severity of the malapposition, with a third, high threshold (0.5 mm) indicating stent struts that are located at the aneurysm dome or at vessel branches.

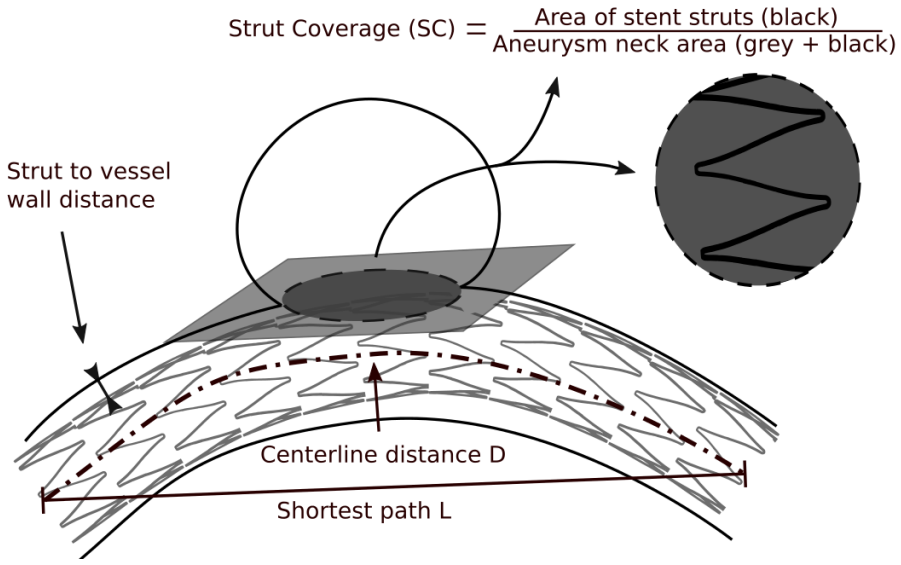

FIGURE 6.4: A schematic view of the calculated parameters used for treatment evaluation; the strut coverage (SC), tortuosity τ and the apposition, quantified by the strut to vessel wall distance.

6.3 RESULTS

6.3.1 Strut coverage

The strut coverage of the aneurysm neck is visualized and quantified in Figure 6.5. While for an undeformed stent, the percentage stent strut surface area covering a cylindrical vessel of the same diameter is similar for the three designs (8.1%, 8.4% and 8.3% for C1, C2 and N1 respectively), notable differences can be observed between different stent designs, and different aneurysm geometries, with clear dissimilarities between wide (A1, A2) and narrow-necked (A3) aneurysms.

In the wide neck A1 and A2 geometries, the closed-cell designs do not cover the aneurysm neck but pass the aneurysm with, approximately, a diameter that is the same as the parent vessels diameter, resulting in low strut coverage (7.3/6.5% for C1 and 8.2/7.5% for C2 in A1/A2). On the other hand, the N1 stent can more easily adapt to the vessel shape (11.5/11.8% for N1 in A1/A2). The A3, having a narrow neck, allows for all designs to cover the aneurysm neck surface (9.5/10.5/9.8% for C1/C2/N1 in A3).

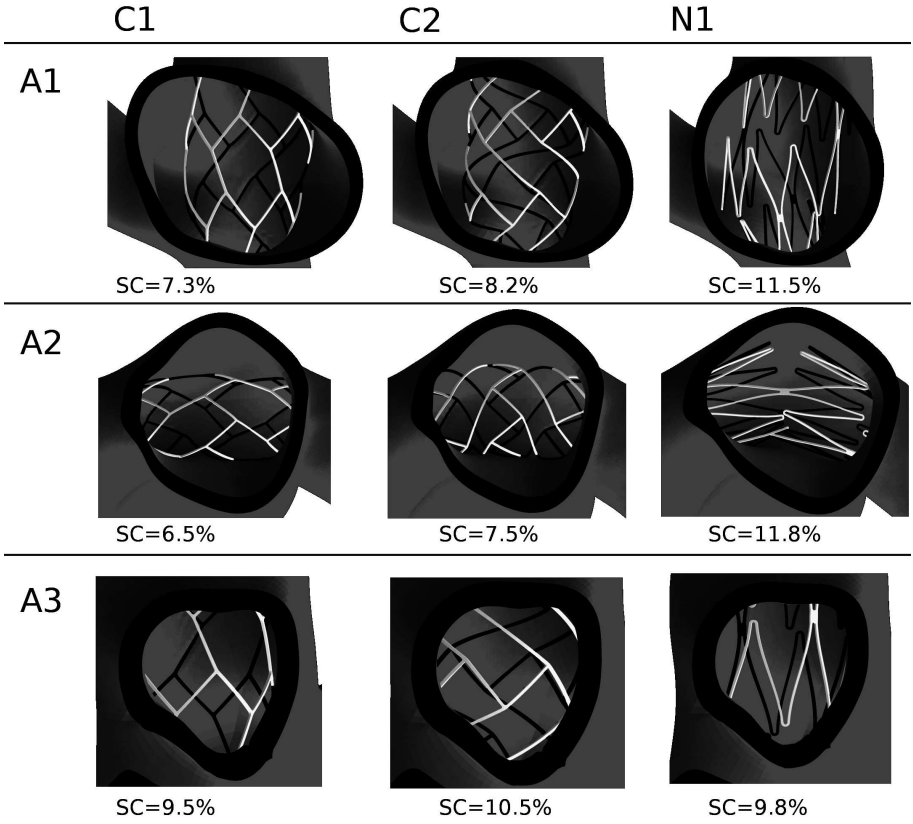

Figure 6.5: Percentage strut coverage (SC) of the aneurysm neck, for all three designs in the three aneurysm geometries.

6.3.2 Tortuosity

The vessel straightening is summarized in Table 6.3. It can be clearly observed that this straightening behavior is stent design dependent, with the open cell design inducing the least straightening. Additionally, the difference in straightening of stent C2 in aneurysm 1 (41%) and 3 (21%) shows that different target anatomies can invoke different stent-vessel reactions, even when the original tortuosity measure is similar (i.e., 0.11 and 0.10).

6.3.3 Apposition

All the investigated stent designs show incomplete strut apposition to the vessel wall, and this occurs in all three aneurysm models. Figure

TABLE 6.3: Tortuosity measure τ, and the relative change (%) versus the unstented condition.

	Tortuosity Unstented	**Tortuosity τ C1**	**Tortuosity τ C2**	**Tortuosity τ N1**	**Increase τ C1**	**Increase τ C2**	**Increase τ N1**
A1	0.11	0.06	0.07	0.11	-46%	-41%	-5%
A2	0.39	0.26	0.31	0.37	-32%	-19%	-3%
A3	0.10	0.05	0.08	0.09	-51%	-21%	-7%

6.6 displays the calculated apposition measures, as the fraction of well apposed stent area with a given threshold to the complete external stent surface.

The quantitative results show that the N1 design does not appose well to the vessel wall, and less than 30% area of struts are within 0.1 mm of the vessel wall, for each geometry. However, as can also be seen from the visualized results, the open cell design better adapts to the vessel widening at the aneurysm (in the background of Figure 6.7, indicated by the arrowhead; also visible in Figure 6.5). Well pronounced malapposition occurs at the location of vessel tapering, and at the end of the stented location when situated at a vessel curve (indicated by an arrow in Figure 6.7). Additionally, for closed-cell designs with low

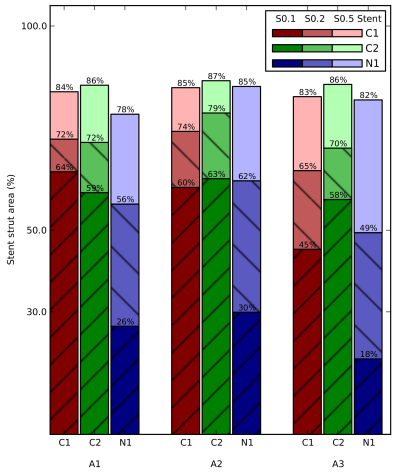

FIGURE 6.6: Percentages of the stent surface S with distance to the vessel wall less than thresholds 0.1, 0.2 and 0.5 mm, for the three stent designs (C1, C2, N1) and three aneurysm geometries (A1, A2, A3).

flexibility, incomplete strut apposition occurs at curved vessel regions (double arrowhead indicators). However, this remains limited due to the large straightening of the vessel. At the same location, for the open cell stent, fish scaling is present. This "fish-scaling", the tendency of stent struts to protrude in- or outwardly, is another aspect of stent deployment of an open cell design. The fish scaling of the N1 is well detected from the simulations and can occur at different locations:

i in the inner curvature of the vessel, protruding in the parent artery (Figure 6.7—double arrowhead indicator)

ii at an enlargement of the vessel diameter due to the (wide necked) aneurysm (Figure 6.7A1/N1 and A2/N1, at the aneurysm neck)

In these aneurysm geometries, incomplete apposition of the stent struts is, for the large part, located at the same locations for the different designs, with the largest differences between designs originating from fish-scaling of the N1 design, visible at multiple locations. Table 6.4 summarizes the performance of the stents, averaged over the three aneurysms.

6.4 Discussion

In this study we have used finite element analysis to gain insight into the deployment and mechanical behavior of cerebrovascular stents and their interaction with the vascular wall. The simulation results are used to assess how a stent meets the primary mechanical requirements, and to quantify possible adverse effects of stent deployment. The strut coverage of the aneurysm neck can be an indirect indicator of coil protrusion and can promote aneurysm occlusion by reducing the blood flow in the dome. The amount of struts covering the aneurysm neck depends not only on stent design, but also on the vessel geometry. While this dependence

Table 6.4: Tortuosity increment, strut coverage and percentage of stent surface with distances less than the chosen thresholds. Values are averaged for each stent on all the vessel geometries. .

	Tortuosity increment (%)	**Strut coverage (%)**	**S0.1/Sstent coverage (%)**	**S0.2/Sstent coverage (%)**	**S0.5/Sstent coverage (%)**
C1	-42.9±9.8	7.8±1.6	56.7±10.1	70.4±5.1	83.8±1.1
C2	-26.9±11.9	8.7±1.6	59.8±2.6	73.4±4.6	85.8±0.7
N1	-5.1±1.6	11.0±1.1	25.0±5.9	56.0±6.4	81.8±3.4

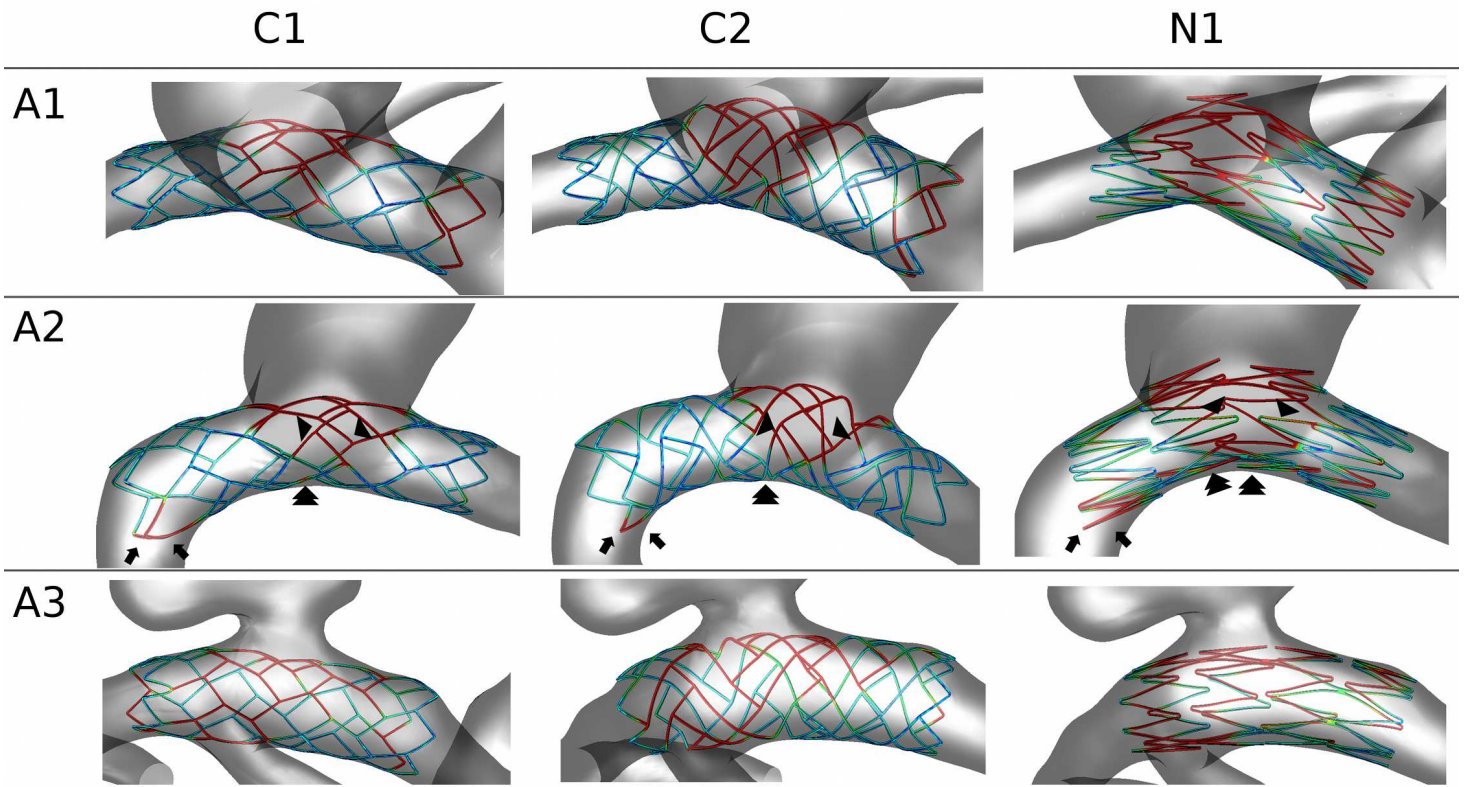

FIGURE 6.7: Stent apposition to the vessel wall for all cases. The contourplot shows the distance to the vessel wall, ranging from blue (0 mm) to red (>0.2 mm).

on diameter has been previously reported in silicone mock arteries [299], the finite element results take into account the complex geometry of patient-specific aneurysms.

In general, for a wide-necked aneurysm, closed-cell designs adapt less to the aneurysm geometry than open-cell designs. Closed-cell designs can be designed to have a low bending stiffness [298]; however for the more flexible (C2) design investigated, the low straightening observed with the open-cell design is not reached. As demonstrated here, open-cell stents like the N1, are more adaptable to the global vessel curvature and tortuosity, and induce a low straightening of the vessel. Vessel straightening by the Neuroform has been previously reported, and it could potentially induce arterial kinking, uneven mechanical strain distributions, or other mechanical effects, which might cause in-stent stenosis [315].

The open-cell design does have some well known shortcomings, which appear in the two wide necked aneurysms. In those cases the stents show outward prolapse of struts into the aneurysm dome (i.e. fish-scaling) when situated at a convex curve of a parent artery, and into the vessel lumen, at the concave regions of an artery. For the former case, fish-scaling can cause an increased opening of one or more stent cells, which may facilitate migration of small coils through the stent cells [316,317]. In the latter case, the inward protruding struts will likely promote a hemodynamic effect, inducing unfavorable flow patterns that could lead to stent thrombosis and/or in-stent stenosis. The presence of struts in the lumen may also obstruct or encumber the placement of the thromboembolic coils or other endovascular devices. Moreover, both for open and closed designs, quantification of incomplete stent apposition can be one of the predictors of long term patency of the stented aneurysm [318].

An experimental in vitro study reports kinking and incomplete stent apposition for closed cell design at high curvature angles [299], and *in vivo* studies also suggest that closed cell designs are more susceptible to malapposition [319,320]. Contrary to these findings, the results obtained in these vessel geometries suggest that the N1 design gives worse apposition values compared to the closed cell designs. It is possible that these discrepancies arise from the geometries of the parent artery, that can easily accommodate both stent designs, and from the design of the investigated closed cell stents, which are either overly stiff, and straighten the vessel, or sufficiently flexible, and appose well. Furthermore, previously discussed fish-scaling of the N1 design also contributes to the incomplete apposition.

The presented virtual framework can be used to assess the risk of adverse effects of stent design, and predict the stent behavior for each

specific patient in an acceptable run time (3 h on a modern desktop pc). In contrast, when using a projection method, these mechanical effects would not have made an impact on the results. Furthermore, *in vivo* assessment of stent deployment, e.g. as an indirect indicator for good wall apposition, has proved to be extremely challenging [318]. The main body of the nitinol stents currently on the market is usually not visible under fluoroscopy in clinical practice. Hence, very little data is available about cerebral stent positioning, after already 8 years of use in clinical practice [321]. Our approach allows visualization and quantification of stent apposition.

In future works, the method presented can be used to also assess the fatigue life of stent designs, specific for each patient. Furthermore, a specific future application lies in hemodynamic investigations. The solid mechanic finite element results can be used as a starting point for CFD calculations. This research can be an additional step towards bringing pre-operative computational engineering results to the operating room. The presented method can serve as a link between stent design and clinical implications of stent deployment. However, clinical and pathophysiological implications of mechanical considerations should be further investigated in animal models or in a clinical setting.

Even though previous experience in the finite element method and its validation [174] make us confident in the presented results, the lack of specific, experimental validation is one of the shortcomings of the manuscript. Other limitations of this work are model simplifications, such as the lack of realistic values for the wall thickness, which varies along the vasculature [322]. The use of an estimated wall thickness is however necessary when image modalities do not support localized thickness measurements, as in this case. Further simplifications include the material properties of the vessel wall, modeled with an isotropic hyperelastic constitutive model which does not take into account the anisotropy of the vascular wall. Recent work on the multiaxial response of cerebral arteries [323] or on the different layers of the internal carotid artery [112] can be considered for a more accurate and complex material formulation. For the purpose of this study, we find that the isotropic constitutive relation offers adequate detail for comparing the mechanical behavior of the stents. A more constraining aspect is the lack of the surrounding tissues which can influence the vessel wall response, probably reducing the vessel straightening due to the interconnectivity of surrounding tissues. However, for the purpose of this comparative study, these approximations are considered to be acceptable.

6.5 Conclusion

This study provides a new computational framework to virtually implant stents in a patient based cerebral aneurysm model to assess the impact of stent placement and provide insight into the biomechanics of the stented aneurysms. The following conclusions can be drawn from this analysis:

i due to the intrinsic adaptability of the open cell design, the Neuroform-like stent adjusts better to the wide-neck aneurysm geometries, resulting in higher percentage of struts covering the neck;

ii altering the design can lower the bending stiffness of closed cell stents, yet for the investigated designs, the high flexibility and low vessel straightening of an open cell stent was not reached;

iii stent malapposition is present for all investigated cases but the open cell stent shows a higher region of stent struts not apposing well to the vessel wall due to fish scaling.

The stiff closed cell design forces the vessel to adapt to the stent shape, and as such, it has a higher number of well apposed stent struts. For the presented designs and aneurysm geometries, the more flexible closed-cell apposes best.

CHAPTER 7

In vivo case study of stent supported coiling

The previous chapter showed the potential of the numerical environment and geometrical analysis to compare different stent designs for cerebral aneurysm treatment. Nevertheless a validation with a real procedure is needed to assess the numerical outcome, especially because model simplifications and assumptions can alter the results of the simulated procedure. In this chapter an *in vivo* case with pre- and post-operative data has been compared to the virtual procedure to prove its reliability. Particular attention was given to the stent delivery technique which has been shown to have an impact on the final stent configuration.

7.1 Introduction

Series of clinical studies have consecutively provided guidelines and have demonstrated the efficacy of endovascular treatment of intra-cranial aneurysms [16, 324–326] also in the long term [327].

The interventionalist community started endorsing the coiling procedure after the positive results of the International Sub-arachnoid Aneurysm Trial [16], recognizing aneurysm coiling as an effective and permanent treatment option in small necked aneurysms.

Still, technical limitations prevent complete occlusions of large and wide necked aneurysms. To overcome this issue, neurovascular stents

have been designed to avoid herniation of the coils into the parent artery lumen [328]. Additionally, these stents have shown to offer other advantages by helping diverting blood from the aneurysm, hereby promoting dome thrombosis [328, 329] and providing a matrix for orifice endothelialization [12, 328, 330, 331].

Despite the encouraging outcomes, some issues are yet to be addressed. In particular incomplete stent apposition (ISA) seems related to adverse events [219, 303, 304]. Assessment of deployed stent configuration and stent malapposition is consequently of high importance [325, 326, 332] also for subsequent re-treatment of the aneurysm or distal vascular access [333].

This seems particularly relevant for closed stent designs [320, 321, 333] but stent related data in the intra-cranial vasculature remain scant [218] due to the limitations of the routinely acquired imaging techniques. Conventional angiography is unable to visualize current nitinol neurovascular stents due to the reduced strut thickness and material attenuation. Visualization improvements with radio-opaque markers are not yet sufficient to provide information regarding the deployed configuration [333].

Advances in high-resolution imaging with C-arm flat-panel angio-CT (FPCT) seems promising to assess the stent structure *in vitro* around bends [218, 318, 334]. FPCT has also shown the ability *in vivo* to detect ISA and the global configuration of implanted intra-cranial stents [320, 321]. 3T-MRA also appears to be able to quantify ISA but poor information of the stent configuration is given, and cannot be performed peri-operatively [321]. More recently contrast-enhanced cone-beam CT data (also known as VasoCT) have proven the ability to provide detailed and simultaneous visualization of neurovascular stents and host arteries both in experimental and *in vivo* setups [333, 335].

A finite element (FE) environment could be a solution to verify these conditions and potentially be used as a pre-operative tool to predict possible undesired events.

FE simulation have been successfully used and validated against *in vitro* models [170, 229]. Patient-specific simulations of endovascular treatments, such as stenting, have been performed in coronary [173, 301] and carotid arteries [167, 168] and cerebral aneurysms [222, 250], but rarely validation with post-procedural data have been performed [293]. This lack in literature motivated the present study, in an attempt to fill this gap.

The endovascular procedure of one patient treated with an Enterprise endovascular reconstruction device (Cordis Corporation; Miami, Fl,

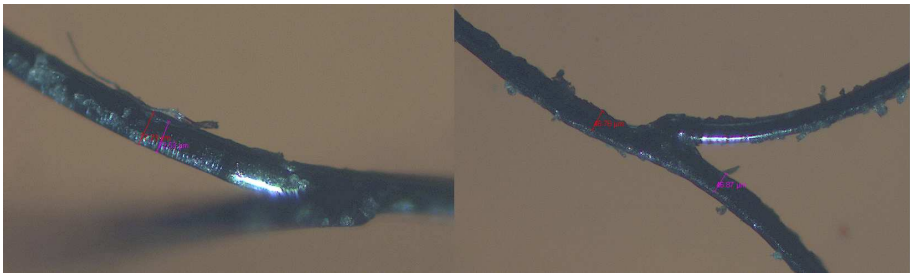

FIGURE 7.1: Optical Microscopy measurements of the Enterprise stent. A detail of the stent struts shows the measurements of the thickness (left) and width (right). Irregularities of the surface are imputable to dirtiness of the sample.

USA) has been reproduced in a FE setting showing specific challenges of a virtual patient-specific environment. The numerical deployment strategy presented in previous studies [229, 230, 250] has been improved to replicate the so-called "push-back" delivery technique as suggested by the instructions for use of the device (`http://www.cordislabeling.com`). After qualitative validation of the deployment method with previously reported experimental work [218], available pre- and post-operative CT scans were used to build the patient specific geometry and validate the final configuration of the inserted device.

7.2 Materials and methods

7.2.1 Stent geometry and material properties

The devices used in this study were Enterprise vascular reconstruction devices of different lengths (4.5×22 mm and 4.5×28 mm). This is a closed-cell design intra-cranial nitinol stent for treatment of wide-necked aneurysms. The stent geometries were obtained using X-ray micro-tomography (μCT) scans of the devices performed at the center for X-ray tomography UGCT (`http://www.ugct.ugent.be`) with a resolution of 1.4 μm. The numerical stent model with hexahedral elements were created in pyFormex (`http://www.pyFormex.org`) with the strategy already used in previous studies [230, 250] and outlined in chapter 3. Additional processing was used to remove the outer elements of the mesh until obtaining the centerline of the stent (as described in chapter 3). The centerline points were approximated by polylines and subdivided to refine the mesh and smoothed to have a softer transition of the tangents of the segments. The final stent mesh was modeled using

Timoshenko beam elements, which are reported to yield accurate results in stent modeling [336] and show stable results, even for coarser meshes [229]. The meshes counted 6200 and 6800 elements for the 22 mm and the 28 mm device respectively. The stent thickness and width were measured with optical microscopy of the device (Figure 7.1). Averaged values of 70 μm and 48 μm for the thickness and width of the devices were measured.

The superelastic behavior of the nitinol material is modeled using a user-defined material subroutine embedded in the FE solver ABAQUS (Simulia Corp, Providence, RI), based on the model described by Auricchio and Taylor [252]. Flat plate testing at 50% of the labeled diameter [299] of the Enterprise stent (4.5×22 mm) were carried out to determine the material properties of the nickel titanium alloy. The test was performed using an Instron 5942 electromechanical tensile test system (Instron, Norwood, MA, USA) at 37 °C temperature repeated 3 times to account for any difference in the initial sample position. The system was configured with a 10N load cell (Figure 7.2). The flat plate test was simulated using Abaqus/Explicit in a quasi-static analysis. Frictionless penalty contact was used. Figure 7.3 shows the mechanical result and the numerical approximation.

The test, however, does not provide the entire description of the nitinol behavior so it was used only to estimate the austenitic elastic modulus while the other parameters were taken from literature [251]. Additional tests (not reported) were performed with a radial crimping

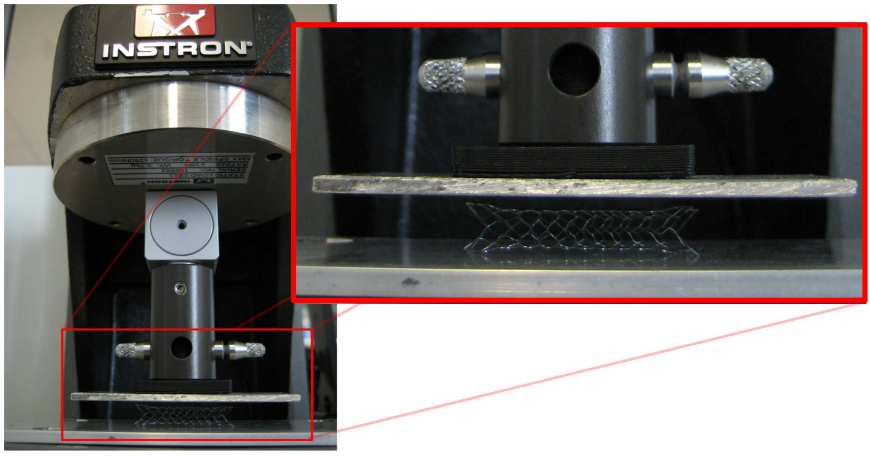

Figure 7.2: Flat plate test setup.

head (MPT Europe, Leek, The Netherlands) with an 8-segment iris to reduce the diameter of the inserted stent. As the measured radial force was too low compared to the noise induced by the friction of the machine, data were discarded for the evaluation of the additional coefficients of the Nitinol model.

The material properties finally selected for the device are summarized in Table 7.1.

7.2.2 Patient specific aneurysm model

Anonymized pre and post-operative CT DICOM data were obtained for one patient with an aneurysm located at the anterior cerebral artery. The aneurysm was treated with stent supported coiling using an Enterprise stent (4.5×22 mm). VasoCT data were acquired using a angiographic c-arm system (Allura FD20/20, Philips Healthcare, Best, the Netherlands). Reconstruction was performed on an XtraVision workstation.

In plane resolution and slice thickness were 0.4 mm and 0.2 mm for the pre-operative and the post-operative datasets respectively.

DICOM data were processed in 3DSlicer (`http://www.slicer.org/`). Due to the low contrast and to the artifacts introduced by the coil, the stent images were manually segmented slice per slice, removing the streaks of the radio-opaque material. The vessel lumen and the stent geometry were exported as triangulated surfaces (STL).

The pre-stented vessel wall was discretized using quadrilateral elements in FE-IAmesh, a meshing tool embedded in 3DSlicer [291]. The vessel wall was assumed having a constant thickness of 0.5 mm derived from the relationship between arterial diameter and thickness described in [310]. The choice was based on the following considerations

FIGURE 7.3: Flat plate test results and numerical approximation.

Table 7.1: Nitinol material parameters for the stent device. Symmetry in compression and a was assumed.

Variable	Value
Austenite elasticity (MPa)	45000
Austenite Poisson ratio	0.3
Martensite elasticity (MPa)	23333
Martensite Poisson ratio	0.3
Transformation strain	0.0437
Start of transformation loading (MPa)	450
End of transformation loading (MPa)	520
Reference temperature °C	37
Start of transformation unloading (MPa)	210
End of transformation unloading (MPa)	130
Start of transformation stress in compression (MPa)	450

1. the image modality did not allow extraction of the vessel wall
2. the image voxel size was 20 to 30 % of the lumen diameter of the stented location
3. the diameter of the stented artery had a very small variation in diameter (2.3 to 2.7 mm)

The vessel has been modeled with 4200 surface elements with reduced integration (S4R in the Abaqus nomenclature). The thickness for this planar elements was applied outward the vessel to keep the lumen size.

The wall was assumed isotropic. Averaged stress-strain of human cerebral arteries data from literature [337] were fitted with a second order reduced polynomial hyperlastic model. However, this simplification does not take into account the anisotropic behavior of cerebral arteries which exhibit lower stiffness in the circumferential direction [338] when their passive response is tested.

7.2.3 Simulation strategy

7.2.3.1 Virtual deployment method

FE simulations were performed using Abaqus/Explicit 6.12 in a quasi-static analysis. The default contact algorithm - node to face and edge to edge contact with penalty enforcement - was used.

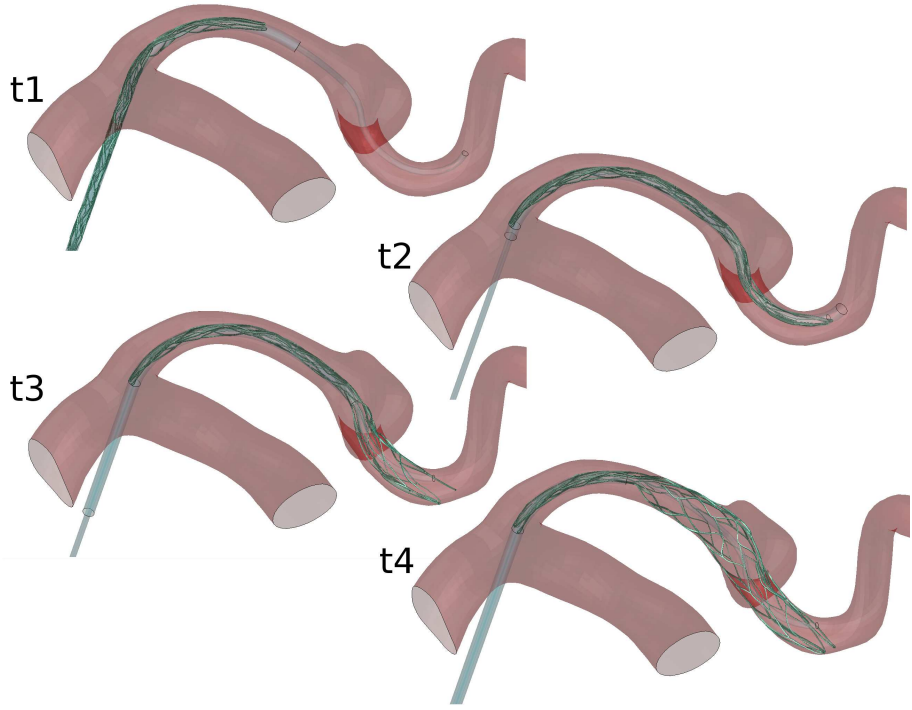

FIGURE 7.4: Deployment methodology at different time steps t_i. The stent is pushed (t_1 and t_2) and the micro-catheter is pulled (t_3 and t_4).

A small viscous surface load, added to the vessel wall to remove oscillations was kept smaller than <5% of the internal energy to avoid the influence of viscous damping on the final outcome.

To guide the stent deployment, the strategy presented in previous studies [229, 230, 250] was improved to apply more realistic boundary conditions to the cylindrical surface employed as guidewire and delivering sheath. The guidewire is bent along the centerline of the vessel (extracted from the lumen surface using vmtk - `www.vmtk.org`), the stent is crimped by reducing the catheter radius up to 5Fr (1.67 mm) [218], pushed along the guidewire and then retrieved maintaining the bottom surface of the catheter fixed to keep the stent in place. Finally the guidewire is retracted. Some instants of the procedure are shown in Figure 7.4. The detailed procedure has been presented in chapter 3. To speed up the simulation, the insertion is started from the the location where the proximal portion of the stent should lay after the delivery, to avoid unnecessary additional computational cost by simulating the

insertion from the internal carotid artery segment. Even though this method is less computationally efficient than the gradual deformation and release of the catheter presented in the aforementioned studies, the procedure guarantees a more realistic replication of the deployment in case the delivery technique has an impact on the deployed configuration (as for the Enterprise stent). In particular the deployed device is prone to under-expansion, with the typical effect of "hugging" the inner curvature of the vessel - see Figure 7.5.

7.2.4 Data analysis

7.2.4.1 Validation of the virtual deployment method

The deployment method has first been employed in a tubular structure to validate the effect of the push-back technique. The complete simulation strategy ran for 7 hours on 8 3.4GHz CPU cores on a high performance computing cluster. This simplified vessel model was approximated from previous experimental work [218]. Results of the simulated deployment of the Enterprise 4.5×22 mm stent were qualitatively compared with the CT scan of the device inserted *in vitro* in the previously mentioned study [218]. Additionally the Enterprise 4.5×28 mm was inserted to prove the efficiency of the technique and study its effect on different length sizes of the device.

7.2.4.2 Validation of the in vivo outcome

The complete simulation strategy ran for 10 hours on 8 3.4GHz CPU cores on a high performance computing cluster. The 22 mm device used in the real procedure has been inserted in the patient specific vessel geometry to match the stented location. The numerical results were

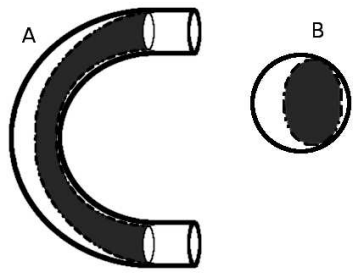

Figure 7.5: *A* Hugging effect in a curved vessel *B* and consequent ovalization of the stent section.

compared both qualitatively (by superposition of the simulated and real deployed stent) and quantitatively by measuring the tortuosity of the pre- and post-stented vessel region as proposed in a previous study [293]. To account also for the surrounding regions influenced by the device the centerline portion at the stented location was extended of 25 % both distally and proximally.

The tortuosity τ, as a measure of the vessel straightening induced by the stent insertion, is defined as

$$\tau = \left(\frac{L}{D} - 1 \right) \tag{7.1}$$

where L is the length of the (tortuous) centerline from the origin to the end of the stented region and D is the straight distance between these two points [314]. The tortuosity measure describes the fractional increase of the vessel length, relative to the shortest path between its two endpoints. The percentage ε error between the final tortuosities of the simulation and the clinical outcomes is computed as:

$$\varepsilon = \left(\frac{\tau_{simulations}}{\tau_{clinical}} - 1 \right) \times 100 \tag{7.2}$$

In order to compare the results, pre- and post-operative vessel geometry scans were registered. For this purpose a registration tool has been created in pyFormex using VTK (`http://www.vtk.org/`) functions for landmark registration. An initial alignment of the geometries was obtained by selecting three corresponding points. After, a more refined registration was performed using an iterative procedure to minimize the error distance between the two surfaces. Because of the changes in vessel shape from the pre- to the post-operative condition the landmarks were positioned on regions of the vessel far from the stented location (with the limitations of the size of the scanned region) in order to perform the registration on the portions of the vessel potentially not affected by the device.

7.2.5 Results

7.2.5.1 Virtual deployment method validation

Figure 7.6 shows the comparison of the CT scan of the *in vitro* experiment [218] and the result of the simulation in the approximated vessel model. Though some mismatch due to the difficulties to recreate the exact *in vitro* geometry is visible, it is evident that the deployment procedure can replicate the side effect highlighted from the insertion in an

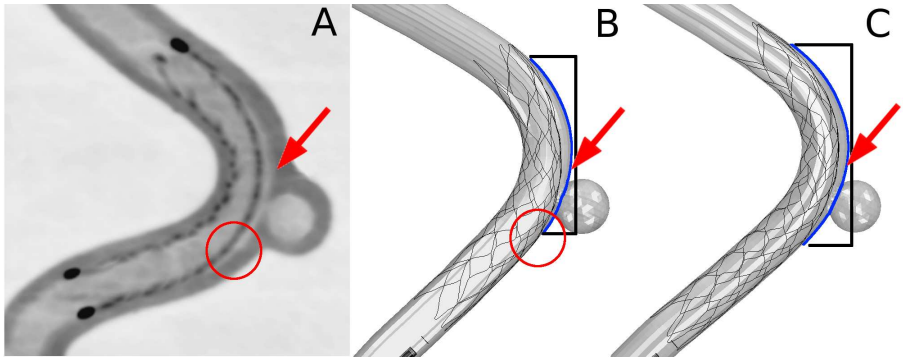

Figure 7.6: In vitro validation of the Enterprise stent deployment using the push-back technique; *A* CT scan of the experimental deployment of the Enterprise 22 mm [218]; *B* Numerical deployment of the Enterprise 22 mm; *C* Numerical deployment of the Enterprise 28 mm. The red arrow indicates the malapposed area due to hugging. The red circles indicates the malapposed zones not properly detected by the simulation in the tested case. The blue and black lines mark the different extension of the malapposed area between the two devices with different lengths.

in vitro setup. The pull-back technique leads the stent to hug the inner curvature of the vessel while leaving a large region not apposing the outer curvature. The effect is even more critical when using a longer stent which increases the malapposed area.

7.2.5.2 In vivo outcome validation

The *in vitro* validation is extended to prove the reliability of the technique in an in vivo setup. Figure 7.7 shows the superposition of the pre and post-operative vessel configuration for both the simulated and real procedure.

Despite the fact that registration errors, triggering errors of the cardiac cycle and bad lumen approximation due to the artifacts induced by the device, do not allow an accurate comparison, it is still clear that main effects of the deployed device are replicated. The stent forces straightening of the vessel which induces a translation in the proximal portion of the vessel (yellow arrow) and after the main curve of the anterior cerebral artery (red arrow). Figure 7.8 shows the superposition of the segmented stent from the post-operative data with the simulated deployed device. The clinical data show a tortuosity of 0.37, while the simulations demonstrate a tortuosity value of 0.44, which correspond to an underestimation of 18.9% of the *in vivo* data.

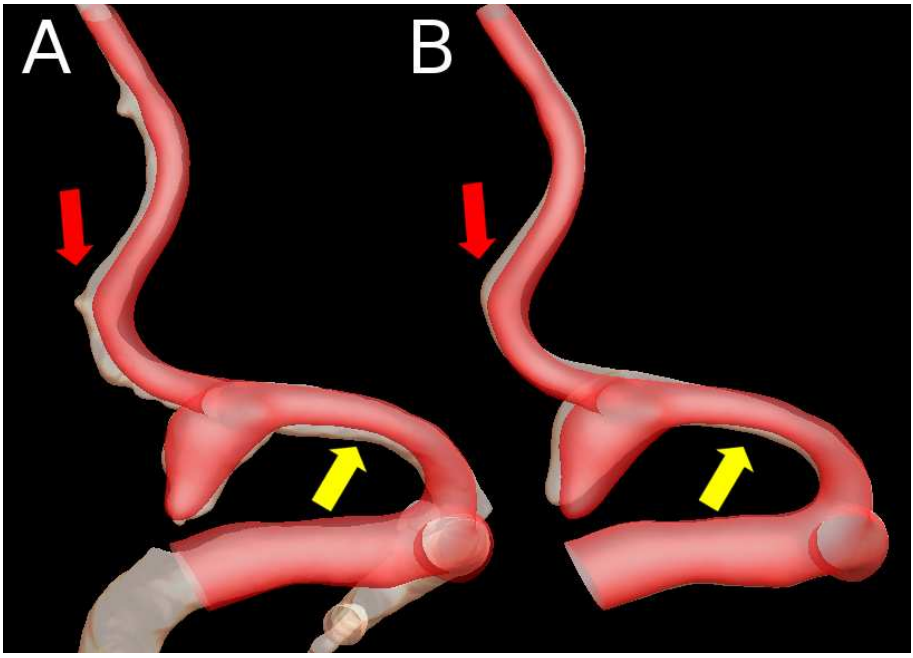

FIGURE 7.7: Final vessel configurations for the clinical *A* and numerical outcome *B*. The arrows indicates the straightening effect on the vessel.

7.3 DISCUSSION

In this work, we presented a patient-specific *in silico* evaluation of an Enterprise stent deployment. In order to catch the real mechanics of the procedure, we implemented a more realistic delivery technique which was first validated with previous experimental data [218].

Structural FE studies on cerebral aneurysm stenting are scant. Virtual stent deployment has been used to evaluate different stent positions in simplified models [300,307] mainly for further fluidodynamic analysis. These studies provide, albeit, limited information due to the planarity of the vessel and the very limited curvature which do not reflect the tortuous reality of the cerebral vasculature. More accurate simulations have been performed on patient-specific models [250] with efficient deployment strategies computing strut coverage of the aneurysm neck, wall apposition and conformability to evaluate different stent designs. Ma et al. [222] deployed a flow diverter in a patient specific geometry using an accurate stent deployment strategy comparable to the one presented in this work.

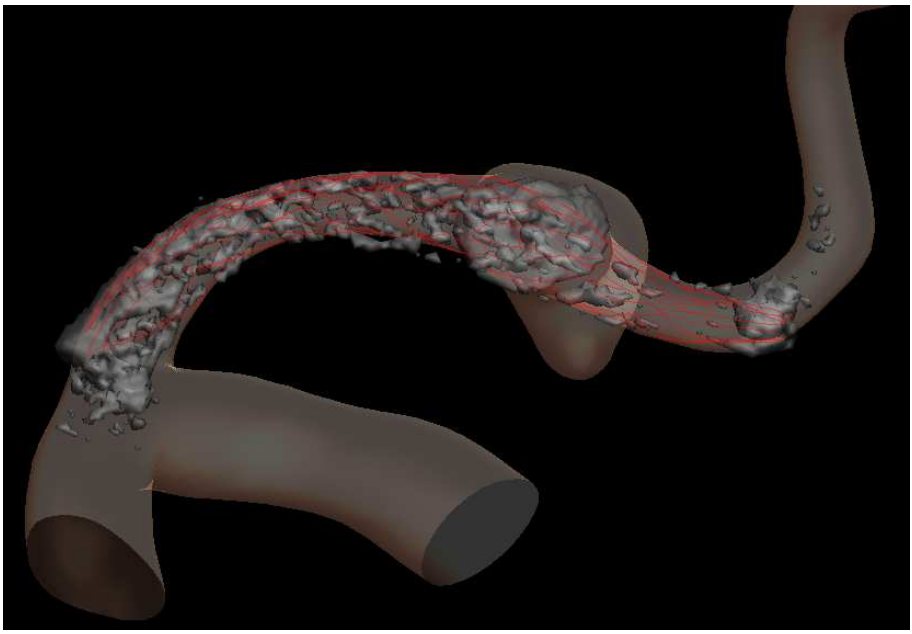

Figure 7.8: *In vivo* validation of the stent deployment. Superposition of the segmented post-procedural device (gray) and the deployed beam model of the numerical simulation (red).

Other groups have proposed geometrical methods for self-expandable stent implantation with different levels of complexity [105, 302, 339], which also seem to achieve good agreement with *in vitro* models in optimal conditions [216].

While these strategies are faster, and might give a possible successful outcome of the procedure, they neglect the lack of conformability of the stent and frequent incomplete apposition described *in vivo* due to hugging and ovalization of the stent[218,320,321]. However, this limitation might be confined to the closed cell device which experiences this collateral effect, and may be less relevant for open cell stents [299,321].

To the best of our knowledge, the results presented in this study is the first attempt for an *in vivo* validation of virtual cerebral aneurysm stenting.

Particular attention has been paid to the delivery technique which was validated with previous *in vitro* data [218] to ensure the inclusion of potentially undesired effects experienced in real endovascular procedures. The FE method shows a good agreement with the experimental results, capturing the hugging of the inner curvature leading to large malapposed

areas, which has been described to occur *in vivo* using the Enterprise stent [320,321,333].

Follow-up has traditionally focused on the presence or absence of residual filling in the dome [333,340]. Though ISA seems to be an underestimated key factor leading to procedural failure. In fact, neointimal growth over the stent struts to embed the device into the artery is a response to endothelial injury from the device [341,342]. The lack of apposition due to ovalization of the stent may prevent neointimal coverage of the treated segment and the exposure of the stent to the blood circulation can promote thrombosis and thromboembolism which have been related to ischemic events [219,303,304]. A reliable tool to assess ISA, as the presented environment, to quantify ISA in a pre-operative setup might, then, have an impact in the clinical community.

When comparing the simulated deployment with the *in vitro* outcome a small mismatch in the proximal segment of the device is present, exhibiting smaller ISA than in the *in vitro* model. This can depend on a number of factors, but it might be possible that the position of the guidewire over which the stent slides, can also play a role in the underexpansion of the device in the simulations. A guidewire positioned along the centerline of the vessel can promote a more uniform expansion of the stent, which is an idealization of the more complex reality.

Additionally, we tried to answer unsolved questions addressed by the authors of the *in vitro* experiment [218] by analyzing the effect of a different length of the device in the same model. The 28 mm stent shows a larger zone of incomplete apposition compared to the shorter design. From this result it is clear that the push-back technique operates on the closed stent by dragging the stent proximally. Once the distal portion of the stent is anchored to the vessel, the friction between the micro-catheter and the stent stretches the device during the retraction due to the fully connected mesh of the stent. The longer device of course offers more contact surface amplifying the dragging consequences experiencing higher ISA. This is a possible explanation why hugging is not reported for open cell designs such as the Neuroform which structure is less connected offering less dragging during pulling [299,320,321]. We speculate that reduction of the friction of the micro-catheter can help solving this drawback for the closed cell device.

Good agreement of the validated delivery technique is also shown when the strategy migrates to the patient-specific setup. The FE method captures the global configuration of the deployed device and the final shape of the stented artery. The difference in the tortuosity values also

provides a (weak) quantitative validation of the numerical outcome. As previously reported [299,343] the Enterprise stent has low conformability and forces the vessel to straighten as confirmed by the reduction in the tortuosity parameter. A visual inspection of the causes of the straightening highlights that the distal segment of the stent ends in region of the vessel with low curvature angles. Due to the force exerted by the stent, the bend is straightened and the more peripheral region of the vessel is translated outward.

A detailed quantitative comparison was not possible due the device-induced artifacts in the post-operative images. An example of the impact of these artifacts is the observation that after the segmentation the proximal part of the vessel displays a smaller diameter in the non-stented region due to the scattering induced by the coil's mass (Figure 7.7). This prevented a luminal analysis of the post procedural outcomes. Also the attenuation of the stent increases the actual size of the struts, hindering a comparison of the apposition as performed in our previous study [250]

Still lacking extensive validation on multiple cases, the present study does show the feasibility of pre-operative assessment of the deployed device. The method can be applied in a clinical setting and can provide knowledge on the occurrence of undesired effects. The method allows to inspect neck coverage and stented vessel shape to assess aneurysm catheterization [344], evaluate stent size and positioning to reduce straightening of the artery, evaluate hugging and the location of ISA which may prevent neointimal coverage of the treated segment [341,342], and thus promoting thromboembolic-related ischemic events [219,303,304] or induce late stent migration [345].

7.3.1 Limitations

Limitations of this study are mostly associated to the *in vivo* data especially from the post-operative condition: streak artifacts caused by the radio-dense stent markers and by the coil mass harboring portions of the stent, relatively low resolution compared to the stent strut dimensions, configuration changes caused by the hemodynamic variations and boundaries non-triggered acquisitions.

Another limitation of this study might arise from the specific case geometry. The curvature angle of the vessel is not sufficient to induce significant ISA [320]. It has been speculated that the Enterprise stent may not be able to completely appose the vessel wall beyond a certain level of tight curvature [218]. Nevertheless, the experimental validation

makes us confident of the applicability of the procedure to more angulated cases.

Also, as shown in this study and in the previous *in vitro* experiments [218] the delivery technique influences the deployed configuration. This adds operator dependency to the uncertainties of the outcome.

Furthermore, modeling simplifications have been applied (single layered vessel model, constant thickness of the wall, no pre-stressing or pre-stretching of the vessel, isotropy of the artery, non complete material device description, lack of influence of the surrounding tissues) which might affect the outcome of the numerical model. Nevertheless, the detail achieved by the numerical outcome seems sufficient to catch the main features of the implanted device. In the authors opinion, a balance is needed between desired accuracy of the results and cost in terms of modeling complexity and computational efficiency. In the perspective of moving numerical simulations to a clinical environment as a pre-assessment tool for procedure planning, speed and ease of model preprocessing, short simulation times and ease of result interpretation are required.

Five

Conclusions

CHAPTER 8

Final remarks

In this chapter, the conclusions of this thesis are presented. Improvements of the numerical methodologies realized within the scope of this PhD thesis and the main results are summarized. Finally unsolved issues of this research are discussed and suggestions for further investigations are proposed.

8.1 Study conclusions

At the beginning of this project, only few biomechanical studies had investigated the endovascular procedure for stroke prevention. Existing studies were focusing on simple parametric models, *in vitro* models and rarely on patient-specific conditions. This thesis continues previous PhD-work on the biomechanical aspects of the interventional stenting procedure performed at our department [346–348] aiming to investigate stent devices and their interaction with the arterial wall for stenotic carotid and aneurysmatic cerebral arteries. A patient-specific setup presents challenges in the modeling of the complex structures of pathological arteries, in the simulation of realistic and computationally efficient approximations of the delivery procedure as well as post-processing techniques for validation of the results.

The introductory chapters give a short overview of the current clinical strategies for stroke prevention, major causes of the pathology and the

existing literature on computational biomechanics studies investigating initiation, progression and treatment of the disease.

8.1.1 Challenges in biomechanical modeling of endovascular treatment modeling

The technological mechanical process for stent creation may result in complex geometrical patterns of the device mesh. A first step for accurate procedural emulation is the reconstruction of realistic stent geometries. Chapter 3 starts by detailing the strategies to build the numerical models of the devices from μCT scans of the samples or other sources using a library of predefined structures. These are then assembled to obtain the numerical device model. Further the specific methodologies developed for accurate vessel modeling are presented. First the construction of a very accurate parametric bifurcated vessel model is described. The model includes high detail of the wall structures and special meshing strategies ensure increased element density at the region of interest. Next, patient-specific vessel reconstruction and meshing is presented. The outer and inner wall surfaces are meshed with quadrilateral elements, connected and refined to create the diseased artery model. Elements laying in the STLs of the plaque geometries are selected to represent the diseased vessel regions.

Finally two insertion strategies are described. A simplified method has been developed and implemented which smoothly bends the delivery catheter along the centerline of the vessel and places the device by a gradual opening of the catheter. Furthermore, a more realistic insertion method has been implemented which simulates the pushing of the stent on the guidewire and retraction of the catheter. The advantage of each strategy is discussed.

8.1.2 Carotid artery stenting

Parametric and simplified vessel geometries are relatively fast to generate allow for an easy comparison and evaluation of different procedural solutions. This is impossible to assess *in vivo*. However, to ensure reliability of parametric models an adequate level of complexity is needed to reflect a realistic vascular morphology. Chapter 4 details the deployment of an Acculink stent in five possible lesion scenarios simulated by changing both material properties (to switch from vulnerable to stable plaques) and vascular geometrical features of an accurate carotid model which included a damage model to quantify the injury of the vessel. The results were analyzed with respect to lumen gain and wall stresses,

both parameters potentially related to failure of the procedure in the clinical setting. Results show that an elliptic lumen shape and a thinner fibrous cap with an underlying lipid pool exhibit higher stenosis reduction, while large calcifications and fibrotic tissue are more prone to recoil. The shielding effect of a thicker fibrous cap helps to reduce local compressive stresses in the soft plaque. The presence of a soft plaque reduces the damage in the healthy vascular structures. Contrarily, the presence of hard plaques is favorable in terms of less damaged volume in the fibrous cap and reduces stress peaks in this region, but they seem to increase stresses in the media-intima layer. Finally the reliability of the achieved results is put into clinical perspective.

Though *in silico* models provide a useful comparative environment, validation with *in vivo* data is needed to assess the numerical outcome. In chapter 5, two patient who underwent CAS with two different sizes of the Acculink stent were studied. Pre-operative data were used to build the numerical vessel models with heterogeneous material properties. Numerical results were validated with post-operative angiography. Incomplete stent apposition, free cell area and largest fitting sphere in the stent cell were evaluated in situ as potential risk factors for CAS complications. The simulations compare well with the post-operative angiographic data both qualitatively and quantitatively. The measurements of the scaffolding parameters on the virtually deployed stents highlight the variability of device behaviors in relation with the target lesion.

8.1.3 Cerebral aneurysm endovascular reconstruction

The deployment technique is further applied in a different vascular district for the treatment of cerebral aneurysm. There is an open debate among clinicians on the superiority of closed versus open cell stents. To gain insights on the influence of stent design in stent assisted coiling a FE environment was devised. In chapter 6 three stent designs (an open cell stent resembling the Neuroform, a generic stiff and a more flexible closed cell design), were deployed in three patient-specific cerebral aneurysmatic vessels. Outcomes of all procedures were investigated with respect to the percentage of strut area covering the aneurysm neck, the straightening induced on the cerebrovasculature, and stent apposition to the wall. The results suggest that the open cell design better covers the aneurysm neck compared to closed cell stents, and induces less straightening of the vessel. This, however, comes at cost of a large incomplete apposition to vessel wall.

In the perspective of a clinical use of a FE model for cerebral stenting as pre-operative tool, *in vivo* comparison is needed to assess the reliability of the outcome. Chapter 7 provides a validation of the virtual set up with one patient specific case study treated with an Enterprise stent. As the delivery technique influences the deployed configuration, *in vitro* experiments are firstly used to validate the FE simulation of the push-back insertion. Further the virtual procedure is performed on the CT-based vessel numerical model. Post-operative CT scans were compared with the numerical results with good agreement of the global stent configuration, and changes in vessel shape. Vessel straightening is also quantitative similar in both the real and simulated case showing the capability of the method to reproduce realistic deformations.

To summarize, the main achievements of the research activities described in this dissertation are:

1. the development and implementation of efficient techniques for preprocessing of the virtual endovascular procedure, both for mesh creation of stents and accurate vessel models, and device deployment;

2. the development of accurate parametric vessel models to study the effect of the stent design on different pathological morphologies;

3. *in vivo* validation of realistic simulation strategies to study patients specific CAS with an advanced post-processing environment to evaluate clinical outcome;

4. new insights on the effect of different stent designs in aneurysmatic cerebral vessels and their dependency on the variability and complexity of patient-specific vasculature;

5. *in vivo* validation of the deployment strategy for stent supported coiling emulating push-back catheter retrieval technique.

Differently from previous work [346–348] in the field, which was focused on fundamental research and comparison of different stents, this research was mainly focused on the application of accurate simulation strategies in realistic anatomical models. Furthermore, a more clinical evaluation has been performed to extract information from the simulations (potentially) useful for a clinical community. The validation process has intrinsic difficulties due to the manipulation of *in vivo* data which require a superior effort in terms of pre- and post-processing. Further validation is, however, a mandatory step to transfer finite element strategies in a medical setting for procedure planning.

8.2 Future perspectives

Results achieved and methodologies proposed in this dissertation can pave the way for further investigation in accurate modeling of endovascular treatment for stroke prevention.

A patient-specific numerical procedure for clinical routine needs not only be reliable and fast compared to procedure planning times, but should also be easily analyzed by the operator to retrieve the needed parameter under investigation.

Instead of developing novel strategies for vessel meshing, the proposed method based on validated and available (open source) meshing tools can be improved by automatically creating the multi-block structure to limit user interaction on the procedure. Modified oriented bounding box methods could be implemented to create connected structures following the centerline of the vessel. The stent meshing tool could be included in a user friendly environment for automated selection of the control points of the basic structures.

Accurate modeling of the stent will also require mechanical testing of the device samples using flat plate and/or radial compression tests for a correct description of the nitinol material coefficients.

On the other hand a systematic investigation should be performed on the validated vessel models, to analyze the dependency of the outcome on specific parameters, and study which simplifications can be adopted without loss of accuracy of the simulation. Material properties should be better investigated (isotropic vs anisotropic material), inclusion of plasticity of the vessel which becomes relevant in balloon angioplasty/stenting, effect of pre-stress due to vessel pressurization and pre-stretch. This could lead to better understanding of the real configuration of the vessel geometry, initial stress and stretch levels. It might be speculated that as the combined effect of all these parameters moves the vessel stress-strain curve in a region with stiffer behavior, a linear approximation could be actually less critical for the description of the vessel behavior in *in vivo* conditions.

The validated deployment method should be extended to study cohorts of stented patients, in order to retrieve average material properties of the vessel to be used as reference for virtual endovascular treatment.

In addition cases with device-related complications should be included to establish the influence of specific mechanical parameters and device characteristics on the endovascular outcome. This, however, implies that a more realistic balloon angioplastic intervention should be implemented by using realistic or engineering equivalent methods.

Long term results of the interventional treatment could help to relate failure due to restenosis, stent fracture or stent migration and thus to some extent to stent design. The *in vivo* cyclic condition should be studied for fatigue rupture (inexpensively through computational analysis) and should be used to calculate a factor of safety for the implanted geometry being imposed to the pulsatile blood conditions.

Finally the validated model(s) could be used to better compare *in vivo* effects of different stent designs.

Bibliography

[1] H. Gray, *Anatomy of the human body*. Lea & Febiger, 1918.

[2] G. A. Holzapfel, T. C. Gasser, and R. W. Ogden, "A new constitutive framework for arterial wall mechanics and a comparative study of material models," *Journal of elasticity and the physical science of solids*, vol. 61, no. 1-3, pp. 1–48, 2000.

[3] S. J. George and J. Johnson, *Atherosclerosis: molecular and cellular mechanisms*. John Wiley & Sons, 2010.

[4] H. C. Stary, A. B. Chandler, S. Glagov, J. R. Guyton, W. Insull, M. E. Rosenfeld, S. A. Schaffer, C. J. Schwartz, W. D. Wagner, and R. W. Wissler, "A definition of initial, fatty streak, and intermediate lesions of atherosclerosis. a report from the committee on vascular lesions of the council on arteriosclerosis, american heart association.," *Arteriosclerosis, Thrombosis, and Vascular Biology*, vol. 14, no. 5, pp. 840–856, 1994.

[5] H. C. Stary, A. B. Chandler, R. E. Dinsmore, V. Fuster, S. Glagov, W. Insull, M. E. Rosenfeld, C. J. Schwartz, W. D. Wagner, and R. W. Wissler, "A definition of advanced types of atherosclerotic lesions and a histological classification of atherosclerosis a report from the committee on vascular lesions of the council on arteriosclerosis, american heart association," *Arteriosclerosis, thrombosis, and vascular biology*, vol. 15, no. 9, pp. 1512–1531, 1995.

[6] H. C. Stary, "Natural history and histological classification of atherosclerotic lesions an update," *Arteriosclerosis, thrombosis, and vascular biology*, vol. 20, no. 5, pp. 1177–1178, 2000.

[7] J.-M. Cai, T. S. Hatsukami, M. S. Ferguson, R. Small, N. L. Polissar, and C. Yuan, "Classification of human carotid atherosclerotic lesions with in vivo multicontrast magnetic resonance imaging," *Circulation*, vol. 106, no. 11, pp. 1368–1373, 2002.

[8] D. M. Sforza, C. M. Putman, and J. R. Cebral, "Hemodynamics of cerebral aneurysms," *Annual review of fluid mechanics*, vol. 41, p. 91, 2009.

[9] P. M. Rothwell, R. J. Gibson, J. Slattery, R. J. Sellar, and C. P. Warlow, "Equivalence of measurements of carotid stenosis. a comparison of three methods on 1001 angiograms. european carotid surgery trialists' collaborative group.," *Stroke*, vol. 25, no. 12, pp. 2435–2439, 1994.

[10] T. G. Brott, J. L. Halperin, S. Abbara, J. M. Bacharach, J. D. Barr, R. L. Bush, C. U. Cates, M. A. Creager, S. B. Fowler, G. Friday, *et al.*, "2011 asa/accf/aha/aann/aans/acr/asnr/cns/saip/scai/sir/snis/svm/svs guideline on the management of patients with extracranial carotid and vertebral artery diseasea report of the american college of cardiology foundation/american heart association task force on practice guidelines, and the american stroke association, american association of neuroscience nurses, american association of neurological surgeons, american college of radiology, american society of neuroradiology, congress of neurological surgeons, society of atherosclerosis imaging and prevention, society for cardiovascular angiography and interventions, society of interventional radiology, society of neurointerventional surgery, society for vascular medicine, and society for vascular surgery developed in collaboration with the american academy of neurology and society of cardiovascular computed tomography," *Journal of the American College of Cardiology*, vol. 57, no. 8, pp. e16–e94, 2011.

[11] W. S. Moore, *Vascular and Endovascular Surgery: A Comprehensive Review*. Elsevier Health Sciences, 2012.

[12] G. Lanzino, A. A. Rabinstein, and R. D. Brown Jr, "Treatment of carotid artery stenosis: medical therapy, surgery, or stenting?," in *Mayo Clinic Proceedings*, vol. 84, pp. 362–368, Elsevier, 2009.

[13] S. Macdonald and G. Stansby, *Practical Carotid Artery Stenting*. Springer, 2009.

[14] J. L. Brisman, J. K. Song, and D. W. Newell, "Cerebral aneurysms," *New England Journal of Medicine*, vol. 355, no. 9, pp. 928–939, 2006.

[15] M. Pearl, L. Gregg, and P. Gailloud, "Endovascular treatment of aneurysmal subarachnoid hemorrhage," *Neurosurgery clinics of North America*, vol. 21, no. 2, pp. 271–280, 2010.

[16] A. J. Molyneux, R. S. C. Kerr, L.-M. Yu, M. Clarke, M. Sneade, J. A. Yarnold, and P. Sandercock, "International subarachnoid aneurysm trial (ISAT) of neurosurgical clipping versus endovascular coiling in 2143 patients with ruptured intracranial aneurysms: a randomised comparison of effects on survival, dependency, seizures, rebleeding, subgroups, and aneurysm occlusion," *Lancet*, vol. 366, pp. 809–817, Sept. 2005.

[17] R. J. Komotar, J. Mocco, and R. A. Solomon, "Guidelines for the surgical treatment of unruptured intracranial aneurysms: the first annual j. lawrence pool memorial research symposium-controversies in the management of cerebral aneurysms," *Neurosurgery*, vol. 62, no. 1, pp. 183–194, 2008.

[18] L. N. Williams and R. D. Brown, "Management of unruptured intracranial aneurysms," *Neurology: Clinical Practice*, vol. 3, no. 2, pp. 99–108, 2013.

[19] J. E. Loewenstein, S. C. Gayle, E. J. Duffis, C. J. Prestigiacomo, and C. D. Gandhi, "The natural history and treatment options for unruptured intracranial aneurysms," *International journal of vascular medicine*, vol. 2012, 2012.

[20] E. S. Connolly, A. A. Rabinstein, J. R. Carhuapoma, C. P. Derdeyn, J. Dion, R. T. Higashida, B. L. Hoh, C. J. Kirkness, A. M. Naidech, C. S. Ogilvy, *et al.*, "Guidelines for the management of aneurysmal subarachnoid hemorrhage a guideline for healthcare professionals from the american heart association/american stroke association," *Stroke*, vol. 43, no. 6, pp. 1711–1737, 2012.

[21] F. Iannaccone, M. De Beule, B. Verhegghe, and P. Segers, "Computer simulations in stroke prevention: Design tools and virtual strategies towards procedure planning," *Cardiovascular Engineering and Technology*, vol. 4, no. 4, pp. 291–308, 2013.

[22] C. D. Mathers, T. Boerma, and D. M. Fat, "Global and regional causes of death," *British Medical Bulletin*, vol. 92, no. 1, pp. 7–32, 2009.

[23] National Heart, Lung, and Blood Institute and others, "Incidence and prevalence: 2006 chart book on cardiovascular and lung diseases," *Bethesda, MD: National Institutes of Health*, 2006.

[24] V. L. Roger, A. S. Go, D. M. Lloyd-Jones, E. J. Benjamin, J. D. Berry, W. B. Borden, D. M. Bravata, S. Dai, E. S. Ford, C. S. Fox, H. J. Fullerton, C. Gillespie, S. M. Hailpern, J. A. Heit, V. J. Howard, B. M. Kissela, S. J. Kittner, D. T. Lackland, J. H. Lichtman, L. D. Lisabeth, D. M. Makuc, G. M. Marcus, A. Marelli, D. B. Matchar, C. S. Moy, D. Mozaffarian, M. E. Mussolino, G. Nichol, N. P. Paynter, E. Z. Soliman, P. D. Sorlie, N. Sotoodehnia, T. N. Turan, S. S. Virani, N. D. Wong, D. Woo, and M. B. Turner, "Heart disease and stroke statistics—2012 update a report from the american heart association," *Circulation*, vol. 125, pp. e2–e220, Jan. 2012.

[25] G. W. Albers, P. Amarenco, J. D. Easton, R. L. Sacco, and P. Teal, "Antithrombotic and thrombolytic therapy for ischemic stroke the seventh ACCP conference on antithrombotic and thrombolytic therapy," *CHEST Journal*, vol. 126, no. 3_suppl, pp. 483S–512S, 2004.

[26] G. S. Silva, W. J. Koroshetz, R. G. González, and L. H. Schwamm, "Causes of ischemic stroke," *Acute Ischemic Stroke*, pp. 25–42, 2011.

[27] R. L. Sacco, R. Adams, G. Albers, M. J. Alberts, O. Benavente, K. Furie, L. B. Goldstein, P. Gorelick, J. Halperin, R. Harbaugh, S. C. Johnston, I. Katzan, M. Kelly-Hayes, E. J. Kenton, M. Marks, L. H. Schwamm, and T. Tomsick, "Guidelines for prevention of stroke in patients with ischemic stroke or transient ischemic attack a statement for healthcare professionals from the american heart Association/American stroke association council on stroke: Co-sponsored by the council on cardiovascular radiology and intervention: The american academy of neurology affirms the value of this guideline.," *Stroke*, vol. 37, pp. 577–617, Feb. 2006.

[28] L. B. Goldstein, R. Adams, M. J. Alberts, L. J. Appel, L. M. Brass, C. D. Bushnell, A. Culebras, T. J. DeGraba, P. B. Gorelick, J. R. Guyton, R. G. Hart, G. Howard, M. Kelly-Hayes, J. V. I. Nixon, and R. L. Sacco, "Primary prevention of ischemic stroke a guideline from the american heart Association/American stroke association

stroke council: Cosponsored by the atherosclerotic peripheral vascular disease interdisciplinary working group; cardiovascular nursing council; clinical cardiology council; nutrition, physical activity, and metabolism council; and the quality of care and outcomes research interdisciplinary working group: The american academy of neurology affirms the value of this guideline.," *Stroke*, vol. 37, pp. 1583–1633, June 2006.

[29] R. G. Nogueira, H. L. Lutsep, R. Gupta, T. G. Jovin, G. W. Albers, G. A. Walker, D. S. Liebeskind, and W. S. Smith, "Trevo versus merci retrievers for thrombectomy revascularisation of large vessel occlusions in acute ischaemic stroke (trevo 2): a randomised trial," *The Lancet*, 2012.

[30] J. L. Saver, R. Jahan, E. I. Levy, T. G. Jovin, B. Baxter, R. G. Nogueira, W. Clark, R. Budzik, and O. O. Zaidat, "Solitaire flow restoration device versus the merci retriever in patients with acute ischaemic stroke (swift): a randomised, parallel-group, non-inferiority trial," *The Lancet*, 2012.

[31] M. P. Marks, M. L. Marcellus, H. M. Do, P. K. Schraedley-Desmond, G. K. Steinberg, D. C. Tong, and G. W. Albers, "Intracranial angioplasty without stenting for symptomatic atherosclerotic stenosis: Long-term follow-up," *AJNR Am J Neuroradiol*, vol. 26, pp. 525–530, Mar. 2005.

[32] R. d. M. d. Rochemont, B. Turowski, M. Buchkremer, M. Sitzer, F. E. Zanella, and J. Berkefeld, "Recurrent symptomatic high-grade intracranial stenoses: Safety and efficacy of undersized stents— initial experience1," *Radiology*, vol. 231, pp. 45–49, Apr. 2004.

[33] H. D. Chastain, M. S. Campbell, S. Iyer, G. S. Roubin, J. Vitek, A. Mathur, N. A. Al-Mubarak, J. B. Terry, V. Yates, and K. Kretzer, "Extracranial vertebral artery stent placement: in-hospital and follow-up results," *Journal of neurosurgery*, vol. 91, no. 4, pp. 547–552, 1999.

[34] North American Symptomatic Carotid Endarterectomy Trial Collaborators and others, "Beneficial effect of carotid endarterectomy in symptomatic patients with highgrade carotid stenosis," *N engl j Med*, vol. 325, pp. 445–453, 1991.

[35] C. Warlow, "Mrc european carotid surgery trial: interim results for symptomatic patients with severe (70-99%) or with mild (0-29%) carotid stenosis," *The Lancet*, vol. 337, no. 8752, pp. 1235–1243, 1991.

[36] P. M. Rothwell and L. B. Goldstein, "Carotid endarterectomy for asymptomatic carotid stenosis asymptomatic carotid surgery trial," *Stroke*, vol. 35, pp. 2425–2427, Oct. 2004.

[37] T. G. Brott, R. W. Hobson, G. Howard, G. S. Roubin, W. M. Clark, W. Brooks, A. Mackey, M. D. Hill, P. P. Leimgruber, A. J. Sheffet, V. J. Howard, W. S. Moore, J. H. Voeks, L. N. Hopkins, D. E. Cutlip, D. J. Cohen, J. J. Popma, R. D. Ferguson, S. N. Cohen, J. L. Blackshear, F. L. Silver, J. Mohr, B. K. Lal, and J. F. Meschia, "Stenting versus endarterectomy for treatment of carotid-artery stenosis," *New England Journal of Medicine*, vol. 363, no. 1, pp. 11–23, 2010.

[38] H. S. Gurm, J. S. Yadav, P. Fayad, B. T. Katzen, G. J. Mishkel, T. K. Bajwa, G. Ansel, N. E. Strickman, H. Wang, S. A. Cohen, J. M. Massaro, and D. E. Cutlip, "Long-term results of carotid stenting versus endarterectomy in high-risk patients," *New England Journal of Medicine*, vol. 358, no. 15, pp. 1572–1579, 2008.

[39] S. Bash, J. P. Villablanca, R. Jahan, G. Duckwiler, M. Tillis, C. Kidwell, J. Saver, and J. Sayre, "Intracranial vascular stenosis and occlusive disease: Evaluation with CT angiography, MR angiography, and digital subtraction angiography," *AJNR Am J Neuroradiol*, vol. 26, pp. 1012–1021, May 2005.

[40] D. A. Steinman, "Image-based computational fluid dynamics modeling in realistic arterial geometries," *Ann Biomed Eng*, vol. 30, pp. 483–497, Apr. 2002.

[41] T. Saam, H. R. Underhill, B. Chu, N. Takaya, J. Cai, N. L. Polissar, C. Yuan, and T. S. Hatsukami, "Prevalence of american heart association type VI carotid atherosclerotic lesions identified by magnetic resonance imaging for different levels of stenosis as measured by duplex ultrasound," *J. Am. Coll. Cardiol.*, vol. 51, pp. 1014–1021, Mar. 2008.

[42] G. M. Biasi, A. Froio, E. B. Diethrich, G. Deleo, S. Galimberti, P. Mingazzini, A. N. Nicolaides, M. Griffin, D. Raithel, D. B. Reid, *et al.*, "Carotid plaque echolucency increases the risk of stroke in carotid stenting the imaging in carotid angioplasty and risk of stroke (icaros) study," *Circulation*, vol. 110, no. 6, pp. 756–762, 2004.

[43] M.-L. M. Grønholdt, B. G. Nordestgaard, T. V. Schroeder, S. Vorstrup, and H. Sillesen, "Ultrasonic echolucent carotid plaques predict future strokes," *Circulation*, vol. 104, pp. 68–73, July 2001.

[44] M. Reiter, I. Effenberger, S. Sabeti, W. Mlekusch, O. Schlager, P. Dick, S. Puchner, J. Amighi, R. A. Bucek, E. Minar, and M. Schillinger, "Increasing carotid plaque echolucency is predictive of cardiovascular events in high-risk patients1," *Radiology*, vol. 248, pp. 1050–1055, Sept. 2008.

[45] T. J. Tegos, M. M. Sabetai, A. N. Nicolaides, P. Robless, E. Kalodiki, T. S. Elatrozy, G. Ramaswami, and S. Dhanjil, "Correlates of embolic events detected by means of transcranial doppler in patients with carotid atheroma," *Journal of Vascular Surgery*, vol. 33, pp. 131–138, Jan. 2001.

[46] M. Wintermark, S. S. Jawadi, J. H. Rapp, T. Tihan, E. Tong, D. V. Glidden, S. Abedin, S. Schaeffer, G. Acevedo-Bolton, B. Boudignon, B. Orwoll, X. Pan, and D. Saloner, "High-resolution CT imaging of carotid artery atherosclerotic plaques," *AJNR Am J Neuroradiol*, vol. 29, pp. 875–882, May 2008.

[47] K. Haraguchi, K. Houkin, I. Koyanagi, T. Nonaka, and T. Baba, "Evaluation of carotid plaque composition by computed tomography angiography and black blood magnetic resonance image," *Interv Neuroradiol*, vol. 14, pp. 39–43, Mar. 2008.

[48] L. Saba, R. Sanfilippo, L. Pascalis, R. Montisci, G. Caddeo, and G. Mallarini, "Carotid artery wall thickness and ischemic symptoms: evaluation using multi-detector-row CT angiography," *European Radiology*, vol. 18, pp. 1962–1971, Apr. 2008.

[49] L. Saba, R. Sanfilippo, R. Montisci, and G. Mallarini, "Associations between carotid artery wall thickness and cardiovascular risk factors using multidetector CT," *AJNR Am J Neuroradiol*, vol. 31, pp. 1758–1763, Oct. 2010.

[50] C. Yuan, L. M. Mitsumori, K. W. Beach, and K. R. Maravilla, "Carotid atherosclerotic plaque: noninvasive MR characterization and identification of vulnerable lesions," *Radiology*, vol. 221, pp. 285–299, Nov. 2001.

[51] V. Mani, S. H. Aguiar, V. V. Itskovich, K. B. Weinshelbaum, J. E. Postley, E. J. Wasenda, J. G. S. Aguinaldo, D. D. Samber, and Z. A. Fayad, "Carotid black blood MRI burden of atherosclerotic disease assessment correlates with ultrasound intima-media thickness," *Journal of Cardiovascular Magnetic Resonance*, vol. 8, no. 3, pp. 529–534, 2006.

[52] L. Saba, R. Sanfilippo, R. Montisci, and G. Mallarini, "Carotid artery wall thickness: comparison between sonography and multidetector row CT angiography," *Neuroradiology*, vol. 52, pp. 75–82, Sept. 2009.

[53] I. F. Klein, P. C. Lavallée, P. J. Touboul, E. Schouman-Claeys, and P. Amarenco, "In vivo middle cerebral artery plaque imaging by high-resolution MRI," *Neurology*, vol. 67, pp. 327–329, July 2006.

[54] M.-l. Li, W.-h. Xu, L. Song, F. Feng, H. You, J. Ni, S. Gao, L.-y. Cui, and Z.-y. Jin, "Atherosclerosis of middle cerebral artery: evaluation with high-resolution mr imaging at 3t," *Atherosclerosis*, vol. 204, no. 2, pp. 447–452, 2009.

[55] C. A. Taylor and D. A. Steinman, "Image-based modeling of blood flow and vessel wall dynamics: Applications, methods and future directions," *Ann Biomed Eng*, vol. 38, pp. 1188–1203, Mar. 2010.

[56] P. J. Homburg, S. Rozie, M. J. van Gils, Q. J. A. van den Bouwhuijsen, W. J. Niessen, D. W. J. Dippel, and A. van der Lugt, "Association between carotid artery plaque ulceration and plaque composition evaluated with multidetector CT angiography," *Stroke*, vol. 42, pp. 367–372, Dec. 2010.

[57] B. Chu, M. S. Ferguson, H. Chen, D. S. Hippe, W. S. Kerwin, G. Canton, C. Yuan, and T. S. Hatsukami, "Cardiac magnetic resonance features of the disruption-prone and the disrupted carotid plaque," *JACC: Cardiovascular Imaging*, vol. 2, no. 7, pp. 883–896, 2009.

[58] N. Gonzalo, G. J. Tearney, P. W. Serruys, G. van Soest, T. Okamura, H. M. García-García, R. Jan van Geuns, M. van der Ent, J. Ligthart, B. E. Boum, *et al.*, "Second-generation optical coherence tomography in clinical practice. high-speed data acquisition is highly reproducible in patients undergoing percutaneous coronary intervention," *Revista Española de Cardiología (English Edition)*, vol. 63, no. 8, pp. 893–903, 2010.

[59] D. A. Steinman, C. R. Ethier, and B. K. Rutt, "Combined analysis of spatial and velocity displacement artifacts in phase contrast measurements of complex flows," *Journal of Magnetic Resonance Imaging*, vol. 7, no. 2, pp. 339–346, 1997.

[60] N. M. Maurits, G. E. Loots, and A. E. P. Veldman, "The influence of vessel wall elasticity and peripheral resistance on the carotid artery flow wave form: A CFD model compared to in vivo ultrasound measurements," *Journal of biomechanics*, vol. 40, no. 2, pp. 427–436, 2007.

[61] H. Hayase, K. Tokunaga, T. Nakayama, K. Sugiu, A. Nishida, S. Arimitsu, T. Hishikawa, S. Ono, M. Ohta, and I. Date, "Computational fluid dynamics of carotid arteries after carotid endarterectomy or carotid artery stenting based on postoperative patient-specific CT angiography and ultrasound flow data," *Neurosurgery*, p. 1, Jan. 2011.

[62] J. D. Gill, H. M. Ladak, D. A. Steinman, and A. Fenster, "Accuracy and variability assessment of a semiautomatic technique for segmentation of the carotid arteries from three-dimensional ultrasound images," *Med Phys*, vol. 27, pp. 1333–1342, June 2000.

[63] A. D. Augst, B. Ariff, S. A. G. McG Thom, X. Y. Xu, and A. D. Hughes, "Analysis of complex flow and the relationship between blood pressure, wall shear stress, and intima-media thickness in the human carotid artery," *Am. J. Physiol. Heart Circ. Physiol.*, vol. 293, pp. H1031–1037, Aug. 2007.

[64] J. J. Wentzel, F. J. Gijsen, N. Stergiopulos, P. W. Serruys, C. J. Slager, and R. Krams, "Shear stress, vascular remodeling and neointimal formation," *Journal of Biomechanics*, vol. 36, pp. 681–688, May 2003.

[65] Y. Fukumoto, H. Asai, M. Shimizu, and N. Chatani, "ChemInform abstract: anti-markovnikov addition of both primary and secondary amines to terminal alkynes catalyzed by the TpRh(C2H4)2/PPh3 system.," *ChemInform*, vol. 39, no. 13, p. no–no, 2008.

[66] H. S. Ryou, S. Kim, S. W. Kim, and S. W. Cho, "Construction of healthy arteries using computed tomography and virtual histology intravascular ultrasound," *Journal of Biomechanics*, vol. 45, pp. 1612–1618, June 2012.

[67] D. J. Clark, S. Lessio, M. O'Donoghue, R. Schainfeld, and K. Rosenfield, "Safety and utility of intravascular ultrasound-guided carotid artery stenting," *Catheterization and cardiovascular interventions*, vol. 63, no. 3, pp. 355–362, 2004.

[68] M. J. Vonesh, C. H. Cho, J. Pinto, J V, B. J. Kane, D. S. Lee, S. I. Roth, K. B. Chandran, and D. D. McPherson, "Regional vascular mechanical properties by 3-d intravascular ultrasound with finite-element analysis," *Am. J. Physiol.*, vol. 272, pp. H425–437, Jan. 1997.

[69] K. B. Chandran, J. H. Mun, K. K. Choi, J. S. Chen, A. Hamilton, A. Nagaraj, and D. D. McPherson, "A method for in-vivo analysis for regional arterial wall material property alterations with atherosclerosis: preliminary results," *Med Eng Phys*, vol. 25, pp. 289–298, May 2003.

[70] S. Z. Zhao, X. Y. Xu, A. D. Hughes, S. A. Thom, A. V. Stanton, B. Ariff, and Q. Long, "Blood flow and vessel mechanics in a physiologically realistic model of a human carotid arterial bifurcation," *J Biomech*, vol. 33, pp. 975–984, Aug. 2000.

[71] B. Reimers, D. Nikas, E. Stabile, L. Favero, S. Saccà, A. Cremonesi, and P. Rubino, "Preliminary experience with optical coherence tomography imaging to evaluate carotid artery stents: safety, feasibility and techniques," *EuroIntervention*, vol. 7, pp. 98–105, May 2011.

[72] C. Setacci, G. de Donato, F. Setacci, G. Galzerano, P. Sirignano, A. Cappelli, and G. Palasciano, "Safety and feasibility of intravascular optical coherence tomography using a nonocclusive technique to evaluate carotid plaques before and after stent deployment," *Journal of Endovascular Therapy*, vol. 19, pp. 303–311, June 2012.

[73] D. Lesage, E. D. Angelini, I. Bloch, and G. Funka-Lea, "A review of 3D vessel lumen segmentation techniques: Models, features and extraction schemes," *Medical Image Analysis*, vol. 13, pp. 819–845, Dec. 2009.

[74] C. Kirbas and F. Quek, "A review of vessel extraction techniques and algorithms," *ACM Comput. Surv.*, vol. 36, p. 81–121, June 2004.

[75] J. S. Suri, K. Liu, L. Reden, and S. Laxminarayan, "A review on MR vascular image processing algorithms: acquisition and prefiltering: part i.," *IEEE transactions on information technology in biomedicine: a publication of the IEEE Engineering in Medicine and Biology Society*, vol. 6, no. 4, p. 324, 2002.

[76] J. S. Suri, K. Liu, L. Reden, and S. Laxminarayan, "A review on MR vascular image processing: skeleton versus nonskeleton approaches: part II.," *IEEE transactions on information technology in biomedicine: a publication of the IEEE Engineering in Medicine and Biology Society*, vol. 6, no. 4, p. 338, 2002.

[77] P. Felkel and R. La Cruz, "Geometric methods for vessel visualization and quantification-a survey," 2004.

[78] P. Felkel and R. Wegenkittl, *Vessel Tracking in Peripheral CTA Datasets - An Overview*. 2001.

[79] K. Sun, "Development of segmentation methods for vascular angiogram," *IETE Technical Review*, vol. 28, no. 5, p. 392, 2011.

[80] K. Bühler, P. Felkel, and A. La Cruz, "Geometric methods for vessel visualization and quantification–a survey," in *In Geometric Modelling for Scientific Visualization*, Citeseer, 2002.

[81] I. M. Adame, R. J. van der Geest, B. A. Wasserman, M. A. Mohamed, J. H. C. Reiber, and B. P. F. Lelieveldt, "Automatic segmentation and plaque characterization in atherosclerotic carotid artery MR images," *Magnetic Resonance Materials in Physics, Biology and Medicine*, vol. 16, no. 5, pp. 227–234, 2004.

[82] D. Vukadinovic, S. Rozie, M. v. Gils, T. v. Walsum, R. Manniesing, A. v. d. Lugt, and W. J. Niessen, "Automated versus manual segmentation of atherosclerotic carotid plaque volume and components in CTA: associations with cardiovascular risk factors," *Int J Cardiovasc Imaging*, vol. 28, pp. 877–887, Apr. 2012.

[83] R. van 't Klooster, P. J. de Koning, R. A. Dehnavi, J. T. Tamsma, A. de Roos, J. H. Reiber, and R. J. van der Geest, "Automatic lumen and outer wall segmentation of the carotid artery using deformable three-dimensional models in MR angiography and vessel wall images," *Journal of Magnetic Resonance Imaging*, vol. 35, no. 1, p. 156–165, 2012.

[84] M. Grabe, *Grid Generation Methods*. Springer, 2010.

[85] S. J. Owen, "A survey of unstructured mesh generation technology.," in *IMR*, pp. 239–267, 1998.

[86] S. Prakash and C. R. Ethier, "Requirements for mesh resolution in 3D computational hemodynamics," *J Biomech Eng*, vol. 123, pp. 134–144, Apr. 2001.

[87] L. Antiga, B. Ene-Iordache, L. Caverni, G. Paolo Cornalba, and A. Remuzzi, "Geometric reconstruction for computational mesh generation of arterial bifurcations from CT angiography," *Computerized Medical Imaging and Graphics*, vol. 26, pp. 227–235, July 2002.

[88] Q. Long, X. Xu, M. Collins, M. Bourne, and T. Griffith, "Magnetic resonance image processing and structured grid generation of a human abdominal bifurcation," *Computer Methods and Programs in Biomedicine*, vol. 56, pp. 249–259, June 1998.

[89] G. De Santis, M. De Beule, P. Segers, P. Verdonck, and B. Verhegghe, "Patient-specific computational haemodynamics: generation of structured and conformal hexahedral meshes from triangulated surfaces of vascular bifurcations," *Computer Methods in Biomechanics and Biomedical Engineering*, vol. 14, pp. 797–802, Sept. 2011.

[90] G. De Santis, M. De Beule, K. Van Canneyt, P. Segers, P. Verdonck, and B. Verhegghe, "Full-hexahedral structured meshing for image-based computational vascular modeling," *Medical Engineering & Physics*, vol. 33, pp. 1318–1325, Dec. 2011.

[91] L. Antiga, B. Ene-Iordache, and A. Remuzzi, "Computational geometry for patient-specific reconstruction and meshing of blood vessels from MR and CT angiography," *IEEE Transactions on Medical Imaging*, vol. 22, pp. 674 –684, May 2003.

[92] L. Botti, M. Piccinelli, B. Ene-Iordache, A. Remuzzi, and L. Antiga, "An adaptive mesh refinement solver for large-scale simulation of biological flows," *International Journal for Numerical Methods in Biomedical Engineering*, vol. 26, no. 1, pp. 86–100, 2010.

[93] O. Sahni, K. E. Jansen, C. A. Taylor, and M. S. Shephard, "Automated adaptive cardiovascular flow simulations," *Engineering with Computers*, vol. 25, no. 1, pp. 25–36, 2009.

[94] E. Wang, T. Nelson, and R. Rauch, "Back to elements-tetrahedra vs. hexahedra," in *2004 International ANSYS Conference Proceedings*, 2004.

[95] D. Tang, C. Yang, J. Zheng, P. K. Woodard, G. A. Sicard, J. E. Saffitz, and C. Yuan, "3D MRI-Based multicomponent FSI models for atherosclerotic plaques," *Annals of Biomedical Engineering*, vol. 32, pp. 947–960, July 2004.

[96] G. A. Holzapfel, M. Stadler, and C. A. J. Schulze-Bauer, "A layer-specific three-dimensional model for the simulation of balloon angioplasty using magnetic resonance imaging and mechanical testing," *Ann Biomed Eng*, vol. 30, pp. 753–767, June 2002.

[97] G. A. Holzapfel, M. Stadler, and T. C. Gasser, "Changes in the mechanical environment of stenotic arteries during interaction with stents: computational assessment of parametric stent designs," *J Biomech Eng*, vol. 127, pp. 166–180, Feb. 2005.

[98] A. Creane, E. Maher, S. Sultan, N. Hynes, D. J. Kelly, and C. Lally, "Finite element modelling of diseased carotid bifurcations generated from in vivo computerised tomographic angiography," *Computers in Biology and Medicine*, vol. 40, pp. 419–429, Apr. 2010.

[99] D. E. Kiousis, S. F. Rubinigg, M. Auer, and G. A. Holzapfel, "A methodology to analyze changes in lipid core and calcification onto fibrous cap vulnerability: the human atherosclerotic carotid bifurcation as an illustratory example," *J Biomech Eng*, vol. 131, p. 121002, Dec. 2009.

[100] M. De Beule, P. Mortier, S. G. Carlier, B. Verhegghe, R. Van Impe, and P. Verdonck, "Realistic finite element-based stent design: The impact of balloon folding," *Journal of Biomechanics*, vol. 41, no. 2, pp. 383–389, 2008.

[101] F. Migliavacca, L. Petrini, V. Montanari, I. Quagliana, F. Auricchio, and G. Dubini, "A predictive study of the mechanical behaviour of coronary stents by computer modelling," *Medical engineering & physics*, vol. 27, no. 1, pp. 13–18, 2005.

[102] P. Mortier, M. De Beule, S. G. Carlier, R. Van Impe, B. Verhegghe, and P. Verdonck, "Numerical study of the uniformity of balloon-expandable stent deployment," *J Biomech Eng*, vol. 130, p. 021018, Apr. 2008.

[103] D. Gastaldi, S. Morlacchi, R. Nichetti, C. Capelli, G. Dubini, L. Petrini, and F. Migliavacca, "Modelling of the provisional side-branch stenting approach for the treatment of atherosclerotic coronary bifurcations: effects of stent positioning," *Biomechanics and Modeling in Mechanobiology*, vol. 9, no. 5, pp. 551–561, 2010.

[104] P. Mortier, M. De Beule, D. Van Loo, B. Masschaele, P. Verdonck, and B. Verhegghe, "Automated generation of a finite element stent model," *Med Biol Eng Comput*, vol. 46, pp. 1169–1173, Nov. 2008.

[105] J. Cebral and R. Lohner, "Efficient simulation of blood flow past complex endovascular devices using an adaptive embedding technique," *IEEE Transactions on Medical Imaging*, vol. 24, pp. 468 –476, Apr. 2005.

[106] H. G. Morales, M. Kim, E. E. Vivas, M.-C. Villa-Uriol, I. Larrabide, T. Sola, L. Guimaraens, and A. F. Frangi, "How do coil configuration and packing density influence intra-aneurysmal hemodynamics?," *AJNR Am J Neuroradiol*, vol. 32, pp. 1935–1941, Nov. 2011.

[107] G. R. Stuhne and D. A. Steinman, "Finite-element modeling of the hemodynamics of stented aneurysms," *J Biomech Eng*, vol. 126, pp. 382–387, June 2004.

[108] S. Morlacchi, B. Keller, P. Arcangeli, M. Balzan, F. Migliavacca, G. Dubini, J. Gunn, N. Arnold, A. Narracott, D. Evans, and P. Lawford, "Hemodynamics and in-stent restenosis: Micro-CT images, histology, and computer simulations," *Annals of Biomedical Engineering*, vol. 39, pp. 2615–2626, July 2011.

[109] R. Löhner, J. R. Cebral, F. E. Camelli, S. Appanaboyina, J. D. Baum, E. L. Mestreau, and O. A. Soto, "Adaptive embedded and immersed unstructured grid techniques," *Computer Methods in Applied Mechanics and Engineering*, vol. 197, pp. 2173–2197, Apr. 2008.

[110] F. Auricchio, M. Conti, M. Ferraro, and A. Reali, "Evaluation of carotid stent scaffolding through patient-specific finite element analysis," *International Journal for Numerical Methods in Biomedical Engineering*, vol. 28, no. 10, pp. 1043–1055, 2012.

[111] E. Maher, A. Creane, C. Lally, and D. J. Kelly, "An anisotropic inelastic constitutive model to describe stress softening and permanent deformation in arterial tissue," *Journal of the Mechanical Behavior of Biomedical Materials*, vol. 12, pp. 9–19, Aug. 2012.

[112] G. Sommer, P. Regitnig, L. Költringer, and G. A. Holzapfel, "Biaxial mechanical properties of intact and layer-dissected human carotid arteries at physiological and supraphysiological loadings," *Am. J. Physiol. Heart Circ. Physiol.*, vol. 298, pp. H898–912, Mar. 2010.

[113] H. M. Loree, "Static circumferential tangential modulus of human atherosclerotic tissue," *Journal of Biomechanics*, vol. 27, no. 2, p. 195, 1994.

[114] S. Glagov, C. Zarins, D. P. Giddens, and D. N. Ku, "Hemodynamics and atherosclerosis. insights and perspectives gained from studies of human arteries," *Arch. Pathol. Lab. Med.*, vol. 112, pp. 1018–1031, Oct. 1988.

[115] D. N. Ku, D. P. Giddens, C. K. Zarins, and S. Glagov, "Pulsatile flow and atherosclerosis in the human carotid bifurcation. positive correlation between plaque location and low oscillating shear stress.," *Arterioscler Thromb Vasc Biol*, vol. 5, pp. 293–302, May 1985.

[116] C. K. Zarins, D. P. Giddens, B. K. Bharadvaj, V. S. Sottiurai, R. F. Mabon, and S. Glagov, "Carotid bifurcation atherosclerosis. quantitative correlation of plaque localization with flow velocity profiles and wall shear stress," *Circ. Res.*, vol. 53, pp. 502–514, Oct. 1983.

[117] J. S. Milner, J. A. Moore, B. K. Rutt, and D. A. Steinman, "Hemodynamics of human carotid artery bifurcations: Computational studies with models reconstructed from magnetic resonance imaging of normal subjects," *Journal of Vascular Surgery*, vol. 28, pp. 143–156, July 1998.

[118] Q. Long, X. Y. Xu, B. Ariff, S. A. Thom, A. D. Hughes, and A. V. Stanton, "Reconstruction of blood flow patterns in a human carotid bifurcation: A combined CFD and MRI study," *Journal of Magnetic Resonance Imaging*, vol. 11, no. 3, p. 299–311, 2000.

[119] D. A. Steinman, J. B. Thomas, H. M. Ladak, J. S. Milner, B. K. Rutt, and J. D. Spence, "Reconstruction of carotid bifurcation hemodynamics and wall thickness using computational fluid dynamics and MRI," *Magn Reson Med*, vol. 47, pp. 149–159, Jan. 2002.

[120] S.-W. Lee, L. Antiga, J. D. Spence, and D. A. Steinman, "Geometry of the carotid bifurcation predicts its exposure to disturbed flow," *Stroke*, vol. 39, pp. 2341–2347, Aug. 2008.

[121] S.-W. Lee, L. Antiga, and D. A. Steinman, "Correlations among indicators of disturbed flow at the normal carotid bifurcation," *J Biomech Eng*, vol. 131, p. 061013, June 2009.

[122] Q. Long, X. Xu, K. Ramnarine, and P. Hoskins, "Numerical investigation of physiologically realistic pulsatile flow through arterial stenosis," *Journal of Biomechanics*, vol. 34, pp. 1229–1242, Oct. 2001.

[123] D. Tang, C. Yang, S. Kobayashi, and D. N. Ku, "Effect of a lipid pool on Stress/Strain distributions in stenotic arteries: 3-d fluid-structure interactions (FSI) models," *Journal of Biomechanical Engineering*, vol. 126, no. 3, p. 363, 2004.

[124] D. Tang, C. Yang, S. Kobayashi, and D. N. Ku, "Steady flow and wall compression in stenotic arteries: A three-dimensional thick-wall model with Fluid–Wall interactions," *Journal of Biomechanical Engineering*, vol. 123, no. 6, p. 548, 2001.

[125] D. Tang, C. Yang, J. Zheng, P. K. Woodard, J. E. Saffitz, G. A. Sicard, T. K. Pilgram, and C. Yuan, "Quantifying effects of plaque

structure and material properties on stress distributions in human atherosclerotic plaques using 3D FSI models," *J Biomech Eng*, vol. 127, pp. 1185–1194, Dec. 2005.

[126] G. Soloperto, N. G. Keenan, M. N. Sheppard, J. Ohayon, N. B. Wood, D. J. Pennell, R. H. Mohiaddin, and X. Y. Xu, "Combined imaging, computational and histological analysis of a ruptured carotid plaque: A patient-specific analysis," *Artery Research*, vol. 4, pp. 59–65, June 2010.

[127] J. J. Wentzel, E. Janssen, J. Vos, J. C. H. Schuurbiers, R. Krams, P. W. Serruys, P. J. de Feyter, and C. J. Slager, "Extension of increased atherosclerotic wall thickness into high shear stress regions is associated with loss of compensatory remodeling," *Circulation*, vol. 108, pp. 17–23, July 2003.

[128] A. Harloff, "Carotid plaque hemodynamics," *Interventional Neurology*, vol. 1, no. 1, pp. 44–54, 2012.

[129] A. C. van der Wal and A. E. Becker, "Atherosclerotic plaque rupture–pathologic basis of plaque stability and instability," *Cardiovascular research*, vol. 41, no. 2, pp. 334–344, 1999.

[130] M. Naghavi, P. Libby, E. Falk, S. W. Casscells, S. Litovsky, J. Rumberger, J. J. Badimon, C. Stefanadis, P. Moreno, G. Pasterkamp, Z. Fayad, P. H. Stone, S. Waxman, P. Raggi, M. Madjid, A. Zarrabi, A. Burke, C. Yuan, P. J. Fitzgerald, D. S. Siscovick, C. L. d. Korte, M. Aikawa, K. E. J. Airaksinen, G. Assmann, C. R. Becker, J. H. Chesebro, A. Farb, Z. S. Galis, C. Jackson, I.-K. Jang, W. Koenig, R. A. Lodder, K. March, J. Demirovic, M. Navab, S. G. Priori, M. D. Rekhter, R. Bahr, S. M. Grundy, R. Mehran, A. Colombo, E. Boerwinkle, C. Ballantyne, W. Insull, R. S. Schwartz, R. Vogel, P. W. Serruys, G. K. Hansson, D. P. Faxon, S. Kaul, H. Drexler, P. Greenland, J. E. Muller, R. Virmani, P. M. Ridker, D. P. Zipes, P. K. Shah, and J. T. Willerson, "From vulnerable plaque to vulnerable patient a call for new definitions and risk assessment strategies: Part i," *Circulation*, vol. 108, pp. 1664–1672, Oct. 2003.

[131] H. C. Stary, A. B. Chandler, R. E. Dinsmore, V. Fuster, S. Glagov, W. Insull, M. E. Rosenfeld, C. J. Schwartz, W. D. Wagner, and R. W. Wissler, "A definition of advanced types of atherosclerotic

lesions and a histological classification of atherosclerosis a report from the committee on vascular lesions of the council on arteriosclerosis, american heart association," *Arterioscler Thromb Vasc Biol*, vol. 15, pp. 1512–1531, Sept. 1995.

[132] M. Fisher, A. Paganini-Hill, A. Martin, M. Cosgrove, J. F. Toole, H. J. M. Barnett, and J. Norris, "Carotid plaque pathology thrombosis, ulceration, and stroke pathogenesis," *Stroke*, vol. 36, pp. 253–257, Feb. 2005.

[133] S. Glagov, E. Weisenberg, C. K. Zarins, R. Stankunavicius, and G. J. Kolettis, "Compensatory enlargement of human atherosclerotic coronary arteries," *N. Engl. J. Med.*, vol. 316, pp. 1371–1375, May 1987.

[134] G. Pasterkamp and P. C. Smits, "Imaging of atherosclerosis. remodelling of coronary arteries," *J Cardiovasc Risk*, vol. 9, pp. 229–235, Oct. 2002.

[135] P. D. Richardson, "Biomechanics of plaque rupture: progress, problems, and new frontiers," *Ann Biomed Eng*, vol. 30, pp. 524–536, Apr. 2002.

[136] J. K. Lovett and P. M. Rothwell, "Site of carotid plaque ulceration in relation to direction of blood flow: An angiographic and pathological study," *Cerebrovascular Diseases*, vol. 16, no. 4, pp. 369–375, 2003.

[137] X.-Z. Huang, Z.-Y. Wang, X.-H. Dai, Yun-Zhang, and M. Zhang, "Velocity vector imaging of longitudinal mechanical properties of upstream and downstream shoulders and fibrous cap tops of human carotid atherosclerotic plaque," *Echocardiography*, Oct. 2012.

[138] H. C. Groen, F. J. H. Gijsen, A. v. d. Lugt, M. S. Ferguson, T. S. Hatsukami, A. F. W. v. d. Steen, C. Yuan, and J. J. Wentzel, "Plaque rupture in the carotid artery is localized at the high shear stress region a case report," *Stroke*, vol. 38, pp. 2379–2381, Aug. 2007.

[139] J. S. Stroud, S. A. Berger, and D. Saloner, "Numerical analysis of flow through a severely stenotic carotid artery bifurcation," *Journal of Biomechanical Engineering*, vol. 124, no. 1, p. 9, 2002.

[140] M. R. Kaazempur-Mofrad, A. G. Isasi, H. F. Younis, R. C. Chan, D. P. Hinton, G. Sukhova, G. M. LaMuraglia, R. T. Lee, and R. D. Kamm, "Characterization of the atherosclerotic carotid bifurcation using MRI, finite element modeling, and histology," *Annals of Biomedical Engineering*, vol. 32, pp. 932–946, July 2004.

[141] Z. Teng, G. Canton, C. Yuan, M. Ferguson, C. Yang, X. Huang, J. Zheng, P. K. Woodard, and D. Tang, "3D critical plaque wall stress is a better predictor of carotid plaque rupture sites than flow shear stress: An in vivo MRI-based 3D FSI study," *J Biomech Eng*, vol. 132, p. 031007, Mar. 2010.

[142] Z.-Y. Li, S. Howarth, R. A. Trivedi, *et al.*, "Stress analysis of carotid plaque rupture based on in vivo high resolution mri," *Journal of biomechanics*, vol. 39, no. 14, pp. 2611–2622, 2006.

[143] P. D. Richardson, M. Davies, and G. Born, "Influence of plaque configuration and stress distribution on fissuring of coronary atherosclerotic plaques," *The Lancet*, vol. 334, no. 8669, pp. 941–944, 1989.

[144] A. Versluis, A. J. Bank, and W. H. Douglas, "Fatigue and plaque rupture in myocardial infarction," *J Biomech*, vol. 39, no. 2, pp. 339–347, 2006.

[145] Z.-Y. Li, T. Tang, J. U-King-Im, M. Graves, M. Sutcliffe, and J. H. Gillard, "Assessment of carotid plaque vulnerability using structural and geometrical determinants," *Circ. J.*, vol. 72, pp. 1092–1099, July 2008.

[146] H. M. Loree, R. D. Kamm, R. G. Stringfellow, and R. T. Lee, "Effects of fibrous cap thickness on peak circumferential stress in model atherosclerotic vessels," *Circ. Res.*, vol. 71, pp. 850–858, Oct. 1992.

[147] Z.-Y. Li, S. P. S. Howarth, T. Tang, and J. H. Gillard, "How critical is fibrous cap thickness to carotid plaque stability? a flow-plaque interaction model," *Stroke*, vol. 37, pp. 1195–1199, May 2006.

[148] G. C. Cheng, H. M. Loree, R. D. Kamm, M. C. Fishbein, and R. T. Lee, "Distribution of circumferential stress in ruptured and stable atherosclerotic lesions. a structural analysis with histopathological correlation.," *Circulation*, vol. 87, pp. 1179–1187, Apr. 1993.

[149] H. Huang, R. Virmani, H. Younis, A. P. Burke, R. D. Kamm, and R. T. Lee, "The impact of calcification on the biomechanical stability of atherosclerotic plaques," *Circulation*, vol. 103, pp. 1051 –1056, Feb. 2001.

[150] D. Tang, C. Yang, H. Walker, S. Kobayashi, and D. N. Ku, "Simulating cyclic artery compression using a 3D unsteady model with fluid–structure interactions," *Computers & structures*, vol. 80, no. 20, pp. 1651–1665, 2002.

[151] Z.-Y. Li, S. P. S. Howarth, T. Tang, M. J. Graves, J. U-King-Im, R. A. Trivedi, P. J. Kirkpatrick, and J. H. Gillard, "Structural analysis and magnetic resonance imaging predict plaque vulnerability: a study comparing symptomatic and asymptomatic individuals," *J. Vasc. Surg.*, vol. 45, pp. 768–775, Apr. 2007.

[152] D. Tang, Z. Teng, G. Canton, C. Yang, M. Ferguson, X. Huang, J. Zheng, P. K. Woodard, and C. Yuan, "Sites of rupture in human atherosclerotic carotid plaques are associated with high structural stresses: an in vivo MRI-based 3D fluid-structure interaction study," *Stroke*, vol. 40, pp. 3258–3263, Oct. 2009.

[153] Z. Teng, U. Sadat, Y. Huang, V. E. Young, M. J. Graves, J. Lu, and J. H. Gillard, "In vivo MRI-based 3D mechanical stress-strain profiles of carotid plaques with juxtaluminal plaque haemorrhage: an exploratory study for the mechanism of subsequent cerebrovascular events," *Eur J Vasc Endovasc Surg*, vol. 42, pp. 427–433, Oct. 2011.

[154] D. Tang, Z. Teng, G. Canton, T. S. Hatsukami, L. Dong, X. Huang, and C. Yuan, "Local critical stress correlates better than global maximum stress with plaque morphological features linked to atherosclerotic plaque vulnerability: an in vivo multi-patient study," *Biomed Eng Online*, vol. 8, p. 15, Aug. 2009.

[155] J. R. Leach, V. L. Rayz, B. Soares, M. Wintermark, M. R. K. Mofrad, and D. Saloner, "Carotid atheroma rupture observed in vivo and FSI-Predicted stress distribution based on pre-rupture imaging," *Ann Biomed Eng*, vol. 38, pp. 2748–2765, Aug. 2010.

[156] U. Sadat, Z. Teng, V. E. Young, S. R. Walsh, Z. Y. Li, M. J. Graves, K. Varty, and J. H. Gillard, "Association between biomechanical structural stresses of atherosclerotic carotid plaques and

subsequent ischaemic cerebrovascular events–a longitudinal in vivo magnetic resonance imaging-based finite element study," *Eur J Vasc Endovasc Surg*, vol. 40, pp. 485–491, Oct. 2010.

[157] H. Gao, Q. Long, M. Graves, J. H. Gillard, and Z.-Y. Li, "Study of reproducibility of human arterial plaque reconstruction and its effects on stress analysis based on multispectral in vivo magnetic resonance imaging," *J Magn Reson Imaging*, vol. 30, pp. 85–93, July 2009.

[158] F. P. Glor, Q. Long, A. D. Hughes, A. D. Augst, B. Ariff, S. A. M. Thom, P. R. Verdonck, and X. Y. Xu, "Reproducibility study of magnetic resonance image-based computational fluid dynamics prediction of carotid bifurcation flow," *Annals of Biomedical Engineering*, vol. 31, no. 2, pp. 142–151, 2003.

[159] A. J. Bank, A. Versluis, S. M. Dodge, and W. H. Douglas, "Atherosclerotic plaque rupture: a fatigue process?," *Medical hypotheses*, vol. 55, no. 6, pp. 480–484, 2000.

[160] W. E. Stehbens, "The elusive local factor in atherosclerosis," *Medical hypotheses*, vol. 48, no. 6, pp. 503–509, 1997.

[161] L. Zheng, Z. Sun, J. Li, R. Zhang, X. Zhang, S. Liu, J. Li, C. Xu, D. Hu, and Y. Sun, "Pulse pressure and mean arterial pressure in relation to ischemic stroke among patients with uncontrolled hypertension in rural areas of china," *Stroke*, vol. 39, pp. 1932–1937, July 2008.

[162] J. K. Lovett, S. C. Howard, and P. M. Rothwell, "Pulse pressure is independently associated with carotid plaque ulceration," *J. Hypertens.*, vol. 21, pp. 1669–1676, Sept. 2003.

[163] P. Ringleb, J. Allenberg, H. Brückmann, H. Eckstein, G. Fraedrich, M. Hartmann, M. Hennerici, O. Jansen, G. Klein, A. Kunze, *et al.*, "30 day results from the space trial of stent-protected angioplasty versus carotid endarterectomy in symptomatic patients: a randomised non-inferiority trial.," *Lancet*, vol. 368, no. 9543, pp. 1239–1247, 2006.

[164] J. S. Yadav, M. H. Wholey, R. E. Kuntz, P. Fayad, B. T. Katzen, G. J. Mishkel, T. K. Bajwa, P. Whitlow, N. E. Strickman, M. R. Jaff, J. J. Popma, D. B. Snead, D. E. Cutlip, B. G. Firth, and

K. Ouriel, "Protected carotid-artery stenting versus endarterectomy in high-risk patients," *N. Engl. J. Med.*, vol. 351, pp. 1493–1501, Oct. 2004.

[165] M. Cosottini, M. C. Michelassi, W. Bencivelli, G. Lazzarotti, S. Picchietti, G. Orlandi, G. Parenti, and M. Puglioli, "In stent restenosis predictors after carotid artery stenting," *Stroke Res Treat*, vol. 2010, 2010.

[166] M. Bosiers, G. de Donato, K. Deloose, J. Verbist, P. Peeters, F. Castriota, A. Cremonesi, and C. Setacci, "Does free cell area influence the outcome in carotid artery stenting?," *Eur J Vasc Endovasc Surg*, vol. 33, pp. 135–141; discussion 142–143, Feb. 2007.

[167] W. Wu, M. Qi, X.-P. Liu, D.-Z. Yang, and W.-Q. Wang, "Delivery and release of nitinol stent in carotid artery and their interactions: a finite element analysis," *J Biomech*, vol. 40, no. 13, pp. 3034–3040, 2007.

[168] F. Auricchio, M. Conti, M. De Beule, G. De Santis, and B. Verhegghe, "Carotid artery stenting simulation: From patient-specific images to finite element analysis," *Medical engineering & physics*, vol. 33, no. 3, pp. 281–289, 2011.

[169] S. Müller-Hülsbeck, P. J. Schäfer, N. Charalambous, S. R. Schaffner, M. Heller, and T. Jahnke, "Comparison of carotid stents: an in-vitro experiment focusing on stent design," *J. Endovasc. Ther.*, vol. 16, pp. 168–177, Apr. 2009.

[170] M. Conti, D. Van Loo, F. Auricchio, M. De Beule, G. De Santis, B. Verhegghe, S. Pirrelli, and A. Odero, "Impact of carotid stent cell design on vessel scaffolding: a case study comparing experimental investigation and numerical simulations," *J. Endovasc. Ther.*, vol. 18, pp. 397–406, June 2011.

[171] S. Zhao, L. Gu, and S. R. Froemming, "Finite element analysis of the implantation of a self-expanding stent: Impact of lesion calcification," *Journal of Medical Devices*, vol. 6, p. 021001, 2012.

[172] G. De Santis, M. Conti, B. Trachet, T. De Schryver, M. De Beule, J. Degroote, J. Vierendeels, F. Auricchio, P. Segers, P. Verdonck, and B. Verhegghe, "Haemodynamic impact of stent-vessel (mal)apposition following carotid artery stenting: mind the gaps!,"

Computer methods in biomechanics and biomedical engineering, Dec. 2011.

[173] P. Mortier, M. De Beule, P. Segers, P. Verdonck, and B. Verhegghe, "Virtual bench testing of new generation coronary stents," *EuroIntervention*, vol. 7, pp. 369–376, July 2011.

[174] P. Mortier, H. M. v. Beusekom, M. D. Beule, I. Krabbendam-Peters, B. V. D. Smissen, G. D. Santis, J. M. Ligthart, B. Verhegghe, and W. J. v. d. Giessen, "Improved understanding of stent malapposition using virtual bench testing," vol. 6, no. 2, pp. 106–109, 2011.

[175] J. Cebral, R. Löhner, O. Soto, P. Choyke, and P. Yim, "Patient-specific simulation of carotid artery stenting using computational fluid dynamics," in *Medical Image Computing and Computer-Assisted Intervention–MICCAI 2001*, pp. 153–160, Springer, 2001.

[176] M. Conti, M. De Beule, P. Mortier, D. Van Loo, P. Verdonck, F. Vermassen, P. Segers, F. Auricchio, and B. Verhegghe, "Nitinol embolic protection filters: design investigation by finite element analysis," *Journal of materials engineering and performance*, vol. 18, no. 5, pp. 787–792, 2009.

[177] R. T. Lee, H. M. Loree, G. C. Cheng, E. H. Lieberman, N. Jaramillo, and F. J. Schoen, "Computational structural analysis based on intravascular ultrasound imaging before in vitro angioplasty: prediction of plaque fracture locations," *J. Am. Coll. Cardiol.*, vol. 21, pp. 777–782, Mar. 1993.

[178] G. A. Holzapfel, M. Stadler, and T. C. Gasser, "Towards a computational methodology for optimizing angioplasty treatments with stenting," *Mechanics of biological tissue. Springer, Heidelberg*, pp. 207–220, 2005.

[179] P. Mortier, M. De Beule, D. Van Loo, B. Verhegghe, and P. Verdonck, "Finite element analysis of side branch access during bifurcation stenting," *Med Eng Phys*, vol. 31, pp. 434–440, May 2009.

[180] W. Jeong and K. Rhee, "Hemodynamics of cerebral aneurysms: Computational analyses of aneurysm progress and treatment," *Computational and Mathematical Methods in Medicine*, vol. 2012, 2012.

[181] J. R. Cebral, M. A. Castro, S. Appanaboyina, C. M. Putman, D. Millan, and A. F. Frangi, "Efficient pipeline for image-based patient-specific analysis of cerebral aneurysm hemodynamics: technique and sensitivity," *IEEE Trans Med Imaging*, vol. 24, pp. 457–467, Apr. 2005.

[182] S. Takeuchi and T. Karino, "Flow patterns and distributions of fluid velocity and wall shear stress in the human internal carotid and middle cerebral arteries," *World Neurosurg*, vol. 73, pp. 174–185; discussion e27, Mar. 2010.

[183] M. S. Alnæs, J. Isaksen, K.-A. Mardal, B. Romner, M. K. Morgan, and T. Ingebrigtsen, "Computation of hemodynamics in the circle of willis," *Stroke*, vol. 38, pp. 2500–2505, Sept. 2007.

[184] N. Resnick, H. Yahav, A. Shay-Salit, M. Shushy, S. Schubert, L. C. M. Zilberman, and E. Wofovitz, "Fluid shear stress and the vascular endothelium: for better and for worse," *Prog. Biophys. Mol. Biol.*, vol. 81, pp. 177–199, Apr. 2003.

[185] C. M. Schirmer and A. M. Malek, "Wall shear stress gradient analysis within an idealized stenosis using non-newtonian flow," *Neurosurgery*, vol. 61, pp. 853–863; discussion 863–864, Oct. 2007.

[186] H. Meng, Z. Wang, Y. Hoi, L. Gao, E. Metaxa, D. D. Swartz, and J. Kolega, "Complex hemodynamics at the apex of an arterial bifurcation induces vascular remodeling resembling cerebral aneurysm initiation," *Stroke*, vol. 38, pp. 1924–1931, June 2007.

[187] Z. Kulcsár, A. Ugron, M. Marosfoi, Z. Berentei, G. Paál, and I. Szikora, "Hemodynamics of cerebral aneurysm initiation: the role of wall shear stress and spatial wall shear stress gradient," *AJNR Am J Neuroradiol*, vol. 32, pp. 587–594, Mar. 2011.

[188] M. Shojima, M. Oshima, K. Takagi, R. Torii, M. Hayakawa, K. Katada, A. Morita, and T. Kirino, "Magnitude and role of wall shear stress on cerebral aneurysm computational fluid dynamic study of 20 middle cerebral artery aneurysms," *Stroke*, vol. 35, pp. 2500–2505, Nov. 2004.

[189] A. A. Valencia, A. M. Guzmán, E. A. Finol, and C. H. Amon, "Blood flow dynamics in saccular aneurysm models of the basilar artery," *J Biomech Eng*, vol. 128, pp. 516–526, Aug. 2006.

[190] A. Mantha, C. Karmonik, G. Benndorf, C. Strother, and R. Metcalfe, "Hemodynamics in a cerebral artery before and after the formation of an aneurysm," *AJNR Am J Neuroradiol*, vol. 27, pp. 1113–1118, May 2006.

[191] L. Boussel, V. Rayz, C. McCulloch, A. Martin, G. Acevedo-Bolton, M. Lawton, R. Higashida, W. S. Smith, W. L. Young, and D. Saloner, "Aneurysm growth occurs at region of low wall shear stress patient-specific correlation of hemodynamics and growth in a longitudinal study," *Stroke*, vol. 39, pp. 2997–3002, Nov. 2008.

[192] L. D. Jou, D. H. Lee, H. Morsi, and M. E. Mawad, "Wall shear stress on ruptured and unruptured intracranial aneurysms at the internal carotid artery," *American Journal of Neuroradiology*, vol. 29, no. 9, pp. 1761–1767, 2008.

[193] J. Xiang, S. K. Natarajan, M. Tremmel, D. Ma, J. Mocco, L. N. Hopkins, A. H. Siddiqui, E. I. Levy, and H. Meng, "Hemodynamic-morphologic discriminants for intracranial aneurysm rupture," *Stroke*, vol. 42, pp. 144–152, Jan. 2011.

[194] S. Omodaka, S.-I. Sugiyama, T. Inoue, K. Funamoto, M. Fujimura, H. Shimizu, T. Hayase, A. Takahashi, and T. Tominaga, "Local hemodynamics at the rupture point of cerebral aneurysms determined by computational fluid dynamics analysis," *Cerebrovasc. Dis.*, vol. 34, no. 2, pp. 121–129, 2012.

[195] J. R. Cebral, M. A. Castro, J. E. Burgess, R. S. Pergolizzi, M. J. Sheridan, and C. M. Putman, "Characterization of cerebral aneurysms for assessing risk of rupture by using patient-specific computational hemodynamics models," *AJNR Am J Neuroradiol*, vol. 26, pp. 2550–2559, Nov. 2005.

[196] J. R. Cebral, F. Mut, J. Weir, and C. M. Putman, "Association of hemodynamic characteristics and cerebral aneurysm rupture," *AJNR Am J Neuroradiol*, vol. 32, pp. 264–270, Feb. 2011.

[197] H. Takao, Y. Murayama, S. Otsuka, Y. Qian, A. Mohamed, S. Masuda, M. Yamamoto, and T. Abe, "Hemodynamic differences between unruptured and ruptured intracranial aneurysms during observation," *Stroke*, vol. 43, pp. 1436–1439, May 2012.

[198] Y. Hoi, H. Meng, S. H. Woodward, B. R. Bendok, R. A. Hanel, L. R. Guterman, and L. N. Hopkins, "Effects of arterial geometry on aneurysm growth: three-dimensional computational fluid dynamics study," *J. Neurosurg.*, vol. 101, pp. 676–681, Oct. 2004.

[199] G. Lu, L. Huang, X. L. Zhang, S. Z. Wang, Y. Hong, Z. Hu, and D. Y. Geng, "Influence of hemodynamic factors on rupture of intracranial aneurysms: patient-specific 3D mirror aneurysms model computational fluid dynamics simulation," *AJNR Am J Neuroradiol*, vol. 32, pp. 1255–1261, Aug. 2011.

[200] J. G. Isaksen, Y. Bazilevs, T. Kvamsdal, Y. Zhang, J. H. Kaspersen, K. Waterloo, B. Romner, and T. Ingebrigtsen, "Determination of wall tension in cerebral artery aneurysms by numerical simulation," *Stroke*, vol. 39, no. 12, pp. 3172–3178, 2008.

[201] S. Ahmed, I. D. Šutalo, H. Kavnoudias, and A. Madan, "Fluid structure interaction modelling of a patient specific cerebral aneurysm: effect of hypertension and modulus of elasticity," in *16th Australasian Fluid Mechanics Conference, Crown Plaza, Gold Coast Australia*, pp. 2–7, 2007.

[202] R. Torii, M. Oshima, T. Kobayashi, K. Takagi, and T. E. Tezduyar, "Numerical investigation of the effect of hypertensive blood pressure on cerebral aneurysm—Dependence of the effect on the aneurysm shape," *International Journal for Numerical Methods in Fluids*, vol. 54, no. 6-8, p. 995–1009, 2007.

[203] A. Valencia, D. Ledermann, R. Rivera, E. Bravo, and M. Galvez, "Blood flow dynamics and fluid–structure interaction in patient-specific bifurcating cerebral aneurysms," *International Journal for Numerical Methods in Fluids*, vol. 58, no. 10, p. 1081–1100, 2008.

[204] J. R. Cebral, M. A. Castro, R. Löhner, J. E. Burgess, R. Pergolizzi, and C. M. Putman, "Recent developments in patient-specific image-based modeling of hemodynamics," *Mecanica Computacional*, vol. 23, pp. 1471–1482, 2004.

[205] C. Li, S. Wang, J. Chen, H. Yu, Y. Zhang, F. Jiang, S. Mu, H. Li, and X. Yang, "Influence of hemodynamics on recanalization of totally occluded intracranial aneurysms: a patient-specific computational fluid dynamic simulation study," *J. Neurosurg.*, vol. 117, pp. 276–283, Aug. 2012.

[206] C. Groden, J. Laudan, S. Gatchell, and H. Zeumer, "Three-dimensional pulsatile flow simulation before and after endovascular coil embolization of a terminal cerebral aneurysm," *J. Cereb. Blood Flow Metab.*, vol. 21, pp. 1464–1471, Dec. 2001.

[207] H. S. Byun and K. Rhee, "CFD modeling of blood flow following coil embolization of aneurysms," *Medical Engineering & Physics*, vol. 26, pp. 755–761, Nov. 2004.

[208] S. Ahmed, I. D. Šutalo, and H. Kavnoudias, "Hemodynamics and stress distribution in a cerebral aneurysm partially blocked with coils," in *Proceedings of the 5th International Conference on CFD in the Process Industries CSIRO*, pp. 13–15, 2006.

[209] N. M. P. Kakalis, A. P. Mitsos, J. V. Byrne, and Y. Ventikos, "The haemodynamics of endovascular aneurysm treatment: a computational modelling approach for estimating the influence of multiple coil deployment," *IEEE Trans Med Imaging*, vol. 27, pp. 814–824, June 2008.

[210] J. Dequidt, M. Marchal, C. Duriez, E. Kerien, and S. Cotin, "Interactive simulation of embolization coils: modeling and experimental validation," *Med Image Comput Comput Assist Interv*, vol. 11, no. Pt 1, pp. 695–702, 2008.

[211] Y. Wei, S. Cotin, J. Allard, L. Fang, C. Pan, and S. Ma, "Interactive blood-coil simulation in real-time during aneurysm embolization," *Computers & Graphics*, vol. 35, pp. 422–430, Apr. 2011.

[212] J. R. Cebral, F. Mut, M. Raschi, E. Scrivano, R. Ceratto, P. Lylyk, and C. M. Putman, "Aneurysm rupture following treatment with flow-diverting stents: Computational hemodynamics analysis of treatment," *AJNR Am J Neuroradiol*, vol. 32, pp. 27–33, Jan. 2011.

[213] W. Fu, Z. Gu, X. Meng, B. Chu, and A. Qiao, "Numerical simulation of hemodynamics in stented internal carotid aneurysm based on patient-specific model," *J Biomech*, vol. 43, pp. 1337–1342, May 2010.

[214] G. Janiga, C. Rössl, M. Skalej, and D. Thévenin, "Realistic virtual intracranial stenting and computational fluid dynamics for treatment analysis," *J Biomech*, Oct. 2012.

[215] L. Augsburger, P. Reymond, D. A. Rufenacht, and N. Stergiopulos, "Intracranial stents being modeled as a porous medium: flow simulation in stented cerebral aneurysms," *Ann Biomed Eng*, vol. 39, pp. 850–863, Feb. 2011.

[216] I. Larrabide, M. Kim, L. Augsburger, M. C. Villa-Uriol, D. Rüfenacht, and A. F. Frangi, "Fast virtual deployment of self-expandable stents: method and in vitro evaluation for intracranial aneurysmal stenting," *Med Image Anal*, vol. 16, pp. 721–730, Apr. 2012.

[217] S. Appanaboyina, F. Mut, R. Löhner, C. M. Putman, and J. R. Cebral, "Computational fluid dynamics of stented intracranial aneurysms using adaptive embedded unstructured grids," *International journal for numerical methods in fluids*, vol. 57, no. 5, pp. 475–493, 2008.

[218] R. S. Heller and A. M. Malek, "Delivery technique plays an important role in determining vessel wall apposition of the enterprise self-expanding intracranial stent," *J NeuroIntervent Surg*, vol. 3, pp. 340–343, Dec. 2011.

[219] D. A. Siqueira, A. A. Abizaid, J. d. R. Costa, F. Feres, L. A. Mattos, R. Staico, A. A. Abizaid, L. F. Tanajura, A. Chaves, M. Centemero, A. G. M. R. Sousa, and J. E. M. R. Sousa, "Late incomplete apposition after drug-eluting stent implantation: incidence and potential for adverse clinical outcomes," *Eur Heart J*, vol. 28, pp. 1304–1309, June 2007.

[220] Q.-H. Huang, Y.-F. Wu, Y. Xu, B. Hong, L. Zhang, and J.-M. Liu, "Vascular geometry change because of endovascular stent placement for anterior communicating artery aneurysms," *AJNR Am J Neuroradiol*, vol. 32, pp. 1721–1725, Oct. 2011.

[221] A. Bernardini, I. Larrabide, L. Petrini, G. Pennati, E. Flore, M. Kim, and A. F. Frangi, "Deployment of self-expandable stents in aneurysmatic cerebral vessels: comparison of different computational approaches for interventional planning," *Comput Methods Biomech Biomed Engin*, vol. 15, no. 3, pp. 303–311, 2012.

[222] D. Ma, G. F. Dargush, S. K. Natarajan, E. I. Levy, A. H. Siddiqui, and H. Meng, "Computer modeling of deployment and mechanical expansion of neurovascular flow diverter in patient-specific intracranial aneurysms," *Journal of Biomechanics*, vol. 45, pp. 2256–2263, Aug. 2012.

[223] M. H. Babiker, L. F. Gonzalez, J. Ryan, F. Albuquerque, D. Collins, A. Elvikis, and D. H. Frakes, "Influence of stent configuration on cerebral aneurysm fluid dynamics," *J Biomech*, vol. 45, pp. 440–447, Feb. 2012.

[224] N. Famaey, G. Sommer, J. Vander Sloten, and G. A. Holzapfel, "Arterial clamping: finite element simulation and in vivo validation," *J Mech Behav Biomed Mater*, vol. 12, pp. 107–118, Aug. 2012.

[225] D. C. Suh, S.-T. Park, T. S. Oh, S.-O. Park, O. K. Lim, S. Park, C. W. Ryu, D. H. Lee, Y. B. Ko, S.-W. Lee, K. Yoon, and J. S. Kim, "High shear stress at the surface of enhancing plaque in the systolic phase is related to the symptom presentation of severe m1 stenosis," *Korean J Radiol*, vol. 12, no. 4, pp. 515–518, 2011.

[226] D. C. Suh, Y. B. Ko, S.-T. Park, K. Yoon, O. K. Lim, J. S. Oh, Y. G. Jeong, and J. S. Kim, "Computational flow dynamics of the severe m1 stenosis before and after stenting," *Neurointervention*, vol. 6, pp. 13–16, Feb. 2011.

[227] J. Murphy and F. Boyle, "Predicting neointimal hyperplasia in stented arteries using time-dependant computational fluid dynamics: a review," *Comput. Biol. Med.*, vol. 40, pp. 408–418, Apr. 2010.

[228] V. Mitelberg and D. Stoeckel, "Method of manufacturing small profile medical devices," June 27 2007. EP Patent 1,266,637.

[229] S. De Bock, F. Iannaccone, G. De Santis, M. De Beule, D. Van Loo, D. Devos, F. Vermassen, P. Segers, and B. Verhegghe, "Virtual evaluation of stent graft deployment: A validated modeling and simulation study," *Journal of the Mechanical Behavior of Biomedical Materials*, vol. 13, pp. 129–139, 2012.

[230] F. Iannaccone, N. Debusschere, S. De Bock, M. De Beule, D. Van Loo, F. Vermassen, P. Segers, and B. Verhegghe, "The influence of vascular anatomy on carotid artery stenting: A parametric study for damage assessment," *Journal of Biomechanics*, 2014.

[231] S. Chaturvedi, A. Bruno, T. Feasby, R. Holloway, O. Benavente, S. Cohen, R. Cote, D. Hess, J. Saver, J. Spence, *et al.*, "Carotid endarterectomy—an evidence-based review report of the therapeutics and technology assessment subcommittee of the american academy of neurology," *Neurology*, vol. 65, no. 6, pp. 794–801, 2005.

[232] Nallamothu BK, Gurm HS, Ting HH, and et al, "OPerator experience and carotid stenting outcomes in medicare beneficiaries," *JAMA*, vol. 306, pp. 1338–1343, Sept. 2011.

[233] Halm, "The good, the bad, and the about-to-get ugly: National trends in carotid revascularization: comment on "geographic variation in carotid revascularization among medicare beneficiaries, 2003-2006"," *Arch Intern Med*, vol. 170, pp. 1225–1227, July 2010.

[234] D. J. H. McCabe, A. C. Pereira, A. Clifton, J. M. Bland, and M. M. Brown, "Restenosis after carotid angioplasty, stenting, or endarterectomy in the carotid and vertebral artery transluminal angioplasty study (CAVATAS)," *Stroke*, vol. 36, pp. 281–286, Feb. 2005.

[235] L. H. Timmins, M. W. Miller, F. J. Clubb, and J. E. Moore, "Increased artery wall stress post-stenting leads to greater intimal thickening," *Lab Invest*, vol. 91, pp. 955–967, June 2011.

[236] J. C. Ritter and M. R. Tyrrell, "The current management of carotid atherosclerotic disease: who, when and how?," *Interact CardioVasc Thorac Surg*, vol. 16, pp. 339–346, Mar. 2013.

[237] W. E. Hellings, R. G. A. Ackerstaff, G. Pasterkamp, J. De Vries, and F. L. Moll, "The carotid atherosclerotic plaque and microembolisation during carotid stenting," *Journal of cardiovascular surgery*, vol. 47, no. 2, pp. 115–126, 2006.

[238] J. N. E. Redgrave, J. K. Lovett, and P. M. Rothwell, "Histological features of symptomatic carotid plaques in relation to age and smoking: The oxford plaque study," *Stroke*, vol. 41, pp. 2288–2294, Sept. 2010.

[239] G. W. van Lammeren, B. L. Reichmann, F. L. Moll, M. L. Bots, D. P. V. de Kleijn, J.-P. P. M. de Vries, G. Pasterkamp, and G. J. de Borst, "Atherosclerotic plaque vulnerability as an explanation for the increased risk of stroke in elderly undergoing carotid artery stenting," *Stroke*, vol. 42, pp. 2550–2555, July 2011.

[240] N. Uchiyama, K. Misaki, M. Mohri, T. Watanabe, Y. Hirota, M. Nakada, Y. Hayashi, F. Ueda, and J.-i. Hamada, "Association between carotid plaque composition assessed by multidetector computed tomography and cerebral embolism after carotid stenting," *Neuroradiology*, vol. 54, pp. 487–493, July 2011.

[241] I. Pericevic, C. Lally, D. Toner, and D. J. Kelly, "The influence of plaque composition on underlying arterial wall stress during stent expansion: The case for lesion-specific stents," *Medical Engineering & Physics*, vol. 31, pp. 428–433, May 2009.

[242] G. A. Holzapfel, G. Sommer, and P. Regitnig, "Anisotropic mechanical properties of tissue components in human atherosclerotic plaques," *Transactions of the ASME-K-Journal of Biomechanical Engineering*, vol. 126, no. 5, pp. 657–665, 2004.

[243] F. Auricchio, M. Conti, A. Ferrara, S. Morganti, and A. Reali, "Patient-specific finite element analysis of carotid artery stenting: a focus on vessel modeling," *International Journal for Numerical Methods in Biomedical Engineering*, p. n/a–n/a, 2012.

[244] D. Balzani, J. Schröder, and D. Gross, "Simulation of discontinuous damage incorporating residual stresses in circumferentially overstretched atherosclerotic arteries," *Acta Biomaterialia*, vol. 2, pp. 609–618, Nov. 2006.

[245] J. Krejza, M. Arkuszewski, S. E. Kasner, J. Weigele, A. Ustymowicz, R. W. Hurst, B. L. Cucchiara, and S. R. Messe, "Carotid artery diameter in men and women and the relation to body and neck size," *Stroke*, vol. 37, pp. 1103–1105, Apr. 2006.

[246] T. C. Gasser, R. W. Ogden, and G. A. Holzapfel, "Hyperelastic modelling of arterial layers with distributed collagen fibre orientations," *Journal of The Royal Society Interface*, vol. 3, pp. 15–35, Feb. 2006.

[247] G. Sommer and G. A. Holzapfel, "3D constitutive modeling of the biaxial mechanical response of intact and layer-dissected human carotid arteries," *Journal of the Mechanical Behavior of Biomedical Materials*, vol. 5, pp. 116–128, Jan. 2012.

[248] A. N. Annaidh, M. Destrade, M. D. Gilchrist, and J. G. Murphy, "Deficiencies in numerical models of anisotropic nonlinearly elastic materials," *Biomech Model Mechanobiol*, vol. 12, pp. 781–791, Aug. 2013.

[249] G. A. Holzapfel, "Collagen in arterial walls: Biomechanical aspects," in *Collagen* (P. Fratzl, ed.), pp. 285–324, Springer US, Jan. 2008.

[250] S. De Bock, F. Iannaccone, G. De Santis, M. De Beule, P. Mortier, B. Verhegghe, and P. Segers, "Our capricious vessels: The influence of stent design and vessel geometry on the mechanics of intracranial aneurysm stent deployment," *J Biomech*, vol. 45, pp. 1353–1359, May 2012.

[251] P. Gong and A. R. Pelton, "Finite element analysis on nitinol medical applications," in *SMST-2003: proceedings of the International Conference on Shape Memory and Superelastic Technologies, 5 May to 8 May 2003, Asilomar Conference Center, Pacific Grove, California, USA*, p. 443, ASM International, 2004.

[252] F. Auricchio, R. L. Taylor, and J. Lubliner, "Shape-memory alloys: macromodelling and numerical simulations of the superelastic behavior," *Computer methods in applied mechanics and engineering*, vol. 146, no. 3-4, pp. 281–312, 1997.

[253] R. T. Lee, H. M. Loree, G. C. Cheng, E. H. Lieberman, N. Jaramillo, and F. J. Schoen, "Computational structural analysis based on intravascular ultrasound imaging before in vitro angioplasty: Prediction of plaque fracture locations," *Journal of the American College of Cardiology*, vol. 21, pp. 777–782, Mar. 1993.

[254] D. Albrecht, S. Kaspers, R. Füssl, H. W. Höpp, and U. Sechtem, "Coronary plaque morphology affects stent deployment: Assessment by intracoronary ultrasound," *Catheterization and Cardiovascular Diagnosis*, vol. 38, pp. 229–235, July 1996.

[255] G. Finet, N. J. Weissman, G. S. Mintz, L. F. Satler, K. M. Kent, J. R. Laird, G. A. Adelmann, A. E. Ajani, M. T. Castagna, G. Rioufol, and A. D. Pichard, "Mechanism of lumen enlargement with direct stenting versus predilatation stenting: influence of remodelling and plaque characteristics assessed by volumetric intracoronary ultrasound," *Heart*, vol. 89, pp. 84–90, Jan. 2003.

[256] M. Sahara, H. Kirigaya, Y. Oikawa, J. Yajima, K. Nagashima, H. Hara, K. Ogasawara, and T. Aizawa, "Soft plaque detected on intravascular ultrasound is the strongest predictor of in-stent restenosis: an intravascular ultrasound study," *Eur Heart J*, vol. 25, pp. 2026–2033, Nov. 2004.

[257] R. Lee, "Atherosclerotic lesion mechanics versus biology," *Zeitschrift für Kardiologie*, vol. 89, no. 2, pp. S080–S084, 2000.

[258] J. Baptista, V. A. Umans, C. D. Mario, J. Escaned, P. D. Feyter, and P. W. Serruys, "Mechanisms of luminal enlargement and quantification of vessel wall trauma following balloon coronary angioplasty and directional atherectomy a study using intracoronary ultrasound, angioscopy and angiography," *Eur Heart J*, vol. 16, pp. 1603–1612, Nov. 1995.

[259] E. R. Edelman and C. Rogers, "Pathobiologic responses to stenting," *The American Journal of Cardiology*, vol. 81, pp. 4E–6E, Apr. 1998.

[260] C. Rogers and E. R. Edelman, "Endovascular stent design dictates experimental restenosis and thrombosis," *Circulation*, vol. 91, pp. 2995–3001, June 1995.

[261] L. H. Timmins, M. W. Miller, F. J. Clubb, and J. E. Moore, "Increased artery wall stress post-stenting leads to greater intimal thickening," *Laboratory Investigation*, vol. 91, no. 6, pp. 955–967, 2011.

[262] P. Mortier, G. A. Holzapfel, M. De Beule, D. Van Loo, Y. Taeymans, P. Segers, P. Verdonck, and B. Verhegghe, "A novel simulation strategy for stent insertion and deployment in curved coronary bifurcations: comparison of three drug-eluting stents," *Ann Biomed Eng*, vol. 38, pp. 88–99, Jan. 2010.

[263] W. Wu, D. Z. Yang, Y. Y. Huang, M. Qi, and W. Q. Wang, "Topology optimization of a novel stent platform with drug reservoirs," *Medical engineering & physics*, vol. 30, no. 9, pp. 1177–1185, 2008.

[264] J. Hausleiter, A. Kastrati, J. Mehilli, H. Schühlen, J. Pache, F. Dotzer, J. Dirschinger, and A. Schömig, "Predictive factors for early cardiac events and angiographic restenosis after coronary stent placement in small coronary arteries," *Journal of the American College of Cardiology*, vol. 40, pp. 882–889, Sept. 2002.

[265] X. Liu, K. Tsujita, A. Maehara, G. S. Mintz, G. Weisz, G. D. Dangas, A. J. Lansky, E. M. Kreps, L. E. Rabbani, M. Collins, G. W. Stone, J. W. Moses, R. Mehran, and M. B. Leon, "Intravascular ultrasound assessment of the incidence and predictors of edge dissections after drug-eluting stent implantation," *JACC: Cardiovascular Interventions*, vol. 2, pp. 997–1004, Oct. 2009.

[266] C. Simpfendorfer, J. Belardi, G. Bellamy, K. Galan, I. Franco, and J. Hollman, "Frequency, management and follow-up of patients with acute coronary occlusions after percutaneous transluminal coronary angioplasty," *The American Journal of Cardiology*, vol. 59, pp. 267–269, Feb. 1987.

[267] M. Ohyama, K. Mizushige, H. Ohyama, T. Takahashi, N. Hosomi, S.-i. Ichihara, and M. Kohno, "Carotid turbulent flow observed by convergent color doppler flowmetry in silent cerebral infarction," *The International Journal of Cardiovascular Imaging (formerly Cardiac Imaging)*, vol. 18, no. 2, pp. 119–124, 2002.

[268] M. Onizuka, K. Kazekawa, S. Nagata, M. Tsutsumi, H. Aikawa, M. Tomokiyo, M. Iko, T. Kodama, K. Nii, S. Matsubara, and A. Tanaka, "The significance of incomplete stent apposition in patients undergoing stenting of internal carotid artery stenosis," *AJNR Am J Neuroradiol*, vol. 27, pp. 1505–1507, Aug. 2006.

[269] M. I. Papafaklis, C. V. Bourantas, P. E. Theodorakis, C. S. Katsouras, D. I. Fotiadis, and L. K. Michalis, "Relationship of shear stress with in-stent restenosis: Bare metal stenting and the effect of brachytherapy," *International Journal of Cardiology*, vol. 134, pp. 25–32, May 2009.

[270] D. Massop, R. Dave, C. Metzger, W. Bachinsky, M. Solis, R. Shah, G. Schultz, T. Schreiber, M. Ashchi, and R. Hibbard, "Stenting and angioplasty with protection in patients at high-risk for endarterectomy: Sapphire worldwide registry first 2,001 patients," *Catheterization and Cardiovascular Interventions*, vol. 73, no. 2, pp. 129–136, 2009.

[271] C. J. White, "Carotid artery stent placement," *J Am Coll Cardiol Intv*, vol. 3, pp. 467–474, May 2010.

[272] A. Cremonesi, C. Setacci, R. Manetti, G. de Donato, F. Setacci, G. Balestra, I. Borghesi, P. Bianchi, and F. Castriota, "Carotid angioplasty and stenting: lesion related treatment strategies," *EuroIntervention*, vol. 1, pp. 289–295, Nov. 2005.

[273] W. A. Gray, K. A. Rosenfield, M. R. Jaff, S. Chaturvedi, L. Peng, and P. Verta, "Influence of site and operator characteristics on carotid artery stent OutcomesAnalysis of the CAPTURE 2 (carotid ACCULINK/ACCUNET post approval trial to uncover rare events) clinical study," *JACC: Cardiovascular Interventions*, vol. 4, no. 2, pp. 235–246, 2011.

[274] G. Maleux and A. Nevelsteen, "Carotid artery stenting: which stent for which lesion?," *Acta chirurgica Belgica*, no. 6, pp. 430–434, 2002.

[275] S. Müller-Hülsbeck, H. Preuss, and H. Elhöft, "CAS: which stent for which lesion," *Journal of cardiovascular surgery*, vol. 50, no. 6, pp. 767–772, 2009.

[276] M. Bosiers, K. Deloose, J. Verbist, and P. Peeters, "Carotid artery stenting: which stent for which lesion?," *Vascular*, vol. 13, no. 4, pp. 205–210, 2005.

[277] G. M. Siewiorek, E. A. Finol, and M. H. Wholey, "Clinical significance and technical assessment of stent cell geometry in carotid artery stenting," *Journal of Endovascular Therapy*, vol. 16, pp. 178–188, Apr. 2009.

[278] Y. Ozaki, M. Okumura, T. F. Ismail, H. Naruse, K. Hattori, S. Kan, M. Ishikawa, T. Kawai, Y. Takagi, J. Ishii, F. Prati, and P. W. Serruys, "The fate of incomplete stent apposition with drug-eluting stents: an optical coherence tomography-based natural history study," *European Heart Journal*, Apr. 2010.

[279] G. de Donato, F. Setacci, P. Sirignano, G. Galzerano, A. Cappelli, and C. Setacci, "Optical coherence tomography after carotid stenting: Rate of stent malapposition, plaque prolapse and fibrous cap rupture according to stent design," *European Journal of Vascular and Endovascular Surgery*, vol. 45, pp. 579–587, June 2013.

[280] O. Jansen, J. Fiehler, M. Hartmann, and H. Brückmann, "Protection or nonprotection in carotid stent angioplasty the influence of interventional techniques on outcome data from the SPACE trial," *Stroke*, vol. 40, pp. 841–846, Mar. 2009.

[281] M. Schillinger, M. Gschwendtner, B. Reimers, J. Trenkler, L. Stockx, J. Mair, S. Macdonald, F. Karnel, K. Huber, and E. Minar, "Does carotid stent cell design matter?," *Stroke*, vol. 39, pp. 905–909, Mar. 2008.

[282] R. O. Tadros, C. T. Spyris, A. G. Vouyouka, C. Chung, P. Krishnan, M. W. Arnold, M. L. Marin, and P. L. Faries, "Comparing the embolic potential of open and closed cell stents during carotid angioplasty and stenting," *Journal of vascular surgery*, vol. 56, no. 1, pp. 89–95, 2012.

[283] K. Y. Park, D. I. Kim, B. M. Kim, H. S. Nam, Y. D. Kim, J. H. Heo, and D. J. Kim, "Incidence of embolism associated with carotid artery stenting: open-cell versus closed-cell stents: Clinical article," *Journal of Neurosurgery*, pp. 1–6, June 2013.

[284] J. P. Hart, P. Peeters, J. Verbist, K. Deloose, and M. Bosiers, "Do device characteristics impact outcome in carotid artery stenting?," *Journal of vascular surgery*, vol. 44, no. 4, pp. 725–730, 2006.

[285] J. de Vries, "Comments regarding 'Comparison of stent free cell area and cerebral lesions after unprotected carotid artery stent placement'," *European Journal of Vascular and Endovascular Surgery*, vol. 43, no. 1, p. 15, 2012.

[286] J. Jim, B. G. Rubin, G. S. Landis, C. T. Kenwood, F. S. Siami, and G. A. Sicard, "Society for vascular surgery vascular registry evaluation of stent cell design on carotid artery stenting outcomes," *Journal of Vascular Surgery*, vol. 54, pp. 71–79, July 2011.

[287] I. Q. Grunwald, W. Reith, K. Karp, P. Papanagiotou, H. Sievert, S. Walter, A. L. Kühn, K. Fassbender, and C. Krick, "Comparison of stent free cell area and cerebral lesions after unprotected carotid artery stent placement," *European Journal of Vascular and Endovascular Surgery*, vol. 43, no. 1, pp. 10–14, 2012.

[288] A. Cremonesi, C. Setacci, F. Castriota, and M. Valgimigli, "Carotid stent cell design: Lack of benefit or lack of evidence?," *Stroke*, vol. 39, pp. e130–e130, Aug. 2008.

[289] C. Setacci, G. De Donato, and M. Bosiers, "Two different studies on carotid stent cell design importance, or are we just saying the same thing?," *Stroke*, vol. 39, pp. e129–e129, Aug. 2008.

[290] R. O. Tadros, R. K. Malik, A. G. Vouyouka, S. H. Ellozy, M. L. Marin, and P. L. Faries, "A systematic review of carotid stent design and selection: strategies to optimize procedural outcomes," 2013.

[291] N. M. Grosland, K. H. Shivanna, V. A. Magnotta, N. A. Kallemeyn, N. A. DeVries, S. C. Tadepalli, and C. Lisle, "IA-FEMesh: an open-source, interactive, multiblock approach to anatomic finite element model development," *Computer Methods and Programs in Biomedicine*, vol. 94, pp. 96–107, Apr. 2009.

[292] F. Castriota, A. Liso, G. Biamino, and A. Cremonesi, "Technical evolution of carotid stents," 2008.

[293] S. Morlacchi, S. G. Colleoni, R. Cárdenes, C. Chiastra, J. L. Diez, I. Larrabide, and F. Migliavacca, "Patient-specific simulations of stenting procedures in coronary bifurcations: Two clinical cases," *Medical Engineering & Physics*, vol. 35, pp. 1272–1281, Sept. 2013.

[294] C. Riedel, S. Müller-Hülsbeck, and M. Heller, "Quantitative analyse physiologischer deformationen der karotiden auf der basis von 3D-TOF-MRA -daten," *RöFo - Fortschritte auf dem Gebiet der Röntgenstrahlen und der bildgebenden Verfahren*, vol. 178, May 2006.

[295] D. Vukadinovic, T. van Walsum, R. Manniesing, S. Rozie, R. Hameeteman, T. T. de Weert, A. van der Lugt, and W. J. Niessen, "Segmentation of the outer vessel wall of the common carotid artery in CTA," *Medical Imaging, IEEE Transactions on*, vol. 29, no. 1, pp. 65–76, 2010.

[296] E. S. Connolly and R. A. Solomon, "Management of unruptured aneurysms," *Management of cerebral aneurysms. Philadelphia: Saunders*, pp. 271–85, 2004.

[297] J. Raymond, D. Roy, A. Weill, F. Guilbert, T. Nguyen, A. J. Molyneux, A. J. Fox, and S. C. Johnston, "Unruptured intracranial aneurysms and the trial on endovascular aneurysm management (TEAM): the principles behind the protocol.," *Journal of Vascular and Interventional Neurology*, vol. 1, p. 1, 2008.

[298] Y. Shobayashi, T. Tanoue, S. Tateshima, and K. Tanishita, "Mechanical design of an intracranial stent for treating cerebral aneurysms," *Medical Engineering & Physics*, vol. 32, pp. 1015–1024, Nov. 2010.

[299] Ö. Krischek, E. Miloslavski, S. Fischer, S. Shrivastava, and H. Henkes, "A comparison of functional and physical properties of self-expanding intracranial stents [neuroform3, wingspan, solitaire, leo (+), enterprise]," *min-Minimally Invasive Neurosurgery*, vol. 54, no. 01, pp. 21–28, 2011.

[300] A. Bernardini, I. Larrabide, L. Petrini, G. Pennati, E. Flore, M. Kim, and A. F. Frangi, "Deployment of self-expandable stents in aneurysmatic cerebral vessels: comparison of different computational approaches for interventional planning.," *Computer methods in biomechanics and biomedical engineering*, p. 1, 2011.

[301] F. J. Gijsen, F. Migliavacca, S. Schievano, L. Socci, L. Petrini, A. Thury, J. J. Wentzel, A. F. van der Steen, P. W. Serruys, and G. Dubini, "Simulation of stent deployment in a realistic human coronary artery," *Biomedical engineering online*, vol. 7, no. 1, p. 23, 2008.

[302] S. Appanaboyina, F. Mut, R. Löhner, C. Putman, and J. Cebral, "Simulation of intracranial aneurysm stenting: techniques and challenges," *Computer Methods in Applied Mechanics and Engineering*, vol. 198, no. 45-46, pp. 3567–3582, 2009.

[303] N. P. Brooks, A. S. Turk, D. B. Niemann, B. Aagaard-Kienitz, K. Pulfer, and T. Cook, "Frequency of thromboembolic events associated with endovascular aneurysm treatment: retrospective case series," 2008.

[304] T. Ishibashi, Y. Murayama, T. Saguchi, M. Ebara, K. Irie, H. Takao, and T. Abe, "Thromboembolic events during endovascular coil embolization of cerebral aneurysms," *Interventional Neuroradiology*, vol. 12, no. Suppl 1, p. 112, 2006.

[305] B. B. Lieber, V. Livescu, L. Hopkins, and A. K. Wakhloo, "Particle image velocimetry assessment of stent design influence on intraaneurysmal flow," *Annals of biomedical engineering*, vol. 30, no. 6, pp. 768–777, 2002.

[306] K. Baráth, F. Cassot, D. A. Rüfenacht, and J. H. Fasel, "Anatomically shaped internal carotid artery aneurysm in vitro model for flow analysis to evaluate stent effect," *American journal of neuroradiology*, vol. 25, no. 10, pp. 1750–1759, 2004.

[307] A. Bernardini, I. Larrabide, L. Petrini, G. Pennati, E. Flore, M. Kim, and A. Frangi, "Deployment of self-expandable stents in aneurysmatic cerebral vessels: comparison of different computational approaches for interventional planning," *Computer methods in biomechanics and biomedical engineering*, vol. 15, no. 3, pp. 303–311, 2012.

[308] A. Fernandez Zubillaga, G. Guglielmi, F. Vinuela, and G. R. Duckwiler, "Endovascular occlusion of intracranial aneurysms with electrically detachable coils: correlation of aneurysm neck size and treatment results," *American journal of neuroradiology*, vol. 15, no. 5, p. 815, 1994.

[309] L. Goubergrits, J. Pöthke, C. Petz, H. C. Hege, A. Spuler, and U. Kertzscher, "3D bildgebung von zerebralen aneurysmen," *Bildverarbeitung Für Die Medizin 2008: Algorithmen-Systeme-Anwendungen*, p. 153, 2008.

[310] L. Prandtl, H. Oertel, M. Böhle, D. Etling, U. Müller, K. R. Sreenivasan, U. Riedel, and J. Warnatz, *Prandtl's Essentials of Fluid Mechanics*. Springer, 2004.

[311] A. Creane, E. Maher, S. Sultan, N. Hynes, D. J. Kelly, and C. Lally, "Finite element modelling of diseased carotid bifurcations generated from in vivo computerised tomographic angiography," *Computers in Biology and Medicine*, vol. 40, no. 4, pp. 419–429, 2010.

[312] A. O. Cifuentes and A. Kalbag, "A performance study of tetrahedral and hexahedral elements in 3-d finite element structural analysis," *Finite Elements in Analysis and Design*, vol. 12, no. 3-4, pp. 313–318, 1992.

[313] S. E. Benzley, E. Perry, K. Merkley, B. Clark, and G. Sjaardama, "A comparison of all hexagonal and all tetrahedral finite element meshes for elastic and elasto-plastic analysis," in *Proceedings, 4th International Meshing Roundtable*, p. 179–191, Citeseer, 1995.

[314] J. B. Thomas, L. Antiga, S. L. Che, J. S. Milner, D. A. Hangan Steinman, J. D. Spence, B. K. Rutt, and D. A. Steinman, "Variation in the carotid bifurcation geometry of young versus older adults: implications for geometric risk of atherosclerosis," *Stroke*, vol. 36, no. 11, p. 2450, 2005.

[315] S. W. Hsu, J. C. Chaloupka, J. A. Feekes, M. D. Cassell, and Y. F. Cheng, "In vitro studies of the neuroform microstent using transparent human intracranial arteries," *American journal of neuroradiology*, vol. 27, no. 5, p. 1135, 2006.

[316] R. P. Benitez, M. T. Silva, J. Klem, E. Veznedaroglu, and R. H. Rosenwasser, "Endovascular occlusion of wide-necked aneurysms with a new intracranial microstent (neuroform) and detachable coils," *Neurosurgery*, vol. 54, no. 6, p. 1359, 2004.

[317] S. Akpek, A. Arat, H. Morsi, R. P. Klucznick, C. M. Strother, and M. E. Mawad, "Self-expandable stent-assisted coiling of wide-necked intracranial aneurysms: a single-center experience," *American journal of neuroradiology*, vol. 26, no. 5, p. 1223, 2005.

[318] N. Ebrahimi, B. Claus, C. Y. Lee, A. Biondi, and G. Benndorf, "Stent conformity in curved vascular models with simulated aneurysm necks using flat-panel CT: an in vitro study," *American journal of neuroradiology*, vol. 28, no. 5, p. 823, 2007.

[319] J. Tanigawa, P. Barlis, K. Dimopoulos, M. Dalby, P. Moore, and C. Di Mario, "The influence of strut thickness and cell design on immediate apposition of drug-eluting stents assessed by optical coherence tomography," *International Journal of Cardiology*, vol. 134, pp. 180–188, May 2009.

[320] R. S. Heller and A. M. Malek, "Parent vessel size and curvature strongly influence risk of incomplete stent apposition in enterprise intracranial aneurysm stent coiling," *AJNR Am J Neuroradiol*, Aug. 2011.

[321] R. S. Heller, W. R. Miele, D. D. Do-Dai, and A. M. Malek, "Crescent sign on magnetic resonance angiography revealing incomplete stent apposition: correlation with diffusion-weighted changes in stent-mediated coil embolization of aneurysms," *Journal of Neurosurgery*, vol. 115, pp. 624–632, Sept. 2011.

[322] G. Sommer, P. Regitnig, L. Költringer, and G. A. Holzapfel, "Biaxial mechanical properties of intact and layer-dissected human carotid arteries at physiological and supraphysiological loadings," *American Journal of Physiology-Heart and Circulatory Physiology*, vol. 298, no. 3, p. H898, 2010.

[323] K. Monson, N. Barbaro, and G. Manley, "Multiaxial response of human cerebral arteries," in *Annual Meeting of the American Society of Biomechanics. Blacksburg, VA: Virginia Polytechnic Institute and State University*, 2006.

[324] D. O. Wiebers, "Unruptured intracranial aneurysms: natural history, clinical outcome, and risks of surgical and endovascular treatment," *The Lancet*, vol. 362, no. 9378, pp. 103–110, 2003.

[325] L. Pierot, L. Spelle, F. Vitry, *et al.*, "Immediate clinical outcome of patients harboring unruptured intracranial aneurysms treated by endovascular approach results of the atena study," *Stroke*, vol. 39, no. 9, pp. 2497–2504, 2008.

[326] M. Piotin, R. Blanc, L. Spelle, C. Mounayer, R. Piantino, P. J. Schmidt, and J. Moret, "Stent-assisted coiling of intracranial aneurysms clinical and angiographic results in 216 consecutive aneurysms," *Stroke*, vol. 41, no. 1, pp. 110–115, 2010.

[327] K. M. Fargen, B. L. Hoh, B. G. Welch, G. L. Pride, G. Lanzino, A. S. Boulos, J. S. Carpenter, A. Rai, E. Veznedaroglu, A. Ringer, *et al.*, "Long-term results of enterprise stent-assisted coiling of cerebral aneurysms," *Neurosurgery*, vol. 71, no. 2, pp. 239–244, 2012.

[328] I. Wanke and M. Forsting, "Stents for intracranial wide-necked aneurysms: more than mechanical protection," *Neuroradiology*, vol. 50, no. 12, pp. 991–998, 2008.

[329] M. Kim, E. I. Levy, H. Meng, and L. N. Hopkins, "Quantification of hemodynamic changes induced by virtual placement of multiple stents across a wide-necked basilar trunk aneurysm," *Neurosurgery*, vol. 61, no. 6, p. 1305, 2007.

[330] D. Lopes and S. Sani, "Histological postmortem study of an internal carotid artery aneurysm treated with the neuroform stent," *Neurosurgery*, vol. 56, no. 2, p. E416, 2005.

[331] A. Biondi, V. Janardhan, J. M. Katz, K. Salvaggio, H. A. Riina, and Y. P. Gobin, "Neuroform stent-assisted coil embolization of wide-neck intracranial aneurysms: Strategies in stent deployment and midterm follow-up," *Neurosurgery*, vol. 61, no. 3, pp. 460–469, 2007.

[332] D. Fiorella, F. C. Albuquerque, V. R. Deshmukh, and C. G. McDougall, "Usefulness of the neuroform stent for the treatment of cerebral aneurysms: results at initial (3–6-mo) follow-up," *Neurosurgery*, vol. 56, no. 6, pp. 1191–1202, 2005.

[333] N. Patel, M. J. Gounis, A. Wakhloo, N. Noordhoek, J. Blijd, D. Babic, D. Takhtani, S.-K. Lee, and A. Norbash, "Contrast-enhanced angiographic cone-beam ct of cerebrovascular stents: experimental optimization and clinical application," *American Journal of Neuroradiology*, vol. 32, no. 1, pp. 137–144, 2011.

[334] G. Benndorf, B. Claus, C. M. Strother, L. Chang, and R. P. Klucznik, "Increased cell opening and prolapse of struts of a neuroform stent in curved vasculature: value of angiographic computed tomography: technical case report," *Neurosurgery*, vol. 58, no. 4, pp. ONS–E380, 2006.

[335] T. F. Flood, I. M. van der Bom, L. Strittmatter, A. S. Puri, G. M. Hendricks, A. K. Wakhloo, and M. J. Gounis, "Quantitative analysis of high-resolution, contrast-enhanced, cone-beam ct for the detection of intracranial in-stent hyperplasia," *Journal of NeuroInterventional Surgery*, pp. neurintsurg–2013, 2014.

[336] G. J. Hall and E. P. Kasper, "Comparison of element technologies for modeling stent expansion," *Journal of biomechanical engineering*, vol. 128, pp. 751–6, Oct. 2006.

[337] J. D. Chalupnik, C. Daly, and H. C. Merchant, *Material properties of cerebral blood vessels.* Department of Mechanical Engineering, University of Washington, 1971.

[338] K. L. Monson, N. M. Barbaro, and G. T. Manley, "Biaxial response of passive human cerebral arteries," *Annals of biomedical engineering*, vol. 36, no. 12, pp. 2028–2041, 2008.

[339] M. Kojima, K. Irie, T. Fukuda, F. Arai, Y. Hirose, and M. Negoro, "The study of flow diversion effects on aneurysm using multiple enterprise stents and two flow diverters," *Asian journal of neurosurgery*, vol. 7, no. 4, p. 159, 2012.

[340] J. Sedat, Y. Chau, L. Mondot, J. Vargas, J. Szapiro, and M. Lonjon, "Endovascular occlusion of intracranial wide-necked aneurysms with stenting (neuroform) and coiling: mid-term and long-term results," *Neuroradiology*, vol. 51, no. 6, pp. 401–409, 2009.

[341] A. Farb, A. P. Burke, F. D. Kolodgie, and R. Virmani, "Pathological mechanisms of fatal late coronary stent thrombosis in humans," *Circulation*, vol. 108, no. 14, pp. 1701–1706, 2003.

[342] P. H. Grewe, T. Deneke, A. Machraoui, J. Barmeyer, and K.-M. Müller, "Acute and chronic tissue response to coronary stent implantation: pathologic findings in human specimen," *Journal of the American College of Cardiology*, vol. 35, no. 1, pp. 157–163, 2000.

[343] B. M. Kim, D. J. Kim, and D. I. Kim, "Stent application for the treatment of cerebral aneurysms," *Neurointervention*, vol. 6, no. 2, pp. 53–70, 2011.

[344] A. M. Spiotta, A. M. Wheeler, S. Smithason, F. Hui, and S. Moskowitz, "Comparison of techniques for stent assisted coil embolization of aneurysms," *Journal of neurointerventional surgery*, vol. 4, no. 5, pp. 339–344, 2012.

[345] M. Kelly, R. Turner, S. Moskowitz, V. Gonugunta, M. Hussain, and D. Fiorella, "Delayed migration of a self-expanding intracranial microstent," *American Journal of Neuroradiology*, vol. 29, no. 10, pp. 1959–1960, 2008.

[346] M. De Beule, *Finite element stent design.* PhD thesis, Ghent University, 2008.

[347] P. Mortier, *Computer modelling of coronary bifurcation stenting.* PhD thesis, Ghent University, 2010.

[348] M. Conti, *Finite Element Analysis of Carotid Artery Stenting.* PhD thesis, Ghent University, Università degli Studi di Pavia, 2010.